Master's thesis

NTNU
Norwegian University of Science and Technology
Faculty of Natural Sciences
Department of Physics

Jørgen Sørhaug

TEM characterization of tungsten-implanted silicon

A study of a potential intermediate band solar cell material

Master's thesis in Natural Science with Teacher Education
Supervisor: Randi Holmestad

June 2019

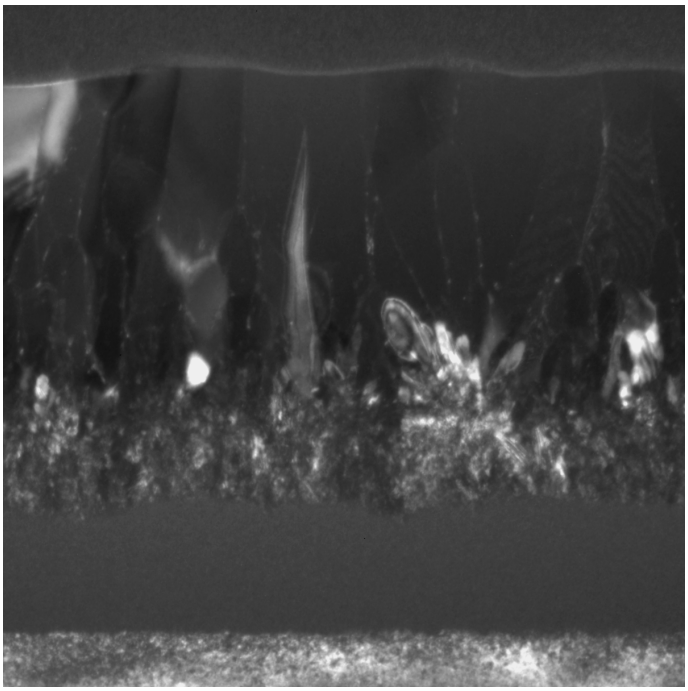

NTNU
Norwegian University of
Science and Technology

Jørgen Sørhaug

TEM characterization of tungsten-implanted silicon

A study of a potential intermediate band solar cell material

Master's thesis in Natural Science with Teacher Education
Supervisor: Randi Holmestad
June 2019

Norwegian University of Science and Technology
Faculty of Natural Sciences
Department of Physics

NTNU
Norwegian University of
Science and Technology

"[...] Energy quanta penetrate into the surface layer of the body, and their energy is transformed, at least in part, into kinetic energy of electrons. The simplest way to image this is that a light quantum delivers its entire energy to a single electron; we shall assume that this is what happens. The possibility should not be excluded, however, that electrons might receive their energy only in part from the light quantum." [1]

Abstract

Global environment, is a growing topic of concern. However, different actions are set, and about to be set, to comply with environmental issues of today and tomorrow. Amongst the attempts to e.g. reduce the use of fossil fuels to generate electricity, is the development and improving of photovoltaic cells to generate environmental friendly power more efficiently. A suggested method for increasing solar cell efficiency, is to use a material with an intermediate energy band. The energy band is positioned between the valence, and the conduction band of a semiconductor. The Shockley-Queisser limit can then perhaps be avoided, and low energetic photons may contribute to electrical power generation.

An intermediate band material must be manufactured, and a possible method is to implant a transition metal such as tungsten (W), into a silicon (Si) matrix. W has however, been reported to induce carrier trap centers in silicon band gap. Nevertheless, if W is introduced in concentrations beyond the equilibrium solubility limit, single partially filled near mid-gap band may be formed. If this is accomplished, the material can be utilized for solar cell application(s).

In this work, tungsten is ion implanted in float-zone silicon wafers, to obtain W peak concentrations of 0.01, 0.1, 0.2, 1 and 2 at.% (referred to as dosages). Areas on the wafers have subsequently been recrystallized, using pulsed laser melting with an energy density of $0.9\,\mathrm{J\,cm^{-2}}$ and $1.8\,\mathrm{J\,cm^{-2}}$. Electron transparent as-implanted and recrystallized samples from the 0.1, 1 and 2 dosage bulk samples - prepared using focused ion beam, have been characterized using transmission electron microscopy techniques, and energy-disper- sive X-ray spectroscopy. Analysis reveal that ion implantation amorphizes the semiconducting host material.

Recrystallized samples using a laser pulse of $0.9\,\mathrm{J\,cm^{-2}}$, does not recrystallize the entire amorphized volume. The melted undercooled silicon, recrystallizes into a layer of large polycrystals of size $0.1 - 1$ µm, whilst heat

dissipation and energy from the solidification is hypothesized to induce explosive crystallization. The result is a large polycrystalline layer, growing from the amorphous/liquid interface towards the sample surface. A fine polycrystalline region is also growing, but disorderly in the opposite direction. The fine polycrystals are of size < 0.1 µm.

The implanted transition metal in the polycrystalline samples, is observed segregated into W_xSi_y precipitates. The precipitates form complex thread-like/filamentary structures, and discontinuous filaments in all the polycrystalline samples. These morphologies, are only observed in the large polycrystalline regions. The W-rich filaments, are more prominent with increasing dopant concentration.

Recrystallized samples using a laser fluence of $1.8\,\mathrm{J\,cm^{-2}}$, recrystallizes the entire amorphized volume. The crystal orientation is observed to be determined by the underlying crystalline silicon, indicating that the undercooled melt regrows epitaxially. Tungsten segregation is also observed in all the completely recrystallized samples, but mainly shaped as discontinuous filaments.

Energy dispersive spectroscopy detects a W peak concentration for the as-implanted samples of 1 at.% and 2 at.%. 0.1 at.% is perhaps too low for the EDS system to detect accurately. The peaks are located approximately 0.6 µm underneath the sample surface, which are 0.1 µm deeper than TRIM simulations. The distribution profiles of the recrystallized samples of dosage 1 and 2, show a small overall movement towards the sample surface. This indicate that W has a slow diffusion in silicon, as expected.

Sammendrag

Det globale miljøet, er et voksende tema av bekymring. Men ulike handlinger er satt i verks, og skal igangsettes for å imøtekomme dagens og morgendagens miljøproblemer. Utviklingen og forbedringer av solceller for å generere miljøvennlig energi mer effektivt, er blant de tiltak som gjøres for å redusere bruk av fossilt brensel til å generere strøm. I den forbindelse, er en foreslått måte å øke solcelle-effektiviteten på, å bruke et materiale med et mellomliggende energibånd mellom en halvleders valens og ledningsbånd. Da kan Shockley-Queisser-grensen kanskje unngås, og lav-energiske fotoner kan da bidra til en effektivisert strømproduksjon.

For å kunne bruke et mellomliggende energibånd-materiale, så må det først lages. En mulig måte å gjøre det på, er å implantere et innskuddsmetall som f.eks. wolfram (W), i en silisium- (Si) matrise. Det har riktignok blitt rapportert at W innfører ladnings-fellesentre i Si-båndgapet. Men dersom W blir introdusert i konsentrasjoner over løselighetsgrensen, kan enkelte, delvis fylte og nært mellomliggende bånd bli dannet. Materialet kan da kanskje bli brukt i forbindelse med solceller.

I dette prosjektet har wolfram blitt ione-implantert i float-zone silisiumswafere, med makskonsentrasjoner på 0.01, 0.1, 0.2, 1 og 2 at.% (referert til som doser). Områder på waferne har deretter blitt rekrystalliser, med bruk av pulsert lasersmelting med en energitetthet på $0.9\,\mathrm{J\,cm^{-2}}$ og $1.8\,\mathrm{J\,cm^{-2}}$. Elektrontransparente as-implanted og rekrystalliserte prøver fra 0.1-, 1- og 2-dose-bulkprøvene - klargjort med fokusert ionestråle, har blitt karakterisert med transmisjon elektronmikroskopi-teknikker, og energi-dispersiv røntgenspektroskopi. Analyser viser at ioneimplantering gjør halvledermaterialet amorft.

Rekrystalliserte prøver ved bruk av en laserpuls på $0.9\,\mathrm{J\,cm^{-2}}$, rekrystalliserer ikke hele det amorfe området. Det smeltede underkjølte silisiumet, rekrystalliseres til et lag med store polykrystaller av størrelsesorden $0.1 - 1$

µm, mens varmeoverføring og energi fra størkningen antas å utløse eksplosiv krystallisering. Resultatet er et polykrystallinsk lag med store krystaller som gror fra det amorfe/flytende grensesjiktet mot prøveoverflaten, og et polykrystallinsk lag med fine korn som gror uordnet i motsatt retning. De fine kornene er av størrelsesorden < 0.1 µm.

Det implanterte innskuddsmetallet i de rekrystalliserte polykrystallinske prøvene, har segregert til W_xSi_y-presipitater. Morfologien til disse presipitatene, er tråd-lignende/filamentlignende strukturer, samt diskontinuerlige filamenter. Strukturene er observert i alle de polykrystallinske prøvene, men kun i laget med store polykrystaller. De W-rike filamentene, er mer fremtredende med økende W-konsentrasjoner.

Rekrystalliserte prøver ved bruk av en laserpuls på $1.8\,\mathrm{J\,cm^{-2}}$, rekrystalliserer hele det amorfe området. Krystallorienteringen er observert å være bestemt av det underliggende krystallinske silisiumet. Dette indikerer at den underkjølte smelta, gror epitaksielt. W er også observert segregert til WSi-presipitater i disse prøvene, men hovedsakelig i diskokntinuerlige filamenter.

Energi-dispersiv røntgen-spektroskopi detekterer en maksimum W-konsentrasjon for as-implanted-prøvene med 1 og 2 at.%. 0.1 at.% er kanskje for lavt for EDS-systemet å detektere, med god sikkerhet. Toppene er posisjonert omtrent 0.6 µm under prøveoverflaten, noe som er 0.1 µm dypere enn TRIM-beregningene. Fordelingsprofilene til de rekrystalliserte prøvene av dose 1 og 2, viser en liten samplet bevegelse mot prøveoverflaten. Dette indikerer at W har en lav diffusjon i silisium, som forventet.

Preface

The work presented in this master thesis, was carried out as a part of my five year M.Sc. degree in physics (through the teacher education program), at the Norwegian University of Science and Technology. The work has been conducted at the department of physics - division of Condensed Matter Physics, at the TEM Gemini centre at NTNU/ SINTEF, and NTNU NanoLab. The presented work is based on H. Lysne's Ph.d. project, about advanced material characterization of materials for use in intermediate band solar cells.

Trondheim, Norway
June 2019

Jørgen A. SØRHAUG

Acknowledgements

To begin with, I will first and foremost express my great gratitude to my supervisor Randi Holmestad, without whom I'd probably never get experience with transmission electron microscopy - the one thing I made as my object to become a high school teacher. I would also like to express my gratitude to Hogne Lysne for supporting me throughout my thesis, and for helping me understand material physics to a greater extent. I would like to thank Turid Dory Reenaas and Marisa Di Sabatino Lundberg for your expertise and good eye to spot features and characteristics in my micrographs, and thorough feedback on my work. You have all been a great group to work with!

I would like to thank Ragnhild Sæterli and Bjørn Gunnar Soleim, for being patient with my training on the immense instrument Jem Jeol 2100F. I am a slow learner, but this has not seemed to be an issue for you. I would also like express some extra gratitude to Bjørn for taking my call whenever I've had issues with 2100F - even in the weekends, guiding me through the problem(s). The both of you have really inspired me to become fond of experimental work, and I really do enjoy doing TEM. Last but one, I would like to thank Paul Monceyron Røren for helping me with some french translation, and lastly the great people whom I live with and see everyday. Only your great support and caring whenever I've had rough days, can make a dark and cloudy day feel like summer.

Contents

List of Abbreviations

AFM	**A**tomic **F**orce **M**icroscope/**M**icroscopy
a/c	**a**morphous/**c**rystalline
a-Si	**a**morphous **Si**licon
BF	**B**right **F**ield
BF-TEM	**B**right **F**ield **T**ransmission **E**lectron **M**icroscopy
BF-STEM	**B**right **F**ield **S**canning **T**ransmission **E**lectron **M**icroscopy
CB	**C**onduction **B**and
DF-TEM	**D**ark **F**ield **T**ransmission **E**lectron **M**icroscopy
DP	**D**iffraction **P**attern
ED	**E**lectron **D**iffraction
EDS/-X	**E**nergy **D**ispersive (**X**-ray) **S**pectroscopy
EOR	**E**nd-**O**f-**R**ange
FIB	**F**ocused **I**on **B**eam
F-poly	**F**ine **poly**crystals
Fz-Si	**F**loat-**z**one **Si**licon
HAADF-STEM	**H**igh **A**ngle **A**nnular **D**ark **F**ield **S**canning **T**ransmission **E**lectron **M**icroscopy
HR	**H**igh **R**esolution
IB	**I**ntermediate **B**and
IBSC	**I**ntermediate **B**and **S**olar **C**ell
L-poly	**L**arge **poly**crystals
MSE	**M**ean **S**quared **E**rror
p.d.f.	**P**earson **D**istribution **P**rofile
p-Si	**p**olycrystalline **Si**licon
PLD	**P**ulsed **L**aser **D**eposition
PLM	**P**ulsed **L**aser **M**elting
PV	**P**hoto**v**oltaic
SAD	**S**elected **A**rea **D**iffraction
SAED	**S**elected **A**rea **E**lectron **D**iffraction

SEM	**S**canning **E**lectron **M**icroscope
SIMS	**S**econdary **I**on **M**ass **S**pectrometry
TEM	**T**ransmission **E**lectron **M**icroscope/**M**icroscopy
TF	**T**hin **F**ilm
TRIM	**TR**ansport of **I**ons in **M**atter
VB	**V**alence **B**and
XEDS	**X**-ray **E**nergy-**D**ispersive **S**pectroscopy
ZA	**Z**one **A**xis

Sample Nomenclature

TABLE 1: An overview of the sample nomenclature when referring to acquired TEM and STEM images/micrographs. All the TEM specimens have been collected close to the center of the pulsed laser melted spot.

	Dopant	**Ordered peak concentration**	**Measured energy fluence**	**Number of pulses**	**Full name**
Units:		[at.% cm^{-3}]	[J cm^{-2}]		
	W	0.1		0	W-D0.1-0P
	W	0.1	0.9	1	W-D0.1-F0.9-1P
	W	0.1	1.8	1	W-D0.1-F1.8-1P
	W	1		0	W-D1-0P
	W	1	0.9	1	W-D1-F0.9-1P
	W	1	1.8	1	W-D1-F1.8-1P
	W	2		0	W-D2-0P
	W	2	0.9	1	W-D2-F0.9-1P
	W	2	1.8	1	W-D2-F1.8-1P

"While inrestigating the cause of such great differences in the resistance of the [selenium] bars, it was found that the resistance altered materially according to the intensity of light to which it was subjected."

Willoughby Smith (1873) [2].

1 Introduction

1.1 The first experimental demonstration

The first documented experimental demonstration of the photovoltaic (PV) effect, was done by Edmond Becquerel in 1839 [3, 4]. Becquerel did this by submerging an electrode in a conductive solution, illuminated the electrode with visible light, and observed that this created an electric current [5]. The current was not remarkably large, but he had nonetheless made the first PV cell. Over 30 years after Becquerel's finding, W. Smith was first out to describe how resistance in selenium bars altered accordingly to light intensity [2]. Then - ten years later, C. E. Fritts managed to build the very first solid state photovoltaic cell, and was convinced that his "[...] cells can be so treated that they will generate a current by simple exposure to light or heat. [...]" [6].

Despite the fact that the first PV cell was built over 150 years ago, photovoltaics did not become a subject of great interest until the early 70's [4]. Research on PV cells - or colloquially named solar cells (which will be used hereafter), is still a hot topic regarding incremental refinement of material quality, design and net efficiency for instance. Therefore - simultaneously as the microelectronic industry tries to manufacture smaller electronic components, solar cell industry aims to accomplish increased solar cell conversion and production efficiency, to oblige sustainable usage and production.

1.2 Different approaches towards solar cell improvements

Solar cell technology has advanced significantly the past decades, with several different approaches. The technology has traditionally been divided into three generations, which can graphically be seen in Figure 1.1. The graph shows possible production costs per unit area, with respect to energy conversion efficiencies [3, 8]. The first (I) generation solar cells, are based on crystalline silicon (c-Si) wafers [8, 9]. This generation, has a typical power performance of 15-20%, commercially [3, 10, 11]. The second generation (II) - known as thin-film (TF) solar cells, use foreign substrates to reduce the amount of absorber materials. These cells are therefore cheaper, but have a smaller power performance than generation I [9, 11, 12]. The third (III) and last generation solar cells, aims to enhance the efficiency of TF devices, or single-crystal III-V materials. This can be done by introducing intermediate energy level(s), between the valence and the conduction band of a host material [8, 9, 12]. Generation III solar cells, are still under development and research. They have therefore not been commercially applied, despite the

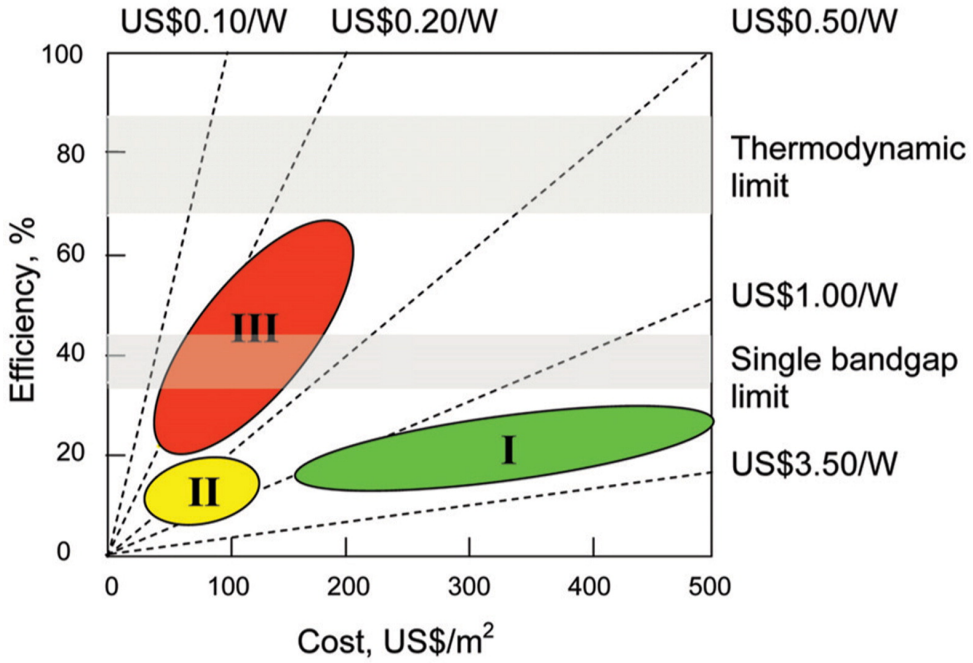

FIGURE 1.1: Efficiency and cost relations for the first (I), second (II) and third (III) solar cell generation. The tinted areas between 31 - 41 % and 67 - 87 % represent the single band gap limit and the thermodynamic limit, respectively. (Acquired from [7].)

possibility of low-cost production and high efficiencies [9].

The concept of intermediate band (IB) solar cells (IBSC) based on deep level impurities, is a relatively young idea. It was first proposed by Luque and Martí in 1997 [14], and has become a field of interest with different approaches [15–19]. An IB material can be manufactured by doping a semiconductor with a transition element, whose energy band(s) does not overlap with the host material's. Instead, it introduces deep centers/levels, to avoid the Shockley-Queisser limit for single bandgap solar cells (graphically shown in Figure 1.1) [20–23]. The centers are generally identified as inductors of non-radiative recombinations [23, 24], but it is believed that recombination of charge carriers can be inhibited if the concentration of impurities is such that the Mott transition is exceeded (typically at approximately 6×10^{19} atoms cm^{-3}) [19, 23–25]. This is schematically shown in Figure 1.2, and is known as hyperdoping.

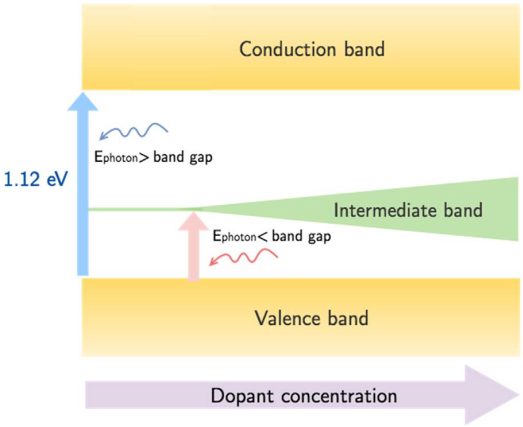

FIGURE 1.2: Schematic of the intermediate band dependency on dopant concentration. (Acquired from [13].)

1.2.1 Silicon as host material

Material requirements for solar cell application can be found in the literature, and the demands are limiting the range of elements that inhibit more than one of the desired qualities. However, of the elemental semiconductors, silicon (Si) complies with several of the criteria, such as it's usable indirect energy gap of 1.1 eV as seen in Figure 1.2 and 1.3 b) [4]. Crystalline silicon (shown in Figure 1.3 a)) has possibly become the most important element for terrestrial use, but amorphous (or non-crystalline) silicon (a-Si) and polycrystalline TF silicon (p-Si) (consisting of microcrystallities or "*grains*" with a typical width of 1 µm), are also of the best developed materials for solar cell applications at present [4].

A lot of the elements believed to produce deep levels in silicon, have a low solubility and high diffusive velocities in solid Si [28]. Therefore, incorporating such elements using non-equilibrium techniques, may result in

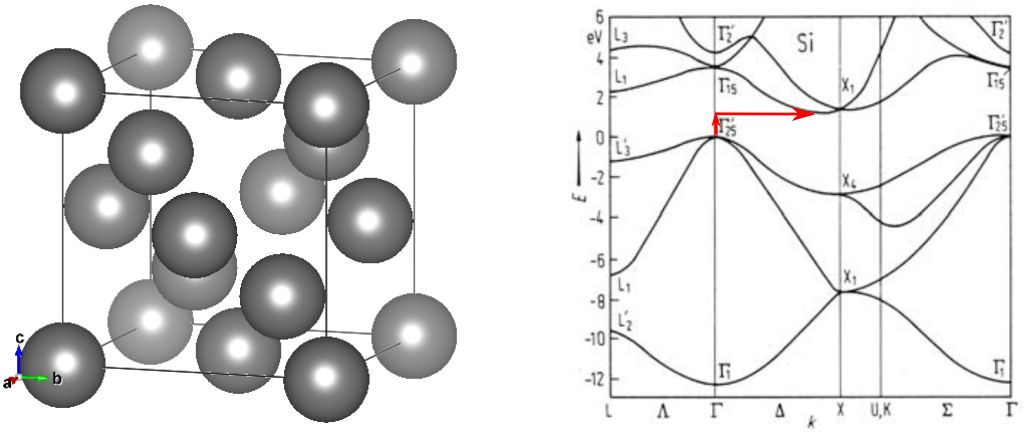

FIGURE 1.3: (a) Visualization of the cubic crystal structure of c-Si, space group Fd$\bar{3}$m (constructed using VESTA software [26].); (b) Band structure of c-Si, depicting energy levels parametrized by k. The red arrows indicates that the band gap is indirect. (Acquired from [27], and further edited.)

dopant concentrations above the solubility limit. Hyperdoping using ion implantation, can be a non-equilibrium first step solution. However, the technique generally degrades the host material quality, due to random collisions between the ions and the host material. Therefore, processes that can offer rapid crystallization, might be of interest. If growth occurs with speeds exceeding the diffusive speed of solute(s) in a liquid, solute concentrations above an equilibrium solid solubility limit (termed "solute trapping"), can be accomplished [29]. Therefore, if an impurity is equally distributed in a silicon matrix, a maximum theoretical efficiency of 54% under ideal conditions, may be achieved [24, 30].

A project at NTNU

In 2015, a project at Norwegian university of science and technology (NTNU), was initiated with the intent of making an IB material. This was done by hyperdoping float-zone silicon (Fz-Si) wafers, with the proposed dopant silver (Ag). This was then followed by rapid recrystallization, using pulsed laser melting (PLM) [31, 32]. However, silver is almost indissoluble in silicon, and was found segregated into complex 3D filamentary structures and local breakups of Ag phases - a phenomena known as cellular breakdown (see Section 2.1.2) [28, 33–38]. A new project was therefore initiated in 2018, using the 74^{th} atomic element tungsten (W) as dopant. W has been ion-implanted in Si wafers, and subsequently recrystallized using PLM with different fluences.

To provide information about the crystal structural and composition of the W-implanted Si samples, transmission electron microscopy (TEM) and energy dispersive spectroscopy (EDS/-X) is done on electron transparent cross-sectional samples. This will constitute the objective of this thesis, and will be further described in the following chapters. A brief comparison of W-implanted and Ag-implanted Si samples, will also be done at the end of the WSi characterization. This will be done to determine whether W may be a better candidate than Ag, regarding dopant incorporation in Si matrices for solar cell application.

In the following, Chapter 2 will cover some theoretical background of the tungsten-silicon system, material processing, and characterization techniques. This involves i.a. W ion-implantation, PLM, focused ion beam (FIB) for TEM sample preparation, imaging techniques in TEM, and elemental characterization using EDS/-X. Chapter 3 will then cover the experimental methods, in more detail. Chapter 4 will present the sample results, with a corresponding discussion of the materials. At the end of Chapter 4, a few comments regarding similarities and differences between the studied W-implanted and the Ag-implanted Si samples, will be presented. The final chapter will then summarize some of the findings, with some concluding marks. This will be followed by some additional suggestions for further work and improvements.

"I have found that the cell is more sensitive to light when the current enters at that surface, which is ordinarily the one covered by the gold or other transparent conductor."

Charles Fritts (1885) [6].

2 Theoretical Background

The present chapter aims to cover some theory about the tungsten-silicon system, before a theoretical introduction of silicon impurity segregation. This will then be followed by a section about material processing using ion implantation and pulsed laser melting (PLM), before introducing the material characterization technique transmission electron microscopy (TEM). This includes TEM sample preparation using focused ion beam (FIB), TEM imaging techniques, and energy dispersive spectroscopy (EDS/-X). Lastly, a Pearson distribution function will be presented, which will be used to model tungsten (W) distribution profiles, acquired using EDS.

2.1 Material properties and impurity segregation

2.1.1 The tungsten-silicon system

It is fairly well established that metallic impurities - such as tungsten (W), leads to device performance degradation in silicon (Si). This is due to the creation of deep levels, acting as carrier trap centers in the silicon band gap [39–41]. Because of the significant reduction in minority-carrier lifetime W may cause, the presence of such a transition metal is typically avoided in Si devices [28, 40, 42–44]. However, if W is introduced in solute concentrations

beyond the equilibrium solubility limit, a filled and an empty energy level may overlap. This may then result in the formation of a single partially filled near mid-gap band, between the valence and the conduction band of Si (see Figure 1.2) [19].

The tungsten-silicon system, has been paid some attention to regarding refractory metal silicides (see Appendix A for some known W silicides). However, as a metallic contaminant in Si, W is one of the least studied [46]. The transition metal has a low solubility in Si as seen in Figure 2.1, and has been reported with a solubility limit of 0.15-0.2 at.% (just above the limit to exceed Mott transition) for temperatures between 837 and 934°C [46]. With higher concentrations, it has been reported that W diffusion promotes formation of W_xSi_y clusters of sizes $1 - 12$ nm, after annealing/dry oxidization. The nature of the precipitates/clusters, could not according to [46] be determined. However, it has been suggested that they may have some connection with the unusually slow, and not completely understood W diffusion mechanism [43, 46, 47].

Recht has already studied tungsten as a deep-level impurity in Si, but only to some extent [48]. In his study, different transition metals were ion implanted in silicon wafers, and subsequently recrystallized using PLM. The

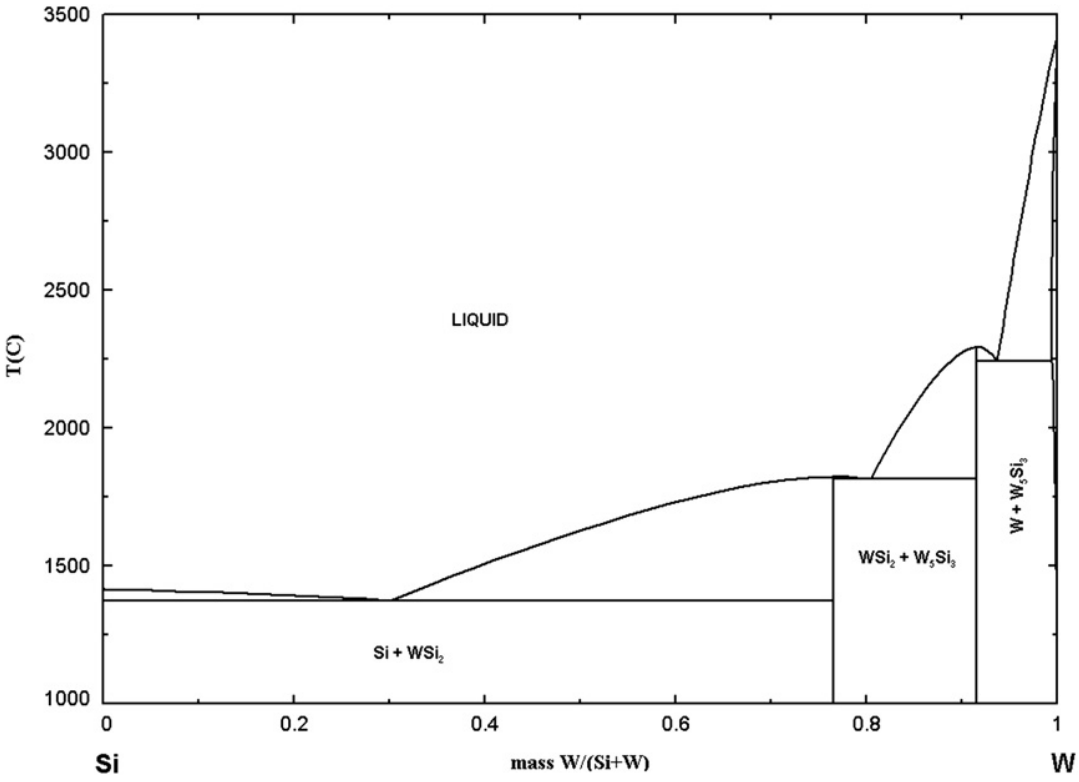

FIGURE 2.1: Equilibrium diagram of the tungsten-silicon system; note that differences can be found in the literature. (Acquired from [45].)

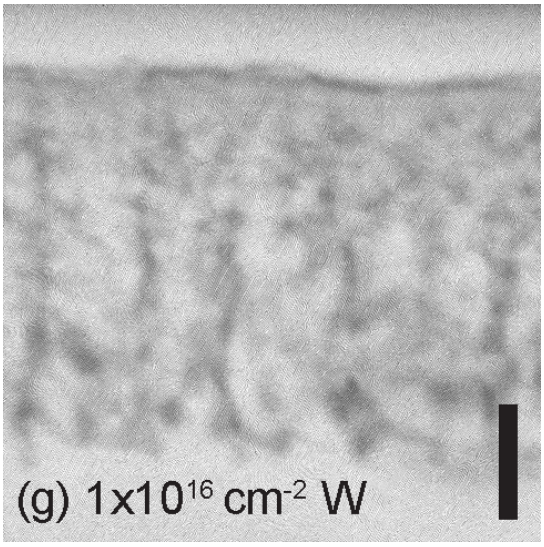

FIGURE 2.2: Cross-section TEM micrograph of segregated W in Si. A carbon layer is seen lying on the top. The scale bar is believed to be approximately 75 nm. (Acquired from the supplementary material of [28].)

tungsten-implanted Si is reported segregated, and a cross-section TEM micrograph of the sample can be seen in Figure 2.2. Despite this, the present project use different material processing parameters, and will therefore also do a further study about W as a contaminant in Si.

2.1.2 Impurity segregation during silicon regrowth

Crystallization is part of silicon purification, since impurities tend to segregate into the Si melt during solidification. This can schematically be seen in Figure 2.3 a). The extent of segregation for a specific impurity, may be described by a segregation coefficient (also known as a partition coefficient) [49]. For impurities in silicon, the segregation coefficient is usually smaller than 1, due to the lower solubility limit in solid Si, than in liquid Si [41]. This does also concern tungsten, which has a segregation coefficient $<< 1$ [41]. This indicates that W is difficult to incorporate in solid silicon, using equilibrium processes.

W is reported to reduce Si recrystallization kinetics after implantation [46], which may be one of many factors that has contributed to the reported W segregation (see Figure 2.2) [48]. However, atomic number, lateral concentration variations and impurity diffusion mechanisms in the melt, may also affect the effective segregation coefficient. Therefore, several parameters can influence crystal growth, and impurity accumulation close to the solid/liquid interface along the growth direction [37, 49, 50].

In principle, a local impurity concentration ought to determine the degree of melting-point depression. This implies that the most impurity rich regions, may cause a local retarded progress in the advancing solidification front [37].

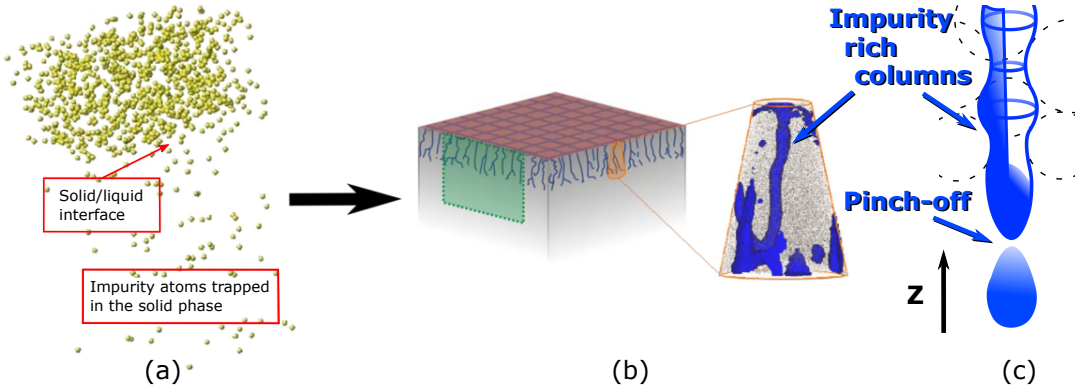

FIGURE 2.3: (a) A snapshot of a simulated evolution of the re-growth of a doped silicon system, where only impurity atoms are present (Acquired from [50], and further edited); (b) Schematic of cobalt cellular breakdown in silicon. The green rectangle illustrates a typical cross-section of a TEM specimen, whereas the blue filaments depict segregated impurities. (Acquired from [37], and further edited.); (c) Schematic of the pinch-off mechanism happening to a contaminent-rich filament, caused by a Rayleigh instability. Radius' of the curvature in the axial direction, are also included.

Lateral concentration variations, can therefore cause impurity accumulations in the liquid. This can further cause a destabilization of the moving liquid-solid interface, through constitutional undercooling. Consequently, this may result in the formation of a characteristic morphology, which is known as cellular breakdown [51–55]. Furthermore, as the interface roughens, impurity segregation can occur laterally with respect to the main solidification front, and cause a creation of precipitate phase "channels" as schematically seen in Figure 2.3 b).

The "channels" of impurity-rich phases, may form continuous impurity rich columns during solidification. However, the columns may also disconnect at a critical length, to a pinch-off mechanism as schematically visualized in Figure 2.3 c). This mechanism is caused by an instability of the cylindrical viscous liquid, and is often called a Rayleigh instability [56]. The pinch-off mechanism has been attributed to the discontinuous morphology of gold-doped silicon, where Rayleigh instability has been amplified by impurity bulk diffusion [38]. The result may therefore be a local breakup in the molten threads of impurity-rich phases, driven by the reduction of interfacial energy.

2.2 Material processing and experimental characterization techniques

2.2.1 Ion implantation and pulsed laser melting

When incorporating impurities with a low solubility limit in a host material, an efficient un-equilibrium method can be to force the dopant (a purposely added impurity) in a matrix as high-energetic ions (see Figure 2.6 i)) [57, 58]. This can be done by accelerating ions from a target, through a mass spectrometer, and onto a silicon wafer for instance. Large concentrations of a impurities may then be achieved. However, due to all the collisions caused by the cascade of ions, the material structure may become degraded and amorphized [4, 59]. A damaged layer may also exist beyond the amorphous/crystalline (a/c) interface, which may be supersaturated with interstitials [60]. This is known as end-of-range (EOR) defects [61–63]. In silicon, the formation of interstitial precipitates may occur from the excess population after ion implantation, and/or after annealing. These defects appears to be rod-like planar defects, which can turn into dislocations in the EOR region (see Figure 2.5 a)) [62, 64–66].

Amorphous implanted silicon may be exploited as a solar cell material, but due to the material quality, charge transport is more energy demanding as opposed to when it is crystalline [4]. Techniques that regain the semiconductor's crystallinity, may therefore be of interest [59]. Pulsed laser melting for instance, can cause large temperature gradients from a single pulse within nanoseconds, and achieve complete crystallization of implant-damaged layers [13]. Thus, if the growth happens faster than the dopant diffusive speed, solute concentrations above the solubility limit in Si may be accomplished [29]. In addition, Aziz and Kaplan have demonstrated that the segregation coefficient increases at high solidification velocities, indicating that dopant incorporation may be accomplished with large enough growth velocities [67].

High non-equilibrium melting, implies thermal expansions at different temperatures. This may cause stress, stacking faults and other deformations in the recrystallizing material [28, 68, 69]. Examples are local lattice distortions, crystal twinning (occur on {111} planes for polycrystalline Si [70, 71]) as schematically shown in Figure 2.4 (with a corresponding electron diffraction pattern), and/or other undesirable defects that may lead to e.g. non-radiative recombinations, and reduction in photocurrent production.

Depending on the implantation depth and laser parameters, undercooled melted material may involve some of the underlying crystalline material, or not. If the former, crystalline layer may act as a seed, and induce resolidification of the dopant rich amorphous region via liquid-phase epitaxy [57, 59]. If the melt does not reach the amorphous/crystalline interface as schematically visualized in Figure 2.5 a) and b), the solidification of the melt may result in large and arbitrary oriented crystals (L-poly) or 'grains' of dimension $0.1 - 1$ µm [73, 75–78]. The grain boundaries are characterised with increased Gibbs energy, implying that such systems may tend to reduce this energy in different ways. This may for instance be done by introducing point defects between the grains, such as foreign atoms. This thermodynamically process, may therefore lead to segregation of dopant elements at the grain boundary [79]. In addition, non-equilibrium processes - such as PLM, may result in non-equilibrium grain boundary segregation. This means that

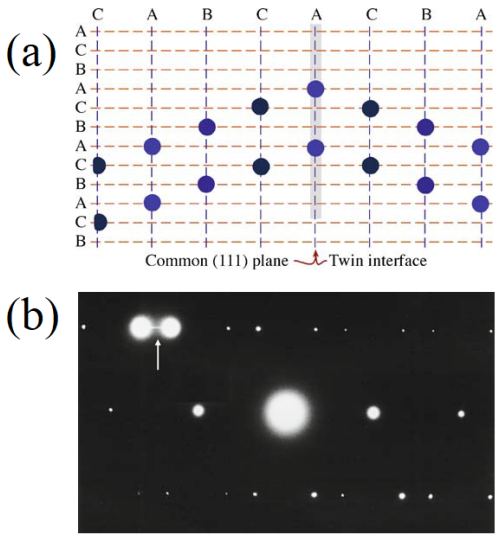

FIGURE 2.4: (a) Schematic of twin, and; (b) electron diffraction pattern (see Section 2.2.3.) with a streak normal to the twin plane. (Acquired from [72].)

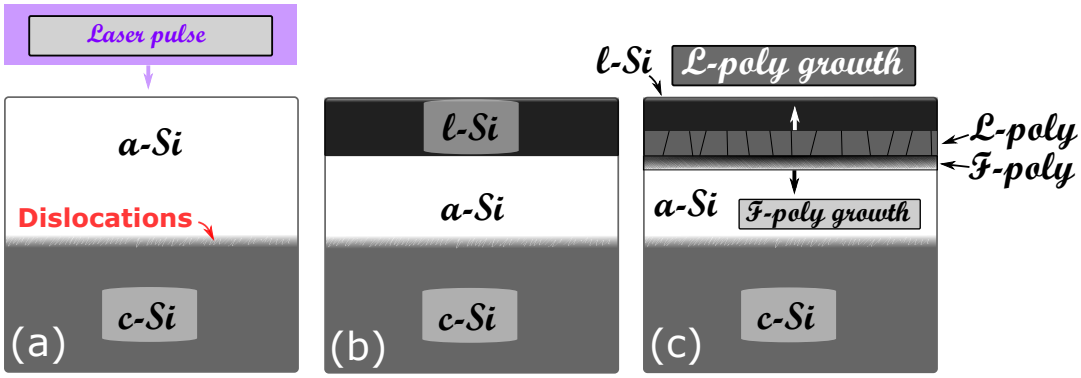

FIGURE 2.5: Schematic cross-sectional overview of laser-annealing amorphized Si, when only parts of the amorphous volume is melted: (a) Cross-section as-implanted sample, showing an amorphous region on top of a narrow layer with dislocation loops; (b) Melting of amorphous material, and; (c) Solidification commences at the liquid/a-Si interface, growing large polycrystalline Si. The recrystallization triggers explosive crystallization, resulting in fine polycrystals. (Inspired by [73] and [74].)

a build up of vacancy-solute pairs around a boundary may occur, to preserve thermal equilibrium [79].

It has been suggested that the crystallization commences at the interface between the amorphous material, and the melt. This implies that energy transfer to the solid amorphous region, may result in a crystallization front of finer polycrystals (F-poly) of dimensions $5 - 10$ nm. This crystallization front is advancing towards the a/c interface, as seen in Figure 2.5 c) [73, 75–78, 80–82]. The phenomena is called explosive crystallization, and is believed to be controlled by the competing heat production, and heat dissipation through conduction [73, 75, 76].

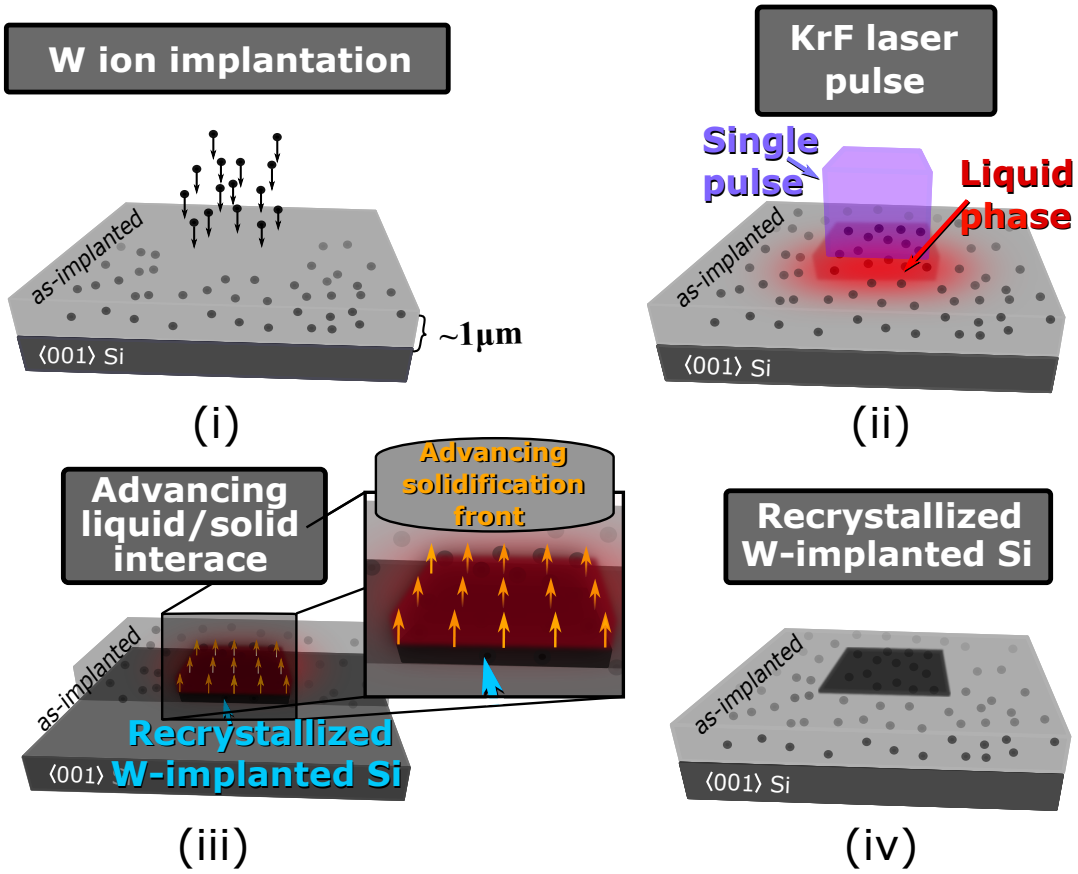

FIGURE 2.6: Schematics of: (i) ion implantation form the IB material by incorporation of a high concentration of W ions in the Si matrix with an implantation depth of roughly 1 µm (cf. chapter 3 and 4); (ii) PLM performed with a KrF pulsed laser to recrystallize the degraded implanted Si; (iii) Rapid solidification recrystallizes the material. If the melt comprises some of the underlying ⟨001⟩ substrate, the crystal may induce epitaxial crystal growth. If not, the recrystallization may lead to two different polycrystalline layers; (iv) Cooled and recrystallized W-implanted silicon, with amorphous/partially crystallized implanted silicon encircling the inflicted PLM volume. Further details about the process, can be found in Chapter 3; Note that the dimensions are not to scale.

An outline of the processing technique conducted on the intended IB materials, is shown in Figure 2.6: (i) A high concentration of tungsten, is ion-implanted in a Si wafer. This leads to defects and damages, due to the cascade of collision events; (ii) Krypton Fluoride (KrF) pulsed laser melting, is used to recover the crystallinity of the material. A short energy pulse is then inflicted onto an implanted area; (iii) Undercooled melt starts to solidify, where a liquid-solid interface advances towards the sample surface; (iv) When cooled, the sample is recrystallized.

2.2.2 Focused ion beam

A dual-beam Focused Ion Beam (FIB), is an instrument that can prepare high-quality samples for further studies on a nanometric scale. It is in principle quite similar to a scanning electron microscope (SEM), where a focused beam of electrons is probing a sample surface to induce signals. However, FIB probes ions as well - typically gallium ions, with a momentum that can cause additional signals for characterization. Nevertheless, perhaps the most prominent properties of FIB, is the ability to nano-mill precise shaped samples on a nanometric scale. This can be done when preparing samples to study using TEM [84]. Since new and more complex materials are manufactured and investigated, the development of a dual-beam FIB as depicted in Figure 2.7, has become a tool of great use [83].

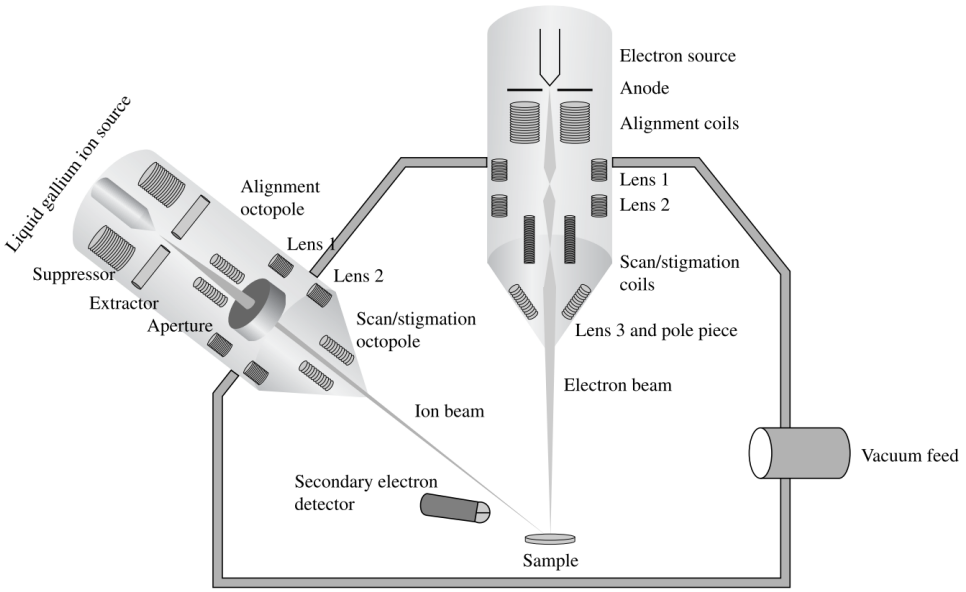

FIGURE 2.7: Schematic illustration of a DualBeam FIB, depicting the ion and electron column in a common chamber. (Acquired from [83].)

Among the different useful qualities FIB exhibits, the ability to exploit the probes to deposit matter, is perhaps one of the most crucial steps during e.g. TEM sample preparation. This can be done by injecting a precursor gas into a working chamber, which is then brought to a selected area for deposition by the probes. The deposition of protective layers, like carbon (C) and platinum (Pt) layers, may then protected a specimen from beam damages, and preserve brittle material characteristics.

2.2.3 Transmission electron microscope/microscopy

The birth of the electron microscope, came with E. Ruska in 1931 [85]. He realized that an electrical current passing through iron caps, could be utilized as magnetic lenses to assist a transport of charged particles (see [86]). Since then, increased functionality and quality in imaging techniques provided by today's TEMs, have gotten material characterization from a micrometer level, to high resolute micrographs from the 'sub Ångstrøm' regime [72].

TEMs exploit the wave nature of electrons, when propagating through specimens with electron transparent thickness'. This may then result in elastic and inelastic scatterings, Rutherford scattering, etc., due to strong interaction mechanisms [72, 87]. The interactions may induce sample characteristic signals, as schematically shown in Figure 2.8. The signals can further be utilized to material characterization (cf. Section 2.2.3 and 2.2.5), and imaging (cf. Section 2.2.3-2.2.4).

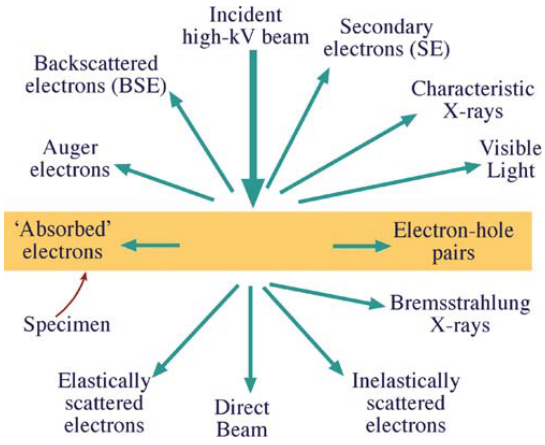

FIGURE 2.8: A schematic illustration of the different signals radiated from a TEM sample when subjected to a high-kilovolt incident electron beam. (Acquired from [72].)

The complete setup of TEM will not be covered in this thesis, but it should be mentioned that the microscope acts as a lens system, with an incident electron beam source, a lens setup and detectors for imaging and material characterization. This can be seen in Figure 2.9 a)-c). Transmitted and scattered electrons can be utilized to create micrographs of a specimen under investigation, either with a broad parallel beam as schematically shown in Figure 2.9 a), or with a focused beam as seen

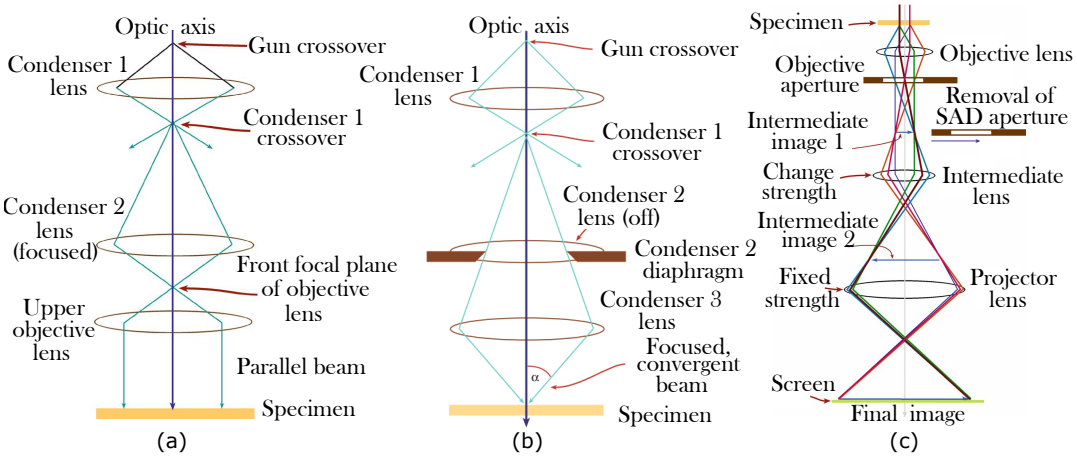

FIGURE 2.9: Highly simplified ray diagram illustrating: (a) Parallel beam operation in the TEM. This is the practical situation in most TEMs, using the Condenser 1 and 2 lenses to image the source at the front focal plane of the condenser-objective plane; (b) Convergent beam/probe mode in a TEM; (c) The final stage of image mode: projecting the image onto a screen. (Acquired from [72], and further edited.)

in Figure 2.9 b). The imaging system then projects the image to detectors, for recording as shown in Figure 2.9 c) (an objective aperture has been inserted in the figure, to conduct bright field (BF) or dark field (DF) TEM. This will be further described in the following). Diffraction can also be done using TEM, which may require the insertion of a selected area diffraction (SAD) aperture (cf. Figure 2.9 c)). Diffracted electrons can then be recorded and form a diffraction pattern (DP), revealing a cross-section of the sample's reciprocal lattice. DPs may be used to acquire information about a material's intrinsic properties, and will be further described in the following.

Diffraction

Diffraction is a phenomena that occurs when an incident wave of wavelength λ, encounters an obstacle or a slit, with a lattice parameter d comparable with λ. If propagating waves - such as incident electrons, is inflicted onto a specimen, corresponding adjacent lattice planes may scatter the electrons such that constructive interference can be described with the following geometric relation:

$$2d \sin\theta = n\lambda. \tag{2.1}$$

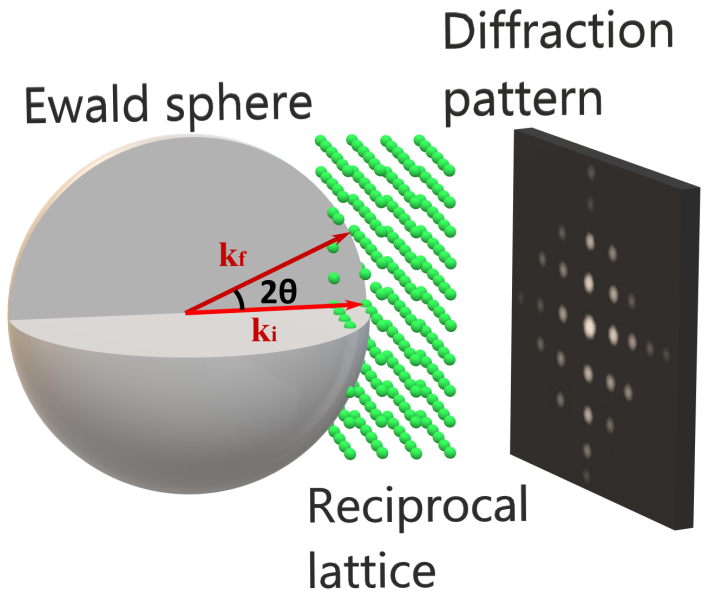

FIGURE 2.10: Schematic of the Ewald sphere, defined by the incoming and scattered wave vectors ($\mathbf{k}_i$ and $\mathbf{k}_f$, respectively). The wave vectors are intersecting an cubic reciprocal lattice. The corresponding diffraction pattern, is shown on the black screen.

Here, θ is the angle measured from the plane, and n is an integer [87, 88]. Equation 2.1 is known as Bragg's law, and can predict constructive interference in reciprocal space.

Incoming and diffracted electrons, can further be allocated an initial and a final wave vector, $\mathbf{k}_i$ and $\mathbf{k}_f$, respectively. If these vectors are positioned in the same origin, and intersect a reciprocal lattice point as depicted in Figure 2.10, constructive interference will occur. Therefore, by constructing a sphere with a radius defined by the length of the wave vectors, the intersection between the so called Ewald sphere and lattice points, can also predict reflections.

As opposed to electromagnetic waves, electrons interfere strongly with matter, and can cause strong interactions with a sample material. Multiple scattering events and/or double diffraction may therefore also happen, implying that re-diffraction or dynamical diffraction may take place due to sample thickness, crystal orientation, and more [72]. As a consequence, the diffraction pattern seen in a TEM, may not necessarily reveal the real projected reciprocal lattice. Nonetheless, such characteristics can reveal properties like orientation, sample thickness, atomic structure, and more.

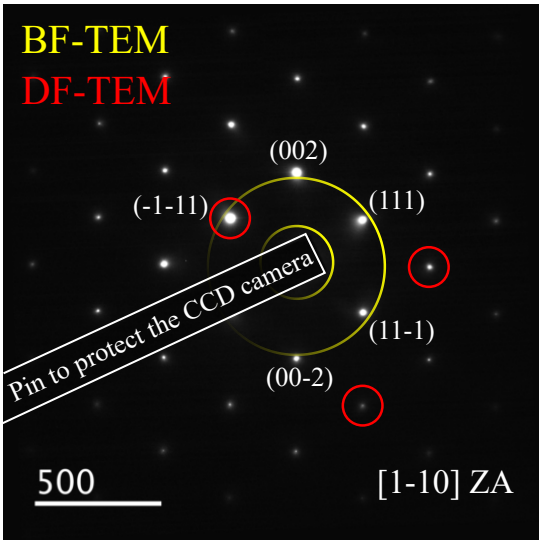

FIGURE 2.11: Diffraction pattern of crystalline Si, on the [1-10] zone axis. The encircling markings illustrate the position of an aperture to do BF-TEM (yellow) and DF-TEM (red). BF-TEM includes the center spot (and perhaps some diffracted electrons), whilst DF-TEM does not. The diffraction pattern has been acquired with a Jem JEOL 2100F, for this purpose only.

Bright field transmission electron microscopy

During selected area electron diffraction, there will consequently be a bright central spot containing all the direct beam electrons. This is depicted and encircled with yellow circles in Figure 2.11 (The center spot in the micrograph is stopped by the pin, to protect the CCD camera). If an objective aperture is positioned in the back focal plane of the objective lens, such that the real space image is projected using the center spot electrons only (and perhaps some of the scattered electrons), the resulting micrograph might be more contrast sensitive. This is because areas that diffract a lot, will turn darker. This technique is called bright field TEM imaging.

Dark field transmission electron microscopy

The second basic imaging technique, is called dark field TEM. DF-TEM is similar to BF-TEM, but instead of positioning an objective aperture in the back focal plane so that transmitted electrons are used to project an image, the aperture is positioned so that a diffracted spot(s) projects the image. This is schematically illustrated with red circles in Figure 2.11, where arbitrary diffraction spots have been chosen for illustration.

2.2.4 Scanning transmission electron microscopy

In addition to the broad-beam techniques described above, a focused/ convergent beam scanning technique, is also a likewise part of the whole of TEM diffraction and imaging [72]. Therefore - in contrast to the parallel recording of static TEM micrographs and diffraction patterns (DP), STEM micrographs

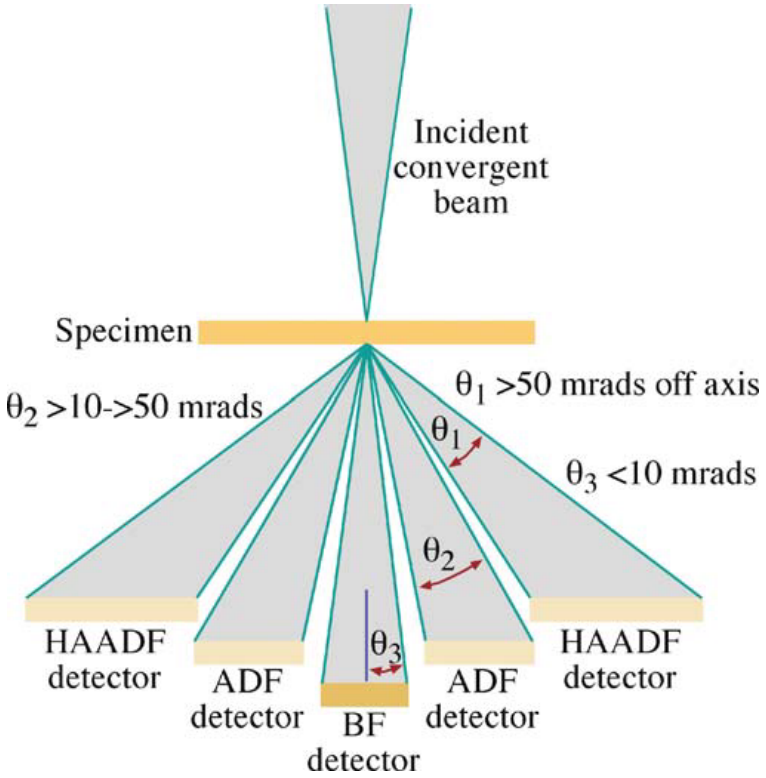

FIGURE 2.12: A schematic illustration of how electrons are transmitted and scattered through a sample, and reaching different detectors to construct a pixel value. (Acquired from [72].)

are built up pixel by pixel, by scanning a focused beam across an area of interest. The scan is done in a raster pattern [89].

The scanning probe has a typical diameter ≤ 1 nm, and may cause a wide range of signals [89]. Therefore - depending on the shape of a detector and the electron scattering angle as seen in Figure 2.12, electrons from a small area on the sample can be detected to form a pixel. The position of the detector with respect to scattered electrons, thus determines the micrograph contrast. However, since the STEM micrograph quality depends on the electron probe formed by the lenses, it consequently has aberration which is limiting the STEM micrograph quality.

Bright field scanning transmission electron microscopy

Bright field STEM, is a mode where a STEM micrograph is put together using electrons that leave the sample at angles smaller than the incident beam convergence angle [72]. This way of constructing micrographs, is analogous to BF-TEM, apart from the pixel by pixel construction [72]. A schematic illustration is shown in Figure 2.12.

High annular angle dark field scanning transmission electron microscopy

In contrast to BF-STEM micrographs, high angle annular dark field (HAADF) STEM micrographs, are constructed using electrons incoherently scattered at relatively high angles with respect to the optic axis. The scatterings can be due to phonon excitations in the specimen under investigation, or Rutherford scattering for instance [89–91]. HAADF-STEM is analogous to DF-TEM, and is often referred to as Z-contrast imaging due to the intensity relation $I \propto \sum_i Z_i^n$, where Z_i is the atomic number of the probed area, and $1.5 < n < 2$ [46, 89]. However, the intensity may also be affected by the structure of the material, leading to a visible contrast difference between e.g. crystalline and amorphous regions of same materials and equal thickness'.

An HAADF-STEM micrograph may be more contrast sensitive from single atoms, compared to annular dark field (ADF) micrographs. The latter technique detects Bragg diffracted electrons (see Figure 2.12) [89], implying that crystal structures can interfere with a Z contrast. The recording of ADF- and HAADF-STEM signals, can be done by inserting an annular detector, through which transmitted electrons may pass unrecorded.

2.2.5 Energy-dispersive X-ray spectroscopy

As mentioned in Section 2.2.3, an incident high-kV electron beam can cause different signals for material characterization. Inelastically scattered electrons, can for instance cause material electrons to excite. This implies that carrier recombinations can cause emission of material characteristic X-rays, accordingly. The unique set of electromagnetic emissions, can then be detected as schematically shown in Figure 2.13, and used for elemental analysis. In TEM for instance, the EDS/-X detector is positioned close to the objective polepiece (seen Figure 2.13), and is counting the number of incoming photons with respect to measured energy. However, since it is difficult to prevent detection of other types of signals from other areas, additional information that is not specimen related, may also be counted as part of the sample spectrum.

Different elements have different probabilities of emitting certain types of X-rays, which among other factors makes it difficult to estimate an element composition. However, a method that can comply with this, is the Cliff-Lorimer technique, which takes the ratio of two elements, A and B, in a binary system [72, 89, 92]. After measuring the above-background characteristic intensities, I_A and I_B simultaneously, the weight percents of each

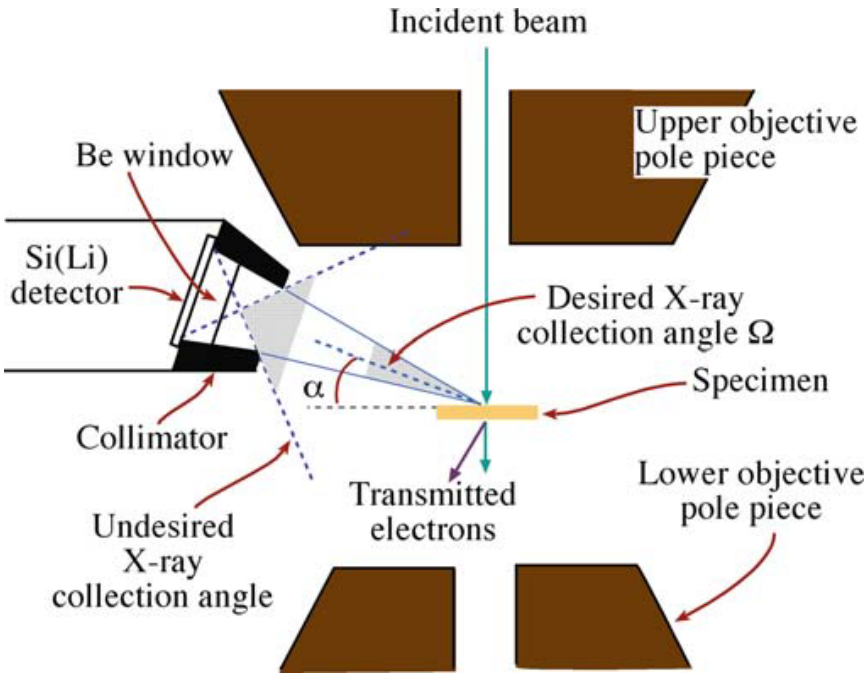

FIGURE 2.13: A schematic interface of incoming X-rays to be detected and the analytical electron microscope. (Acquired from [72].)

element, C_A and C_B, can be related to their respective intensities through the Cliff-Lorimer equation, $C_A/C_B = k_{AB}I_A/I_B$. k_{AB} is often referred to as the Cliff-Lorimer factor, and is a sensitivity factor dependant on the electron microscope/X-ray energy-dispersive spectroscopy (XEDS) system, and operating voltage [72].

Energy dispersive (X-ray) spectroscopy (EDS/-X) can be done using TEM, to quickly acquire information about material composition from an area of interest. However, using EDS in STEM mode, may result in a much higher spatial resolution compared with EDS in TEM mode. Furthermore, EDS in STEM mode is also a very robust, and reliable approach to characterize materials [89]. Therefore, EDS using STEM offer the possibility to acquire material information from points, to two-dimensional maps as shown in Figure 2.14. A spectra from maps for instance, can give information about how elements are distributed in a cross-section sample. However, with a possible lower detection limit of $\sim$ 0.1 wt.% for routine EDS analysis, information about elements at low concentrations may be limited and uncertain [89, 93]. In addition, mapping requires longer acquisition times, because of the the poor efficiency of X-ray generation and detection. This may too affect the detection accuracy [89].

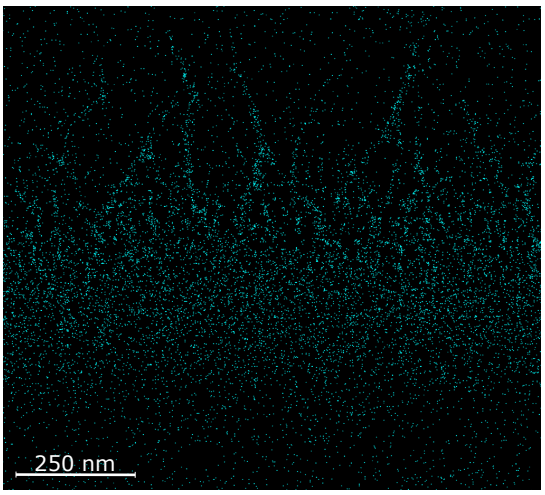

FIGURE 2.14: EDS/-X mapping of tungsten, acquired from one of the studied samples in this thesis.

Pearson distribution profile

A simple method to describe ion implantation profiles, is through analytical functions. The parameters can be determined from experimental spatial moments, implying that different distribution functions may be applied to ion implantation profiles. Pearson distribution functions, can be used to describe ion implantation profiles [94–96]. Therefore, a model that will be focused on in this thesis, is a solution to the Pearson distribution function (p.d.f.), referred to as the type IV.

The p.d.f. is defined as the differential equation

$$\frac{dh(s)}{ds} = \frac{(s-a)f(s)}{b_0 + b_1 s + b_2 s^2}, \tag{2.2}$$

where a, b_0, b_1 and b_2 are constants, and $s = x - [standarddeviation]$ (ΔR_p) [97, 98]. A family of twelve solutions can be derived from the equation above, but only the fourth (IV) distribution will be presented in the following.

The moments of an obtained profile $f(x)$, can be given by

$$R_p = \frac{\int_0^\infty x f(x) dx}{\int_0^\infty f(x) dx}, \tag{2.3}$$

$$\mu_i = \frac{\int_0^\infty (x - R_p)^i f(x) dx}{\int_0^\infty f(x) dx}, \quad \text{for i} > 1, \tag{2.4}$$

where (R_p) is the projected range. ΔR_p, skewness (γ) and kurtosis (β) are related to the moments as follows:

$$\Delta R_p = \sqrt{\mu_2}, \tag{2.5}$$

$$\gamma = \frac{\mu_3}{\Delta R_p^3}, \tag{2.6}$$

$$\beta = \frac{\mu_4}{\Delta R_p^4}, \tag{2.7}$$

where skewness is a measure of the profile tilting, and kurtosis is related to the profile shape. Equation 2.2 can then be solved:

$$a = -\frac{(\beta + 3)}{A} \Delta R_p \gamma, \tag{2.8}$$

$$b_0 = -\frac{4\beta - 3\gamma^2}{A} \Delta R_p^2 \tag{2.9}$$

$$b_1 = a \tag{2.10}$$

$$b_2 = -\frac{2\beta - 3\gamma^2 - 6}{A}, \tag{2.11}$$

where $A = 10\beta - 12\gamma^2 - 18$.

When handling discrete values, the integration can be treated using middle Riemann sum [99]:

$$S = \sum_{i=2}^{N} F\left(\frac{x_i + x_{i-1}}{2}\right) \Delta x, \tag{2.12}$$

where F is a profile, N is the number of pixels in the present context, and Δx is the distance between each pixel.

Depending on the moment values, the solution of Equation 2.2 can be determined by the criteria

$$\kappa = \frac{b_1^2}{4 b_0 b_2}, \tag{2.13}$$

for different domains. In the present work, the Pearson IV distribution has shown promising curve fits, implying that κ has been fulfilling the condition

$0 < \kappa < 1$. The Pearson distribution function IV is given by:

$$h(s) = K \left| b_0 + b_1 s + b_2 s^2 \right|^{\frac{1}{2b_2}} \times \exp\left[-\left(\frac{b_1}{2b_2} + a \right) \frac{2}{\sqrt{4b_2 b_0 - b_1^2}} \arctan\left(\frac{2b_2 s + b_1}{\sqrt{4b_2 b_0 - b_1^2}} \right) \right], \quad (2.14)$$

where K can be determined by adjusting the dose to a desired value. A limitation regarding equation 2.14, is the infinite range of f that experiments does not comply. Therefore, the moments obtained from experimental data, may not be sufficiently close to the required moments to generate accurate curve representations. Therefore, fitting and optimization may be necessary - in particular if original data are noisy [100].

In order to obtain a class IV profile, the following conditions must apply:

$$0 < \gamma^2 < 32, \quad (2.15)$$

$$\beta > \frac{39\gamma^2 + 48 + 6(\gamma^2 + 4)^{\frac{3}{2}}}{32 - \gamma^2}. \quad (2.16)$$

Schematically this can be seen in Figure 2.15. However, in many cases, the above condition(s) are not always met due to experimental limitations. Therefore, in such cases, β may for instance be set equal the limiting value of Equation 2.16 [95].

A quick algorithm to reduce noise in a data set, is to apply median filters. A mathematical representation may be written as:

$$y_j = \frac{1}{2n+1} \sum_{i=j-n}^{j+n} y_i, \quad (2.17)$$

where y_j and y_i are data values, and n is an integer. In this context, a window size of five will be applied to each entry, implying that $n = 2$. In order to handle boundary issues, the first/last value can be repeated. This implies that when $j = 0$ and $j = N$, the window size will be reduced to four, and $2n + 1 \rightarrow 2n$.

In order to optimize the representation of a profile, mean squared error (MSE) to estimate the average squared difference between estimated values and actual estimations, can be applied. A mathematical representation may

be written as

$$\text{MSE} = \frac{1}{N}\sum_{i}^{N}(Y_i - \hat{Y}_i)^2, \tag{2.18}$$

where Y is an observed value, and $\hat{Y}$ is the corresponding value of the fitted curve in this context. Thus, by optimizing MSE with respect to Equations 2.5-2.7, a more accurate fit may be obtained.

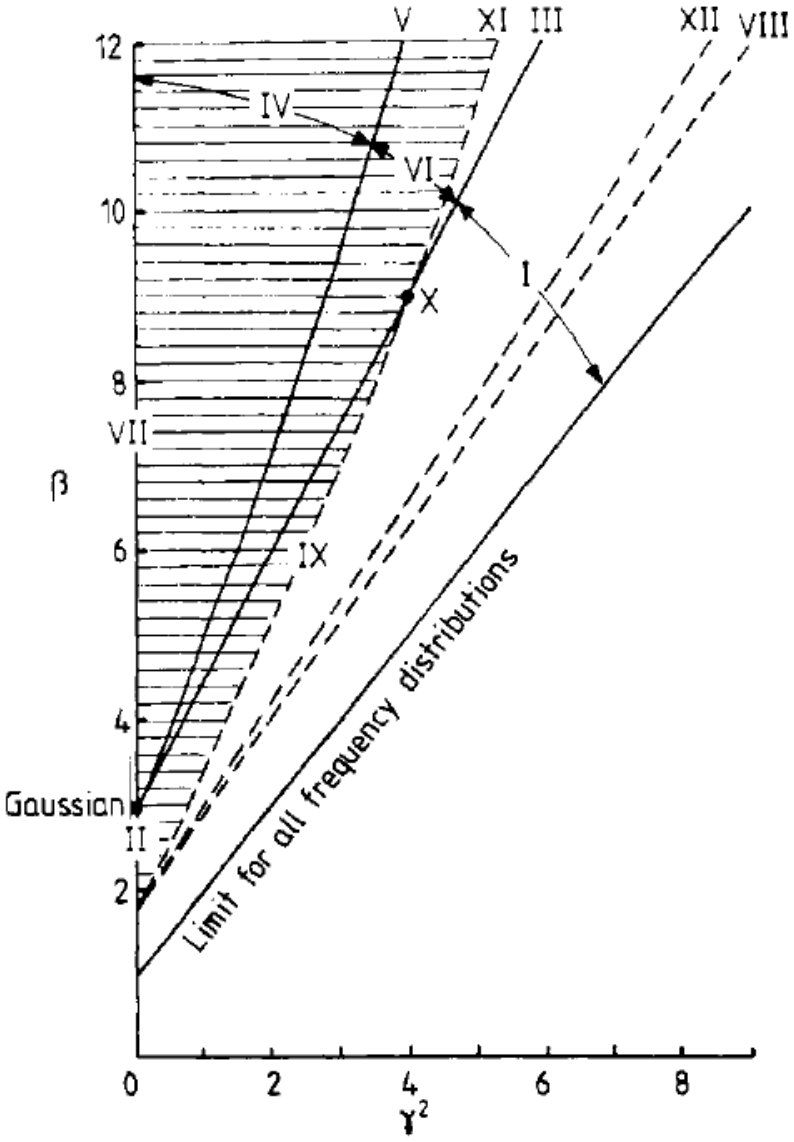

FIGURE 2.15: Domains of validity of Pearson types on the $\beta - \gamma^2$ plane. (Acquired from [100].)

"I have put one of the two platinum plates, previously heated to red hot, on one of the sides of a glass box which has been blackened except for the side on the opposite of the plate. Then having exposed the plate to the different colour beams of the sun light spectre, obtained by diffracting direct sun beams, we got an electric current only when the plate was exposed by the purple and blue beams."

[Translated] Alexandre-Edmond Becquerel (1839) [5].

3 Experimental Details

In the following, experimental details about the instruments and techniques used for material characterization, will be further explained. This includes a more thorough and detailed description of the ion implantation, and subsequent conducted pulsed laser melting (PLM). The latter processing, is inspired by [101]. This will then be followed by a step-by-step description of the transmission electron microscopy (TEM) sample preparation, using DualBeam focused ion beam (FIB). From now on, 'sample' will be used when referring to TEM samples, whilst 'bulk sample' will be used when referring to the bulk material. The chapter will wrap up the experimental details about the used electron microscope, employed to characterize cross-sectional W-implanted Si samples. The used TEM is located at the TEM Gemini centre, NTNU/SINTEF.

3.1 Ion implantation

As mentioned in Chapter 1, the present project is a new attempt to make an intermediate band material by hyperdoping Float-zone (Fz) silicon wafers, but with tungsten (W). Five Fz-Si wafers is ion implanted with W at The Ion Beam Centre of University of Surrey, with concentrations above, and underneath tungsten solubility limit in silicon. The samples can schematically be

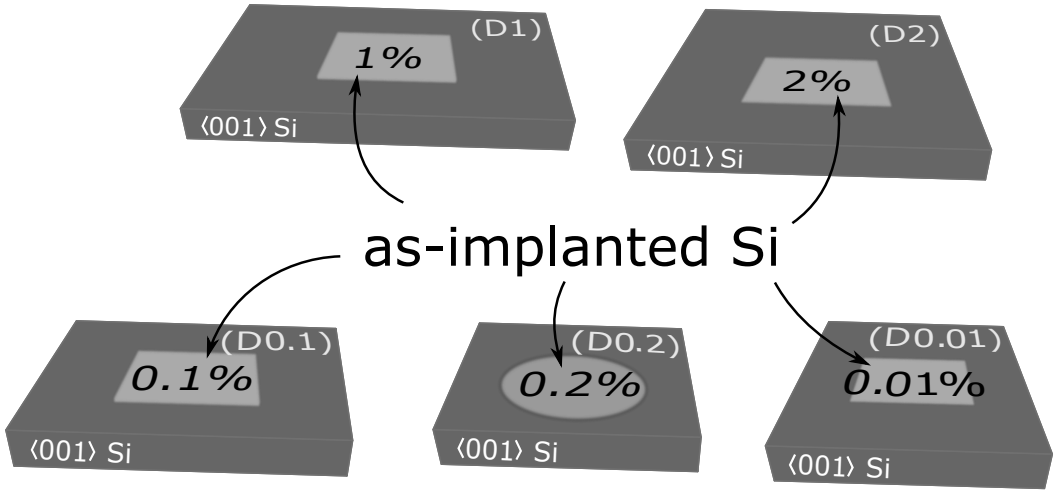

FIGURE 3.1: Schematic of the five W ion-implanted float-zone silicon wafers. The written percentages refer to their respective W peak concentrations. Note that the sizes of the wafers are not scaled, but are to illustrate their mutual shapes.

seen in Figure 3.1, where the shapes of the wafers were predetermined in advance of the implantation. This is to separate the bulk samples from one another. The samples are to have a W peak concentration of 0.01, 0.1, 0.2, 1 and 2 at.%. The implantation is done from an angle of 7° with respect to the wafer surface area vector $\langle 001 \rangle$, to reduce channeling.

The implantation dosage profiles were simulated in advance of the ion implantation, using the software "Transport of Ions in Matter" (TRIM). The implantation parameters used, are shown in Table 3.1. Identical ion energies are used to get an approximately 1 µm thick implantation layers, and a peak concentration at approximately 0.5 µm underneath the sample surface. The general estimated profile using TRIM, is shown in Figure 3.2. The Ion Beam

TABLE 3.1: Implantation parameters necessary to obtain a peak concentration corresponding to the different "dosages," positioned at approximately 0.5 µm from the sample surface. The parameters are based on TRIM simulations conducted by Lysne [102].

Dosage	**Peak concentration** [atom/cm^2]	**Ion Energy** [keV]	**Position of peak** [µm]
0.01	5×10^{18}	1800	~ 0.5
0.1	5×10^{19}	1800	~ 0.5
0.2	1×10^{20}	1800	~ 0.5
1	5×10^{20}	1800	~ 0.5
2	1×10^{21}	1800	~ 0.5

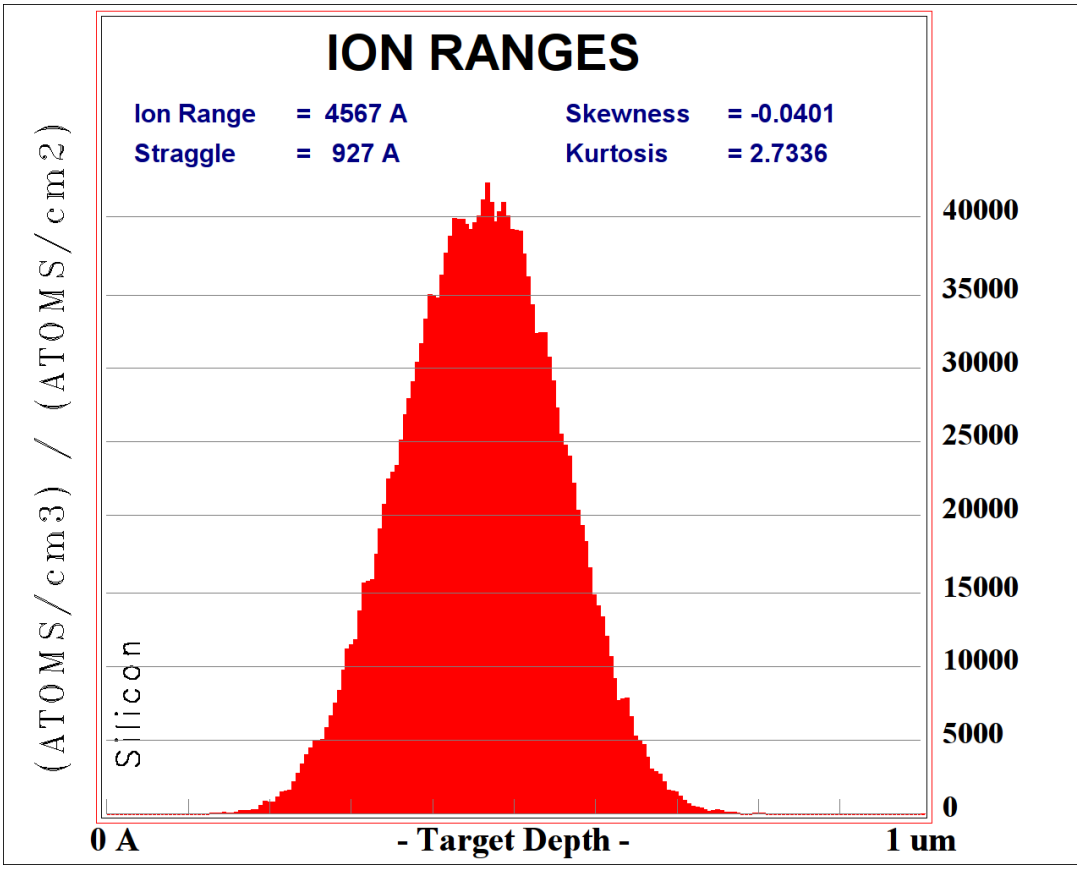

FIGURE 3.2: The distribution profile for W implanted Si, based on TRIM simulations. The calculation has been conducted by Lysne [102].

Centre did not report ion fluence in terms of *atoms* cm^{-2}. Instead, the centre reported target and received counts, which is why ion fluence is not given here.

3.2 Pulsed laser melting

After ion implanting five Fz-Si wafers with five different concentrations of tungsten, the doped Si-wafers are annealed with a single laser pulse using PLM. This is done to regain some of the bulk material's crystallinity. PLM is conducted on a self-constructed system adapted by Hauge, and is based on a pulsed laser deposition (PLD) system with a COMPex Pro KrF exicmer laser from Lambda Physik NovaTube technology. Data about the conducted PLM experiment, can be seen in Table 3.2. Note that some of the parameters corresponding to different samples, will from now on be abbreviated in the sample nomenclature. The nomenclature goes as follows: W-D[*at.%*]-F[*conducted laser fluence*]-[*number of pulses*]P (see Table 3.4). Details about the laser, can be found in Table 3.3.

TABLE 3.2: Experimental PLM parameters conducted on dosage 0.1, 1 and 2 in the PLD chamber. The estimations are done by H. Lysne [102].

Voltage [kV]	**Laser fluence** [J cm^{-2}]	**Laser fluence error** [J cm^{-2}]	**Recrystallized spot size** [cm^2]	**Spot size error** [cm^2]
20	0.91(8)	0.06(6)	0.0363	10^{-5}
30	1.88(8)	0.13(5)	0.0363	10^{-5}

TABLE 3.3: KrF excimer laser (from Lambda Physik) specifications. (Acquired from [32].)

Property [atom/cm^2]	**Value** [keV]
Wavelength [nm]	248
Maximum pulse energy[1] [mJ]	400
Maximum average power[2]	30
Pulse duration [ns]	25
Beam dimension [mm^2]	$24 \times [5, 10]$
Maximum voltage [V]	30

1 Measured at low repetition rate (5 Hz)

2 Measured at maximum repetition rate

3.3 Sample preparation and characterization

3.3.1 TEM sample preparation using focused ion beam

TEM sample preparations are conducted by H. Lysne, using FEI Helios NanoLab DualBeam Focused Ion Beam (FIB), equipped with an FEI easylift. The preparations are conducted at NTNU NanoLab. The present section, is therefore a process description based on documentations from Lysne.

When preparing a silicon specimen to be examined with a transmission electron microscope, it is crucial that the sample has a thickness of approximately 100 nm or less, to be electron transparent. It should also have a width of approximately 15 µm, to have some area to investigate. Lastly, the TEM sample ought to have a length of $15 - 30$ µm too. This is necessary to avoid beam damages on the implanted area, when the second last milling process underneath the sample is being done (cf. step 4 below).

The sample preparation process constitutes nine steps, in course features. These are further described below, with a corresponding matrix showing

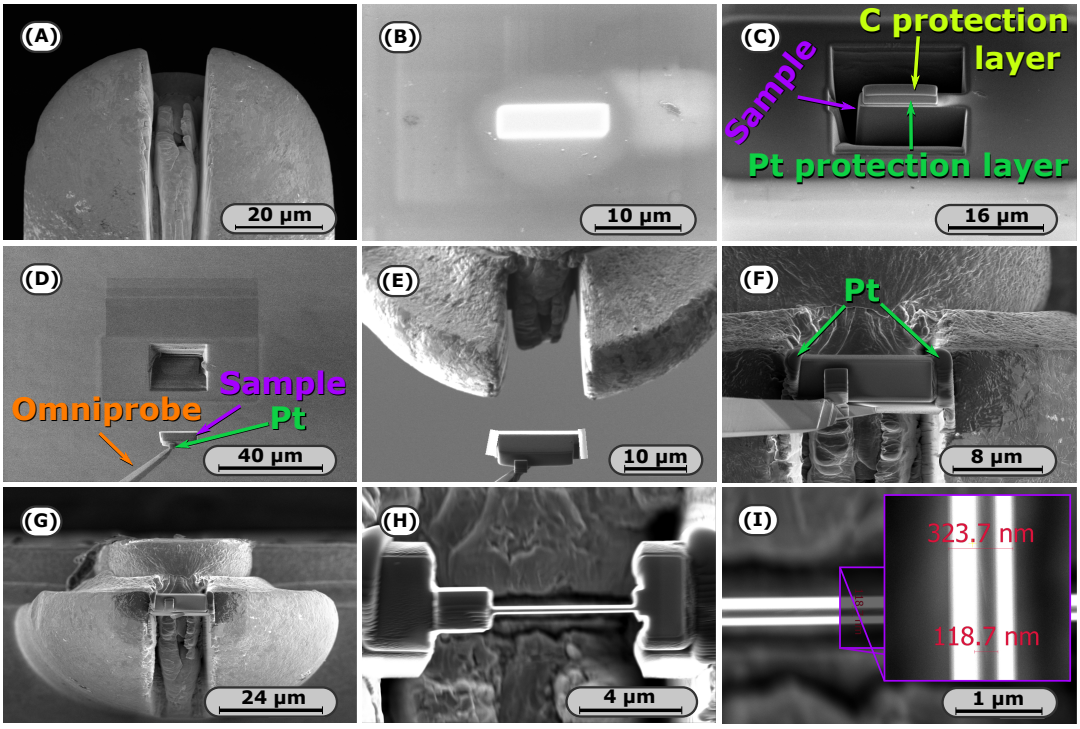

FIGURE 3.3: An array of SEM micrographs illustrating some of the steps during TEM sample preparation with FIB: (A) A finger of a TEM Cu-grid, milled to an H-bar; (B) Depositing C and Pt onto the sample; (C) TEM sample being milled out; (D) The TEM sample attached to an omniprobe; (E) The TEM sample being relocated into the H-bar; (F) Attaching the TEM sample to the H-bar; (G) TEM sample after detachment from the Omniprobe; (H) Thinning down the TEM specimen; and (I) Measuring the thickness of the TEM sample. All the micrographs have been acquired by Lysne.

scanning electron microscopy (SEM) micrographs from a TEM-sample preparation. The micrographs have been acquired by Lysne, and can be seen in Figure 3.3.

1. If the TEM sample is to be properly fastened from two sides, use the ion beam to mill off copper (Cu) from the middle of the tip of a FIB TEM grid finger, to make an H-bar as shown in Figure 3.3A. The finger depth ought to be approximately $15 - 30$ µm, whereas the width should be approximately $15 - 20$ µm. If the TEM specimen is to be fastened on just one of the sample sides, this step is superfluous;

2. Deposit a protective layer of platinum (Pt) and carbon (C) with the electron and ion beams respectively, onto a pre-selected area of approximately 1 µm $\times$ 15 µm as shown in Figure 3.3B;

3. Exploit the ion beam to remove matter surrounding the TEM sample from three sides, by wedge-cut digging. The result is illustrated in Figure 3.3C;

4. Remove matter underneath the TEM sample. The TEM sample is now only fastened to the bulk material on one sample sides, as shown in Figure 3.3C;

5. Attach a precision controlled needle FEI easylift onto the specimen, by depositing more platinum between the sample and the needle. This is followed by radiating away the remaining bulk matter from the specimen. The FEI easylift is then used to lift off, and relocate the TEM sample as shown in Figure 3.3D-E;

6. The relocated sample is now to be positioned in the H-bar TEM grid finger (see Figure 3.3A), after the grid and the sample are oriented and aligned properly with respect to each other. The sides of the specimen should almost be in touch with the H-bar on both sides, and close to the tip as illustrated in Figure 3.3E and 3.3F. If the TEM specimen is to be fastened to the grid finger with one sample side (i.e. no H-bar has been milled), the sample ought not to be fastened and aligned to the tip of the grid finger. Instead, it should be fastened to one of the finger's sides, in order to be less exposed.

7. The TEM sample is fastened to the TEM grid by depositing platinum along the finger/sample interface(s), as shown in Figure 3.3F;

8. When the sample is fastened to the finger, the FEI easylift is detached from the sample. This is done by milling off the Pt, which is holding the needle and the sample together. The result can be seen in Figure 3.3G;

9. The sample needs now to be thinned to a thickness of approximately 100 nm, using the ion beam. It is crucial that the thinning is done in steps, to avoid beam damages. Figure 3.3H-I show the sample after thinning.

3.3.2 Transmission electron microscopy characterization

The cross-sectional TEM samples prepared for characterization, are from D0.1, D1 and D2. The samples are both as-implanted, and recrystallized using a mere laser pulse with measured intensities of $0.9\,\mathrm{J\,cm^{-2}}$ and $1.8\,\mathrm{J\,cm^{-2}}$. An

TABLE 3.4: An overview of the sample nomenclature when referring to acquired TEM and STEM micrographs. The specimens are prepared from approximately the center of the recrystallized area.

Dopant	As-implanted peak concentration	Measured energy fluence	Number of pulses	Full name
Units:	[at.% cm^{-3}]	[J cm^{-2}]		
W	0.1		0	W-D0.1-0P
W	0.1	0.9	1	W-D0.1-F0.9-1P
W	0.1	1.8	1	W-D0.1-F1.8-1P
W	1		0	W-D1-0P
W	1	0.9	1	W-D1-F0.9-1P
W	1	1.8	1	W-D1-F1.8-1P
W	2		0	W-D2-0P
W	2	0.9	1	W-D2-F0.9-1P
W	2	1.8	1	W-D2-F1.8-1P

overview of the characterized samples, is shown in Table 3.4. Their respective nomenclature, can also be seen in the table.

TEM image acquisition

The TEM characterization of the W-implanted Si samples, is done using a Jeol JEM-2100F - a high-resolution analytical electron microscope, with a field emission gun. The microscope is operating at an acceleration voltage of 200 kV. A schematic of the TEM, can be seen in Figure 3.4. To acquire good micrographs and do Bright Field (BF), Dark Field (DF) TEM and diffraction, the specimens were loaded on a sample holder EM-31640 Specimen Tilting Beryllium Holder, as depicted in Figure 3.5 [103, 104]. The holder can tilt a TEM sample in both X- and Y direction, with a maximum tilting range of approximately $\pm 30^{\circ}$ in both directions [104]. The TEM is also equipped with JEOL STEM detectors, which are controlled by Gatan Digiscan for the Digital Micrograph Software [105].

The final intensity adjustments are done using the freeware program Gatan Microscopy Suite (GMS) Software 3 [106], and the public domain Java image processing and analysis program ImageJ [107, 108]. Note that approximately all the TEM-micrographs presented in Chapter 4, will be intensity adjusted, using a non-linear gamma function to get adequate contrasts between characteristic features.

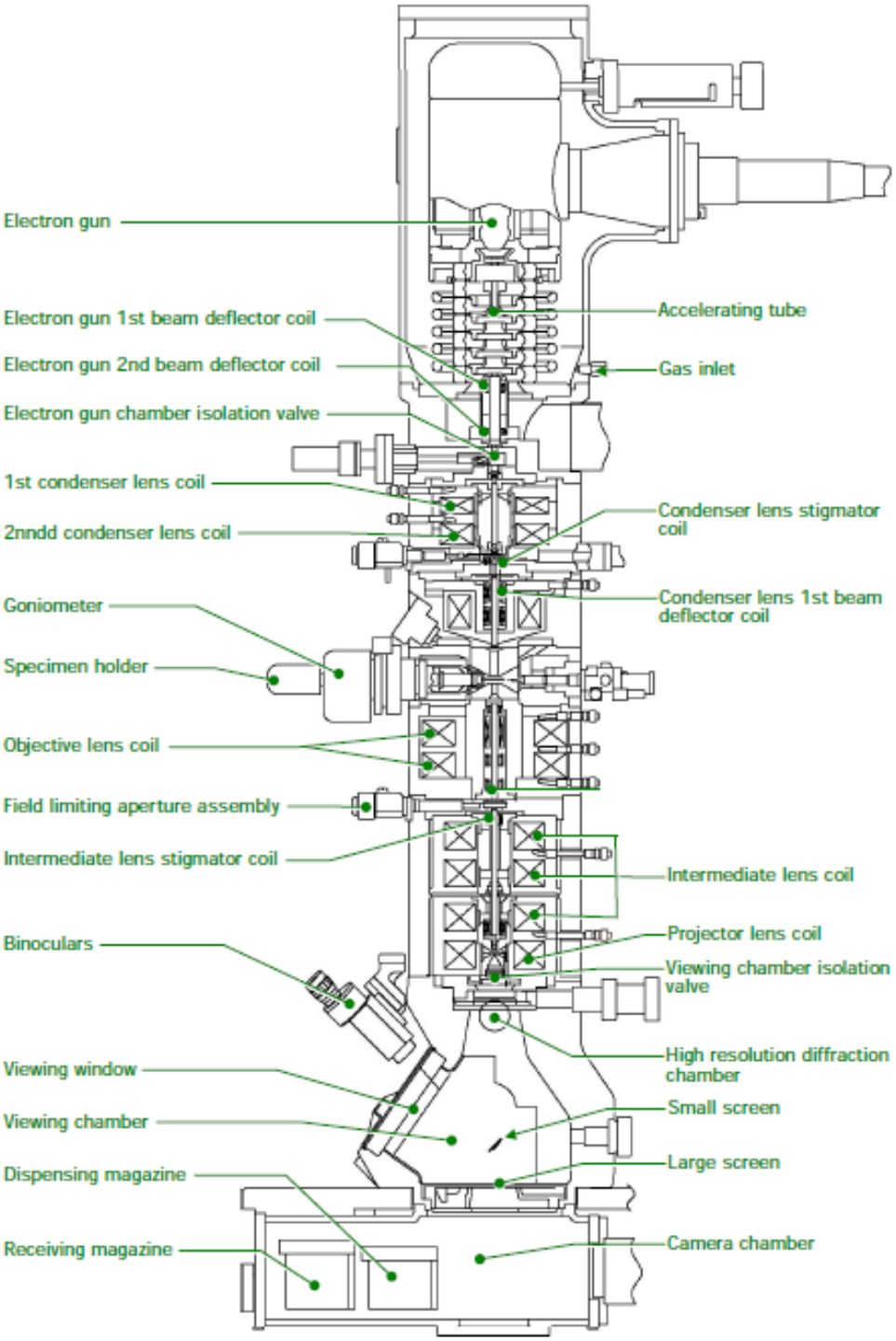

FIGURE 3.4: Schematic of the JEM-2100F field emission electron microscope. (Acquired from [103].)

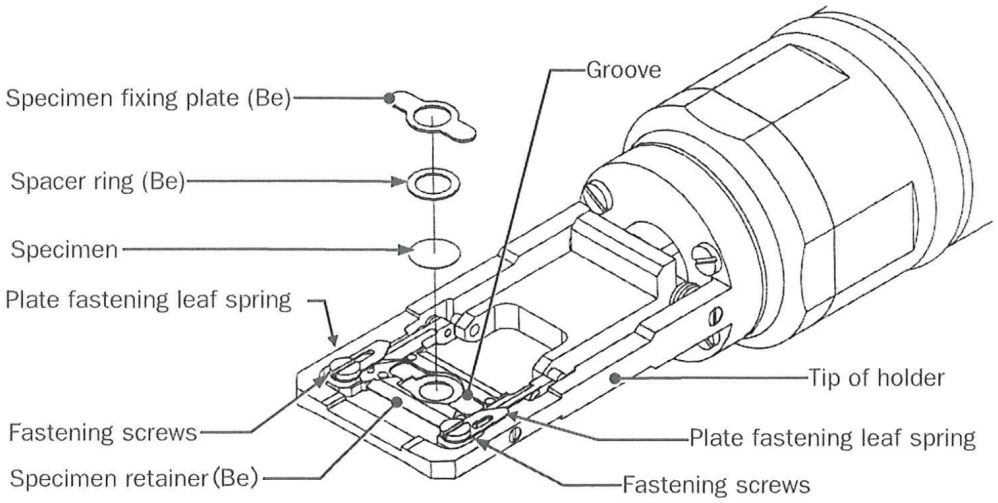

FIGURE 3.5: Schematic of the EM-31640 Specimen Tilting Beryllium Holder tip. (Acquired from [104].)

3.3.3 Energy dispersive spectroscopy

Element distribution characterization of TEM samples using area energy dispersive spectroscopy (EDS), is conducted using STEM mode. The JEM-2100F is operating at a voltage of 200 kV. The probe has a diameter of 1 nm, whilst the acquisition is done using a magnification of $\sim$ 120k. The EDS detector exploited, is an Oxford X-max (80 mm^2) SDD, with a MnKα resolution of 129 keV [109, 110].

Acquired EDS-maps of tungsten are read and processed using Matlab. The raw data parallel with the sample surface, is summed into a vector containing counts with respect to sample depth. The lists are subsequently treated with median filtering, before a possible curve fitting using a Pearson IV distribution function (cf. Equation 2.14).

"In the earlier stages of my investigations, before the discovery of this dual state and of the method of changing a cell from the insensitive to the sensitive condition, hundreds of cells were made, finished, and tested, only to be then ruthlessly destroyed and melted over, under the impression that they were worthless. Now, I consider nothing worthless, but expect sooner or later to make every cell useful for one purpose or another."

Charles Fritts (1885) [6].

4

Results and Discussion

In the following, results from the transmission electron microscopy (TEM) characterization of tungsten (W) -implanted silicon (Si), will be presented. This will be done with a corresponding discussion of the results. The studied cross-sectional samples are three as-implanted samples, prepared from bulk samples with W peak concentrations of 0.1, 1 and 2 at.%. The peak concentrations are expected to be located approximately 0.5 µm underneath the sample surface. The samples are further anticipated to be amorphized after the W ion-implantation, implying that crystalline silicon (c-Si) is located underneath/beside. A damaged region between the amorphized Si (a-Si) and the c-Si, is expected to contain damages and dislocations after the ion-implantation; a schematic cross-section of an as-implanted specimen, is shown in Figure 4.1 (I). A carbon (C) and a platinum (Pt) protection layer are also included in the figure, which are deposited during TEM sample preparation (see Section 3.3.1).

In addition to the as-implanted samples, six recrystallized specimens from the mentioned bulk materials of different W concentrations, will also be studied. In these samples, W is expected to segregate to some extent, into WSi precipitates due to the low solubility in solid Si (see Section 2.1.1). This is schematically shown in Figure 4.1 (II) and (III). Of the recrystallized samples, three specimens are anticipated not completely recrystallized, when using a

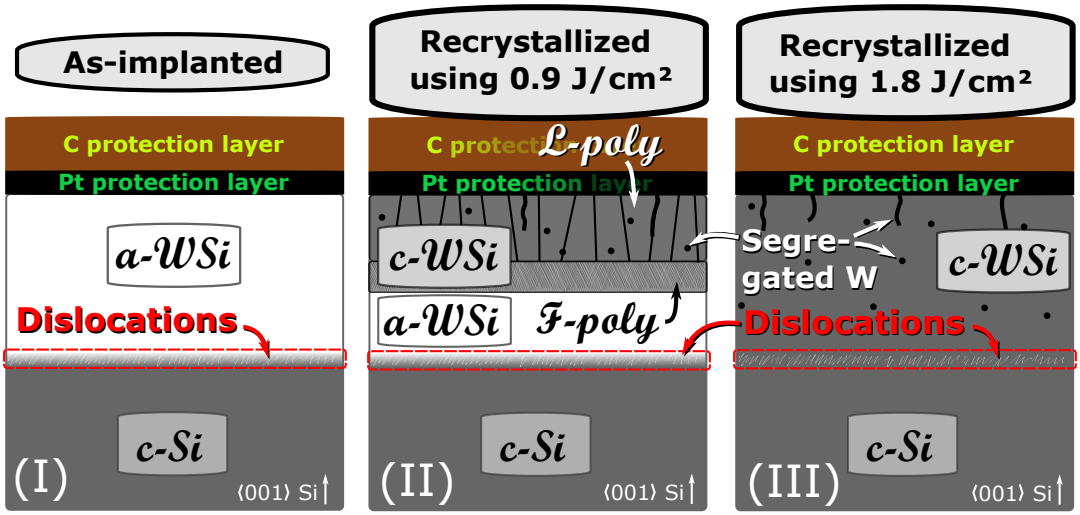

FIGURE 4.1: Schematic overview of cross-section TEM samples, prepared from a bulk Si sample. The schematics illustrate expected characteristic features: (I) As-implanted sample with an amorphous layer on top of crystalline Si, and a damaged region in between; (II) A sample that is not completely recrystallized, containing four different layers: A polycrystalline layer of larger grains, a polycrystalline layer of small grains, a remaining amorphous layer and the crystalline Si; (III) A completely recrystallized sample, with a small region of defects and dislocations from the pre-a/c interface. It is expected that some of the dopant has segregated into WSi precipitates after conducted PLM. Note that the dimensions are not to scale.

laser fluence of $0.9\,\mathrm{J\,cm^{-2}}$. These samples are expected to contain two different polycrystalline regions, a remaining amorphous region, and the underlying c-Si. The polycrystalline regions should consist of large and fine crystal grains, which will be defined as grains of sizes $0.1 - 1$ µm and < 0.1 µm, respectively. The areas are therefore abbreviated to L-poly (large polycrystals) and F-poly (fine polycrystals). A schematic is shown in Figure 4.1 (II). The remaining three recrystallized TEM samples, should be completely recrystallized using a laser fluence of $1.8\,\mathrm{J\,cm^{-2}}$. A region close to the pre-a/c interface, is anticipated to contain dislocations and other defects, as seen in Figure 4.1 (III).

The following characterization of the W-implanted Si samples, will take place in the following order: an as-implanted sample prepared from the 0.1 at.% bulk sample, will be characterized first. Characterization of the not-completely recrystallized sample will subsequently be presented, followed by the characterization of the completely recrystallized sample. The dosage 1 and 2 samples, will be characterized accordingly, in the same order.

The material characterization involves a presentation of sample representative bright-field (BF) TEM micrographs, along with representative selected

area electron diffraction (SAED) patterns. A mean amorphized depth will be given for the as-implanted samples, along with a corresponding standard deviation. In addition, a mean depth of the region with apparent dislocations, will also be given. The estimations are calculated from five measurements. Other characteristic features will also be measured, but depends on how well they are defined in the micrographs. In these cases, ten measurements will be done to get better statistics. All measurements are rounded to the closest hundredth, in µm. Furthermore, high angle annular dark field (HAADF) scanning TEM (STEM) and/or BF-STEM micrographs, will subsequently be presented to give more information about dopant distribution. The depth of evident dopant segregation, will also be estimated. To distinguish different present morphological W-rich clusters from filaments, filament precipitates will in this context be defined as impurity-rich columns of length greater than 50 nm.

A plotted graph from energy dispersive X-ray spectroscopy (EDS) mapping, will subsequently be presented. Due to the detection limit using EDS, the plot will only be presented with the intent of giving a schematic overview of tungsten distribution. Some of the profiles will be fitted to a Pearson IV distribution profile, along with a corresponding optimized profile. Estimated mean square error (MSE) will also be given, but are only intended as an indication on how good/bad an experimentally fitted curve is compared to a corresponding optimized curve. After all the samples from one bulk material has been characterized, normalized W distribution curves will subsequently be presented and discussed.

At the end of the chapter, the studied recrystallized WSi samples will be summarized. This will then be followed by a brief discussion of similarities and differences between the characterized W-implanted Si samples, and the previous studied Ag-implanted Si samples.

The characterized samples are abbreviated with respect to dopant (W), nominal as-implanted W peak concentrations, and PLM parameters. Recrystallized samples can not be expected to have equal W concentrations as the nominal peak concentrations, which is why '*dosage*' (D) will be used in the sample abbreviation. Samples prepared from the bulk materials of 0.1 at.%, 1 at.% and 2 at.%, are abbreviated as '*D0.1*,' '*D1*' and '*D2*', respectively. Used laser fluences - 0.9 J cm^{-2} and 1.8 J cm^{-2} (see Section 3.2), are abbreviated as '*F{0.9, 1.8}-1P*' (1P stands for one laser pulse). The nomenclature is therefore '*W-D{0.1, 1, 2}-0P*' for as-implanted samples, and '*W-D{0.1, 1, 2}-F{0.9, 1.8}-1P*' for recrystallizes samples.

4.1 Samples of dosage 0.1

4.1.1 W-D0.1-0P

A BF-TEM micrograph of the as-implanted TEM sample W-D0.1-0P, is shown in Figure 4.2. Three corresponding diffraction patterns, are also included. The acquired diffraction patterns (DPs) are done with apertures positioned approximately where the red circles are positioned in the micrograph. The circle dimensions, are only approximate. A platinum (Pt) protection layer from TEM sample preparation using focused ion beam (FIB), can also be seen in the micrograph. The Pt layer is defining the interface between the protection layer, and the as-implanted sample surface.

SAED1 shows characteristic amorphous rings, implying that the W ion-implantation has amorphized the crystalline Si (c-Si). A sample characteristic feature is appearing when doing BF-TEM, and can be seen in the apparent dark region where SAED2 is done. SAED2 reveals weak amorphous rings,

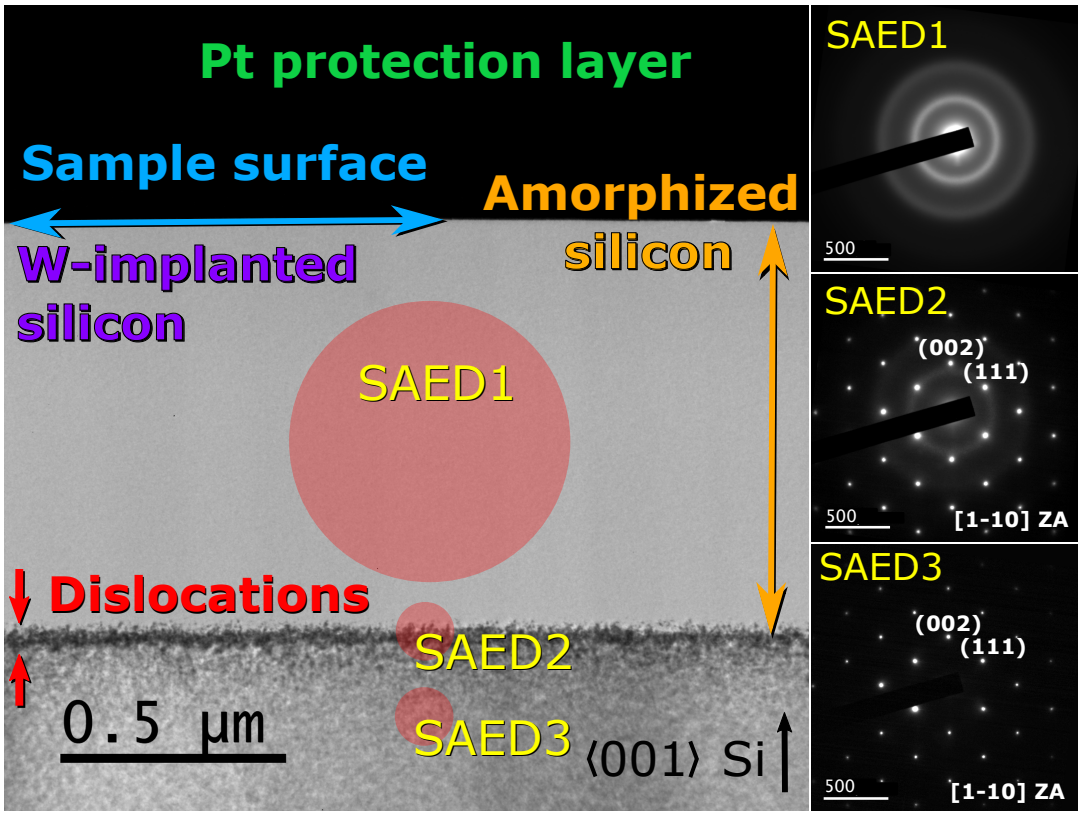

FIGURE 4.2: BF-TEM micrograph of W-D0.1-0P with three selected area electron diffraction patterns. SAED1-3 reveal an amorphous layer, an a/c interface, and a crystalline region, respectively. The red circles schematically illustrate the approximate SAED aperture diameters during ED from the respective areas.

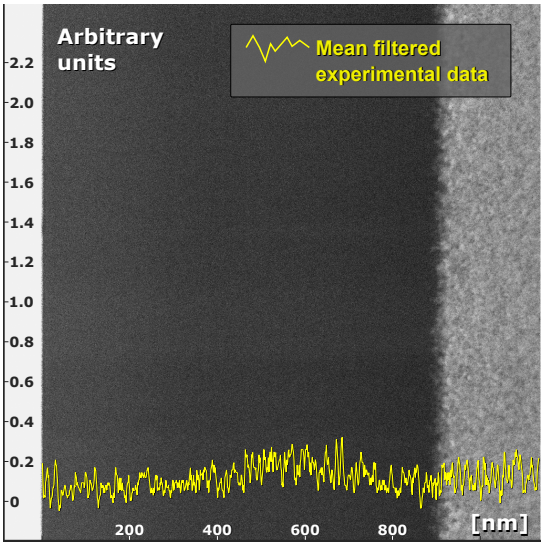

FIGURE 4.3: Mean filtered tungsten distribution profile of W-D0.1-0P, obtained using EDS-mapping. The W profile is plotted on a HAADF-STEM micrograph, corresponding to the area the EDS data was acquired. The profile shows no apparent peak concentrations.

in addition to diffraction spots corresponding to the [1-10] zone axis (ZA) of Si. SAED3 from below this region, shows no extra amorphous rings. This indicates that undamaged crystalline silicon, is underneath/beside the amorphized Si. The dark characteristic region therefore defines a transition/interface between the amorphous W-implanted silicon layer, and the crystalline Si.

The dark feature seen on the amorphous/crystalline (a/c) interface, indicates a presence various crystal defects such as dislocations and possible present interstitial atoms (see Section 2.2.1). The area is measured to be approximately (0.05 ± 0.01) µm deep, and defines the end-of-range (EOR) region. Acquired and mean filtered EDS spectra is shown in Figure 4.3, plotted on a corresponding HAADF-micrograph. The spectra supports the possible presence of interstitial W atoms. This indicates that there may be an excess W population in the crystalline Si, as a result of the ion implantation.

Due to the noisy EDS data (despite mean filtering), no apparent peak concentration can be determined from the data set. A small increment close to 0.6 µm underneath the sample surface is observed, but may be due to noise. Therefore, neither the presence nor the W interstitial concentration, can be discussed in detail for the present sample. In addition - during EDS acquisition, the software was not able to automatically select W as a present element, without the influence of the operator. Therefore, the expected peak concentration of tungsten may indicate a detection limit close to 0.1 at.% (see Section 2.2.5). Secondary ion mass spectrometry (SIMS) - a technique used to analyze the composition of solid surfaces and thin films, may therefore be a better alternative to EDS, to determine the W distribution. This work is in progress.

With the Pt protection layer/amorphous interface defining the sample surface, and the a/c interface defining the transition from amorphous silicon to crystalline silicon, the measured mean amorphized depth is approximately (0.90 ± 0.02) µm.

4.1.2 W-D0.1-F0.9-1P

Annealing an area of the W-D0.1-0P bulk sample with a laser fluence of $0.9\,\mathrm{J\,cm^{-2}}$, does not melt the entire amorphous volume. A cross-section BF-TEM sample can be seen in Figure 4.4, revealing a different topology and

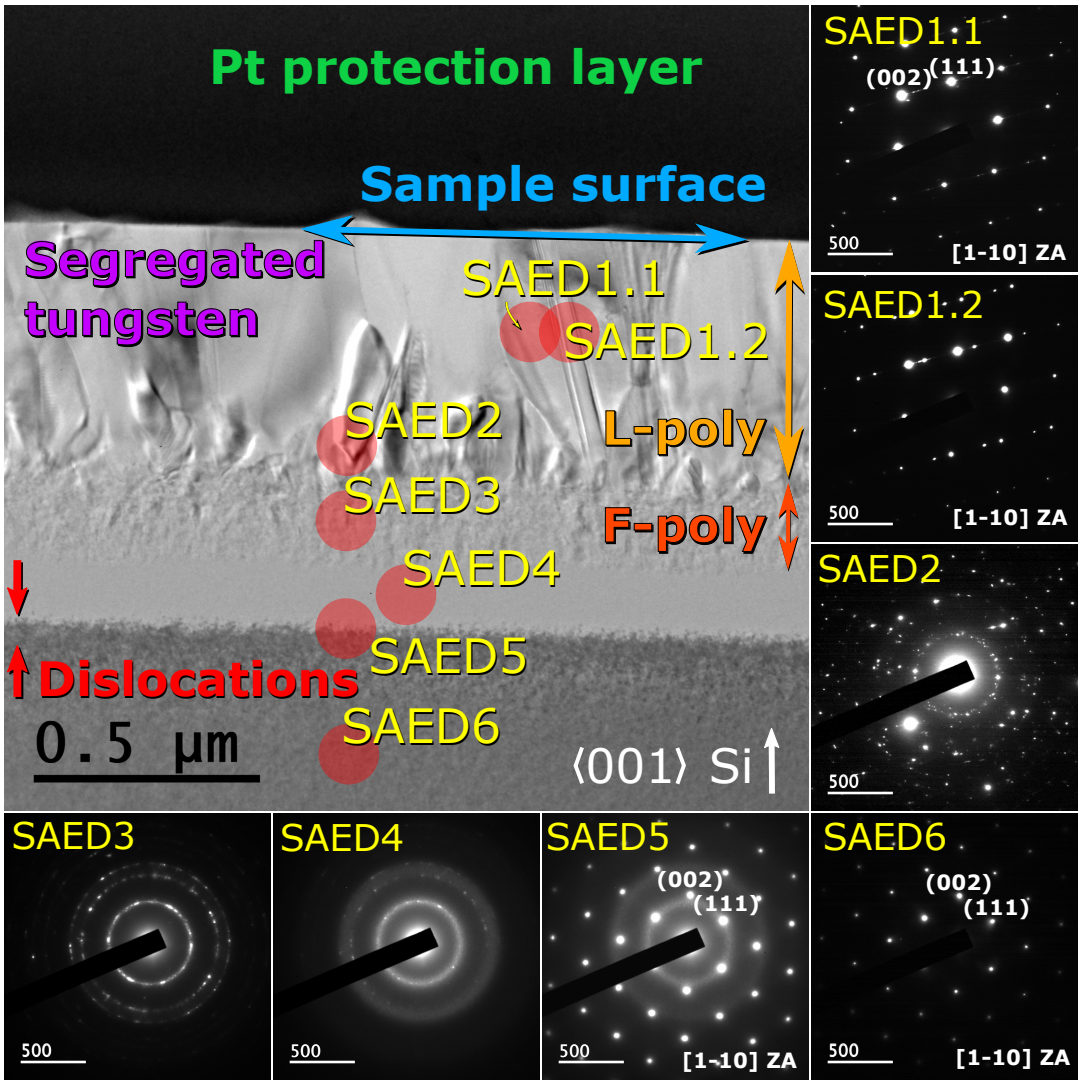

FIGURE 4.4: BF-TEM micrograph of W-D0.1-F0.9-1P with seven SAED patterns. SAED 1.1-1.2 reveal a crystal twinning, while SAED2-6 reveal the DPs of an L-poly region, an F-poly region, an amorphous layer, an a/c interface, and a crystalline region, respectively. The red circles schematically illustrate the approximate diameter and position of the aperture used during ED.

morphology compared to W-D0.1-0P. Surface elevations, crystalline grain boundaries and defects such as crystal twinning (see SAED1.1 and SAED1.2) can be seen, in addition to some characteristic cellular breakdown filaments. SAED2 reveals clear diffraction spots with no apparent symmetry, implying that the layer constituting the sample surface is polycrystalline. SAED3 does also show the characteristics of a polycrystalline diffraction pattern, but has well defined rings with d-values corresponding to Si too. The rings resembles that of an amorphous layer, but contains diffuse diffraction spots as well. This indicates that the region consists of polycrystalline grains, but smaller than the grains in the upper polycrystalline layer. As opposed to SAED3, SAED4 shows the characteristic diffuse amorphous rings as seen in W-D0.1-0P in Figure 4.2, in addition to a few weak diffraction spots. SAED5 reveals the crystallinity of the underlying c-Si (see SAED6) and the amorphous region, but no additional reflections similar to the spots seen on SAED4.

The presence of two possible polycrystalline layers with similar, but different electron diffraction patterns, indicate a possible occurrence of explosive crystallization as described in Section 2.2.1. The undercooled melt from conducted PLM, may have caused a phase transition of the underlying amorphous phase, which possibly has been triggered by heat dissipation and released energy from the solidifying melt. Thus, while the solid/liquid front advances towards the surface - growing large polycrystals (L-poly) of dimensions $0.1 - 1$ µm (see Section 2.2.1), explosive crystallization takes place too, but in opposite direction. The electron diffraction from the small/fine polycrystals (F-poly) region, supports this possible phase transition; SAED4 shows a different, but similar DP to amorphous rings (see SAED4 in Figure 4.4 and SAED1 in Figure 4.2), and polycrystalline ED (see SAED2 in Figure

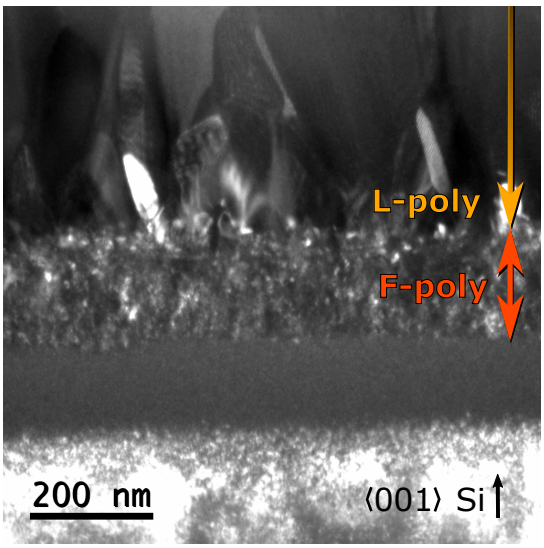

FIGURE 4.5: BF-TEM micrograph of W-D0.1-F0.9-1P. The L-poly/F-poly transition/interface becomes easier to detect, when constructing a micrograph using the second smallest objective aperture, and moving the center of the electron beam away from the area of interest. The result is perhaps a combination between BF- and DF-TEM.

4.4). This becomes more evident, when an amorphous region is seen underneath the F-poly region, revealed by SAED4.

SAED4 shows the characteristic rings of an amorphous phase, but has nonetheless some small diffraction spots in the rings. This may indicate a presence of small crystalline grains in this region. However, the additional reflections may also be due to the aperture size, overlapping with the F-poly region during ED.

It is apparent from Figure 4.4, that the transition from the F-poly to the L-poly region is not evident. However, by moving the electron beam during BF such that a low intensity beam is inflicted onto the sample (perhaps resulting in a combination of BF and DF TEM), the transition becomes more apparent. This can be seen in Figure 4.5. The L-poly and the F-poly regions are thus measured to be approximately (0.56 ± 0.01) µm and (0.17 ± 0.01) µm, respectively. The remaining amorphous region is approximately (0.15 ± 0.01) µm deep.

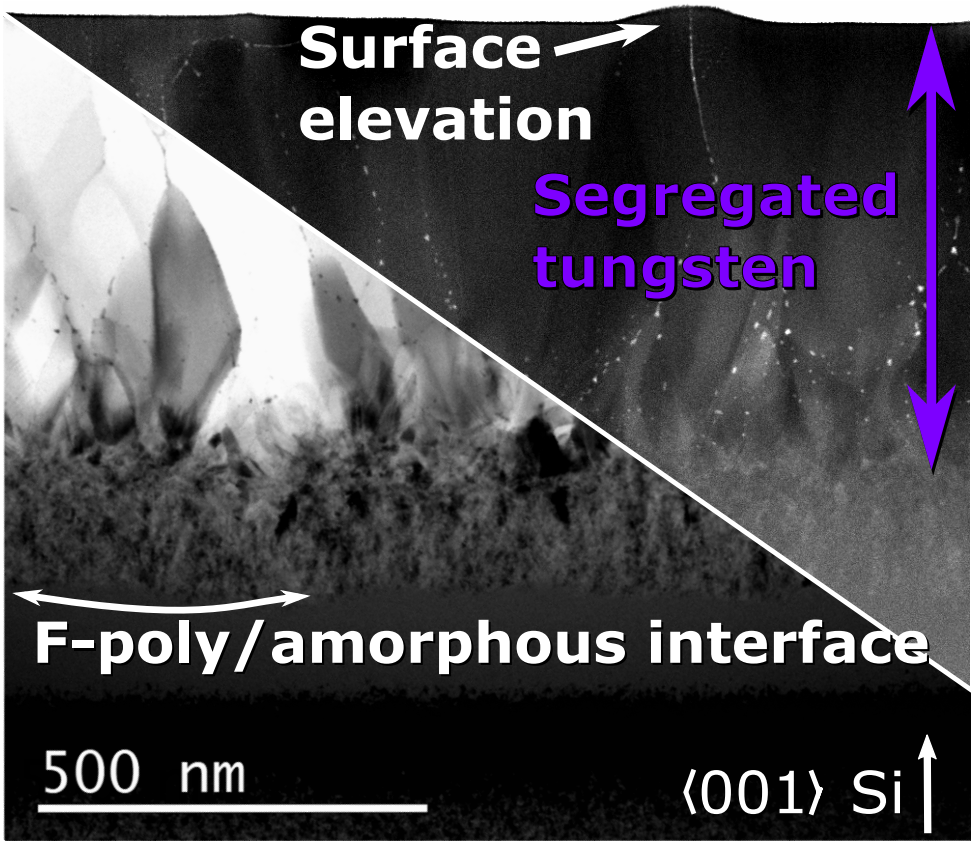

FIGURE 4.6: BF-STEM and HAADF-STEM micrograph of W-D0.1-F0.9-1P, revealing evident W-rich precipitates. Only BF-STEM (and the technique used to acquired the micrograph shown in Figure 4.5) reveal an evident F-poly/amorphous interface. The c-Si is almost completely black after intensity adjustments.

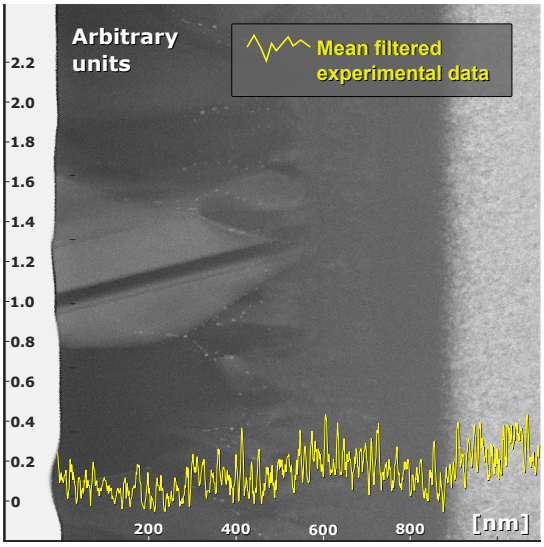

FIGURE 4.7: Mean filtered tungsten distribution profile of W-D0.1-F0.9-1P, obtained with EDS-mapping. The W profile is plotted on a rotated HAADF-STEM micrograph, corresponding to the area the EDS data was acquired. The W profile does not show any apparent peak concentrations, probably due to the EDS detection limit.

Figure 4.6 shows a BF- and HAADF-STEM micrograph, from approximately the same area as Figure 4.4. The micrographs reveal segregated tungsten, but mainly in the L-poly region. It can be seen that W_xSi_y precipitates of dimensions $3 - 28$ nm are present from the Z-contrast, and that the precipitates are not equally distributed in the cross-section sample. Impurity rich threads/filaments stretching from the sample surface are also observed, forming a few complex structures. The small single cluster-shaped precipitates seem to form discontinuous impurity-rich columns. Some of these precipitates can be observed following grain boundaries, while others are not. Whether the discontinuous columns are due to a pinch-off mechanism as described in Section 2.1.2, is not evident from the present sample. However, several of the precipitates can be argued to be discontinuous filaments, regarding their apparent distribution in the micrographs. Due to the difficulty to distinguish W-rich precipitates from possible crystal grains in the F-poly region, an approximate depth containing segregated W will not be given.

The F-poly region appears as a rough unstructured layer underneath the L-poly region, as seen in Figure 4.6. Mainly the BF-STEM micrograph reveals an evident F-poly/amorphous interface, of invariant shape. Segregation of tungsten is not as evident in this region, as it is in the L-poly region. This does also support the possible occurrence of an explosive crystallization.

A W concentration profile from EDS-mapping, is shown in Figure 4.7 on a corresponding HAADF-micrograph. The profile does not show any apparent peaks, except small concentration increases at approximately 0.6 µm below the sample surface, and in the c-Si region. However, because of the low W concentration in the present sample, the possibility that this is statistical interference, is not unlikely.

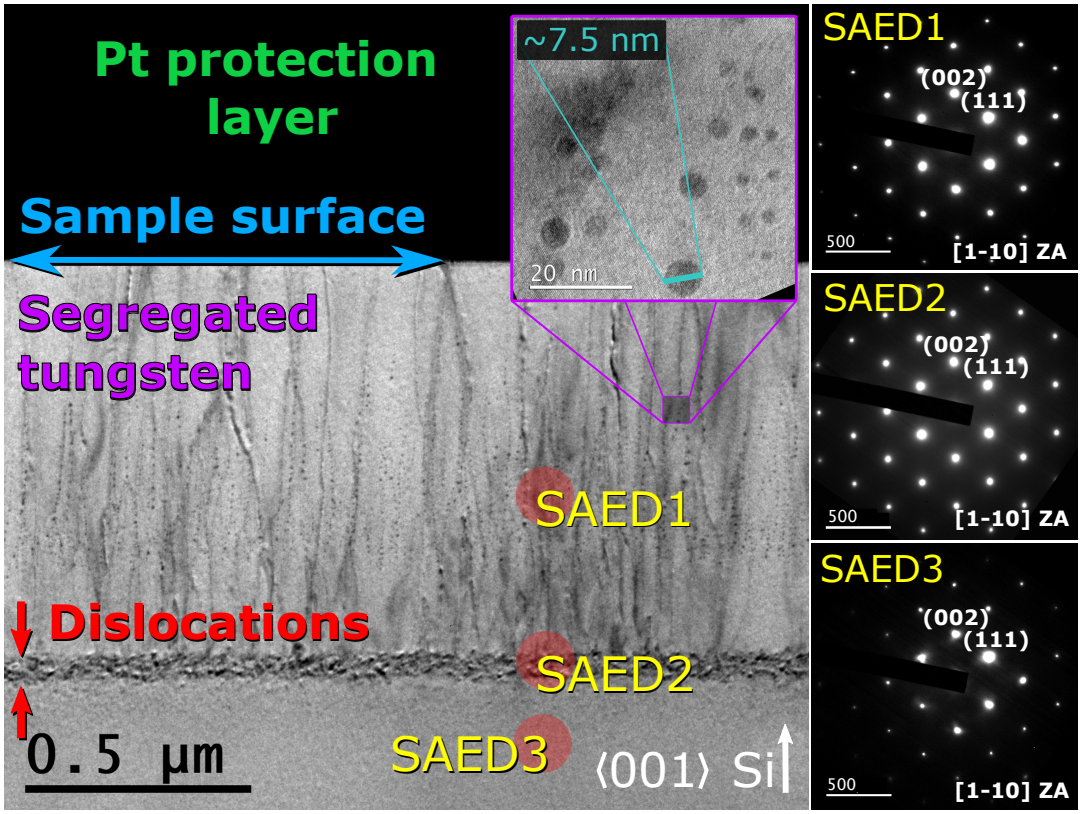

FIGURE 4.8: BF-TEM micrograph of W-D0.1-F1.8-1P, where segregated W-rich precipitates can be seen. Three corresponding SAED patterns are included, showing the projected [1-10] ZA. This indicates that epitaxial crystal growth has occurred, during solidification. No apparent super reflexes are observed in the DPs. The red marked areas schematically illustrate the approximate diameter of the aperture used during ED from the respective areas.

4.1.3 W-D0.1-F1.8-1P

Increasing the laser energy fluence to $1.8\,\mathrm{J\,cm^{-2}}$, results in complete recrystallization of the entire amorphized volume as seen in Figure 4.8. The selected area electron diffraction pattern from the recrystallized region (SAED1), reveals that the solidified melt has crystallized into a monocrystalline phase. The phase is identical to the crystalline Si phase, reveal by SAED2 and SAED3.

Mainly $\sim 1-10$ nm-sized precipitates of tungsten and silicon are found in the recrystallized region, which is verified by the HAADF-STEM micrograph in Figure 4.9. However, some precipitates approximately 40 nm are also present, in addition to a few observed filaments > 50 nm. The precipitate morphology looks like discontinuous filaments as seen in W-D0.1-F0.9-1P (see Section 2.1.1), reaching approximately 0.68 ± 0.04 µm underneath the sample surface. However, in contrast to W-D0.1-F0.9-1P, apparent dark features approximately perpendicular to the surface normal, are also present in

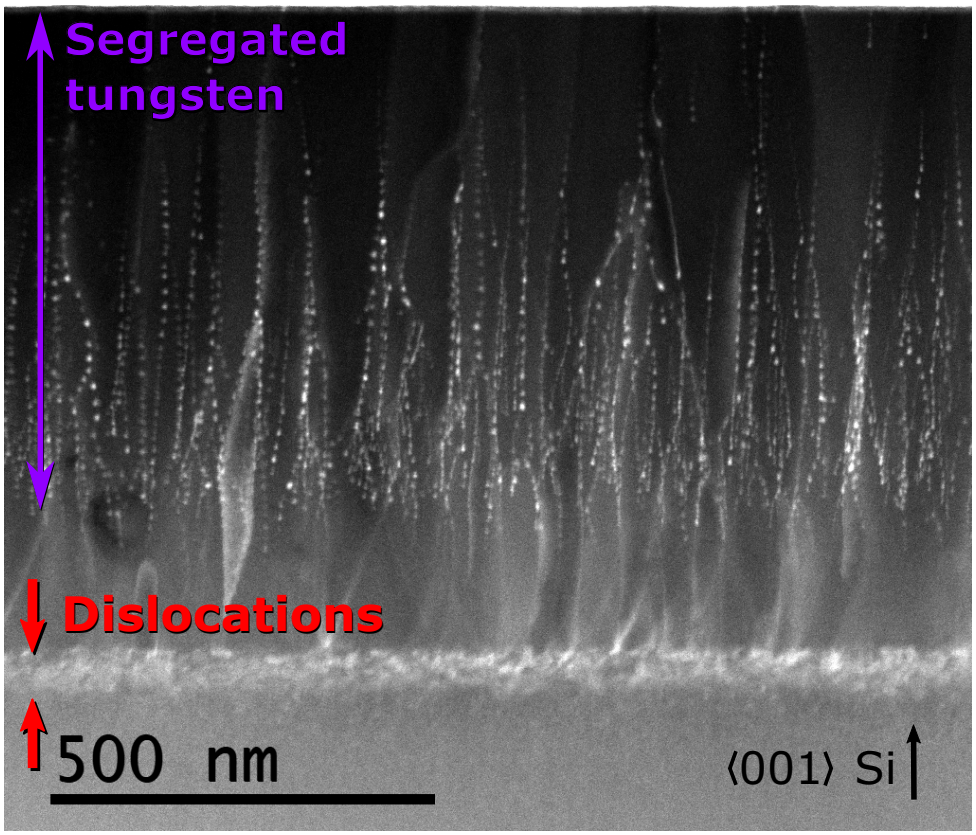

FIGURE 4.9: HAADF-STEM micrograph of W-D0.1-F1.8-1P, revealing segregated W-rich phases in the recrystallized region. Whether the Z contrast seen in the pre-a/c interface, is large W-concentrations or caused by crystal defects, is not evident from the micrograph.

the BF-TEM micrograph. This may either be W-rich silicon phases, or defects such as stacking faults and/or stress. If the latter case, the defects may be a result of tungsten accumulation, large temperature gradients from the laser annealing causing the material to expand differently at different temperatures, and/or a result from the rapid solidification. Some of the W-rich precipitates seem to follow these hypothesized defects, which may support the argument of observable stress.

Dark features parallel to the sample surface, are also present approximately 0.9 µm below the sample surface. This contrast effect may be revealing interstitial-rich phases and dislocations, as described in Section 2.2.1. Present dislocations are revealed by tilting the sample, resulting in contrast differences at different angles. This can be seen seen in Figure 4.10. The region of dislocations are also seen in the HAADF-micrograph in Figure 4.9, but whether the Z-contrast is caused by dislocations or interstitial W atoms, is not evident from the scanning technique. However, it may be both.

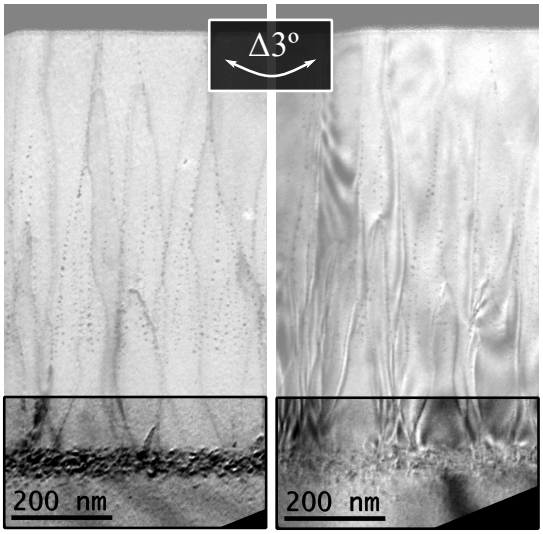

FIGURE 4.10: Defects such as dislocations in the pre- a/c interface, is revealed by rotating the sample. The present sample revealed dislocations by tilting it 3°, as seen in the emphasized areas.

One final interesting observation on the BF-TEM micrograph of W-D0.1-F1.8-1P, is the absence of evident surface morphology. Some surface features can be seen in Figure 4.8, but compared with W-D0.1-F0.9-1P, the elevation is much smaller, and almost flat. The surface morphology can not be determined from TEM alone, and needs to be further studied using scanning electron microscopy (SEM) or atomic force microscopy (AFM) for instance. Nonetheless, this apparent absence may indicate that a small, or perhaps neglectable, destabilization has occurred in the moving liquid/solid interface.

When analyzing diffraction pattern 1-3 in Figure 4.8, it can be observed that all the areas have the same phase. This indicates that the c-Si has acted as a seed during solidification, causing the the melt to grow epitaxially from the substrate to the sample surface. A homogeneous crystal growth may therefore perhaps explain the absence of evident surface morphology. No DP was found with additional reflexes from the observed precipitates, as seen in SAED1. This indicates that the present phases may have a similar arrangement as the surrounding silicon. However, another possible explanation, is that the observed W-rich precipitates are amorphous to some extent. This phase will consequently cause no additional reflections in the diffraction pattern, but weak background noise. This may perhaps be observed in SAED1 and SAED2, but is too weak to tell. In addition, it was further attempted to find a precipitate zone axis by tilting the sample, but without any good results. This may also strengthen the hypothesis of a possible amorphous phase within the Si matrix. This implies that during solidification, the reduction in precipitate interfacial energy by clustering into small and almost circular phases, might be favourable over a W crystallization. Furthermore, if the observed precipitates are amorphous, a lattice mismatch is to be expected

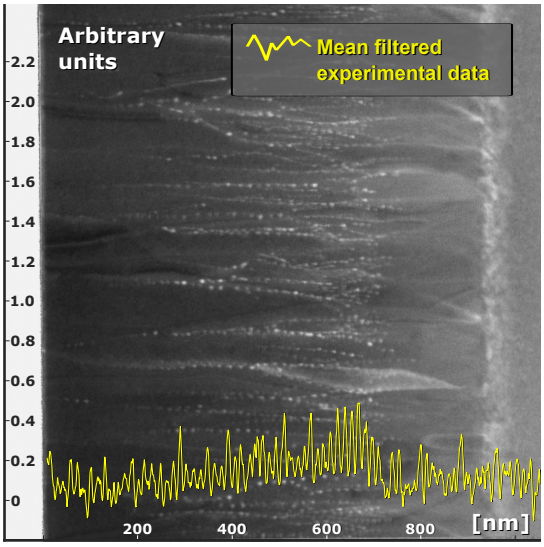

FIGURE 4.11: Mean filtered tungsten distribution profile of W-D0.1-F1.8-1P, obtained with EDS-mapping. The W profile is plotted on a HAADF-STEM micrograph, corresponding to the area the EDS data was acquired.

in the Si matrix. Consequently, strain and other effects in a TEM micrograph is anticipated. Such effects are perhaps observed in Figure 4.8, and is therefore strengthening the possibility that the W-rich precipitates are amorphous to some extent.

The acquired EDS and mean filtered W distribution profile, is shown in Figure 4.11 on a corresponding HAADF-micrograph. The profile shows a rough distribution of tungsten atoms, with a possible peak located approximately 0.6 µm underneath the sample surface. The profile shows a sudden drop close to 0.7 µm, which correlates well with the depth of observed tungsten rich precipitates (see Figure 4.9).

A noticeable Z-contrast is observed in the HAADF-STEM micrograph of W-D0.1-F1.8-1P, where the characterized dislocations are present (see Figure 4.9 and 4.10). EDS-mapping reveals that the EOR region may contain tungsten-rich phases. However, the intensity increase in the HAADF-STEM micrograph, may also be due to defects and noise. In addition, also this sample suffers from noise in the EDS data (see Section 4.1.1), implying that the W concentration in this region can not be determined from EDS and HAADF-STEM results alone; SIMS data of the samples of dosage 0.1, is to be published in a later letter.

4.2 Samples of dosage 1

4.2.1 W-D1-0P

Increasing the tungsten peak concentration to 1 at.%, implies that the W concentration is approximately $5-7$ times higher than the reported solubility

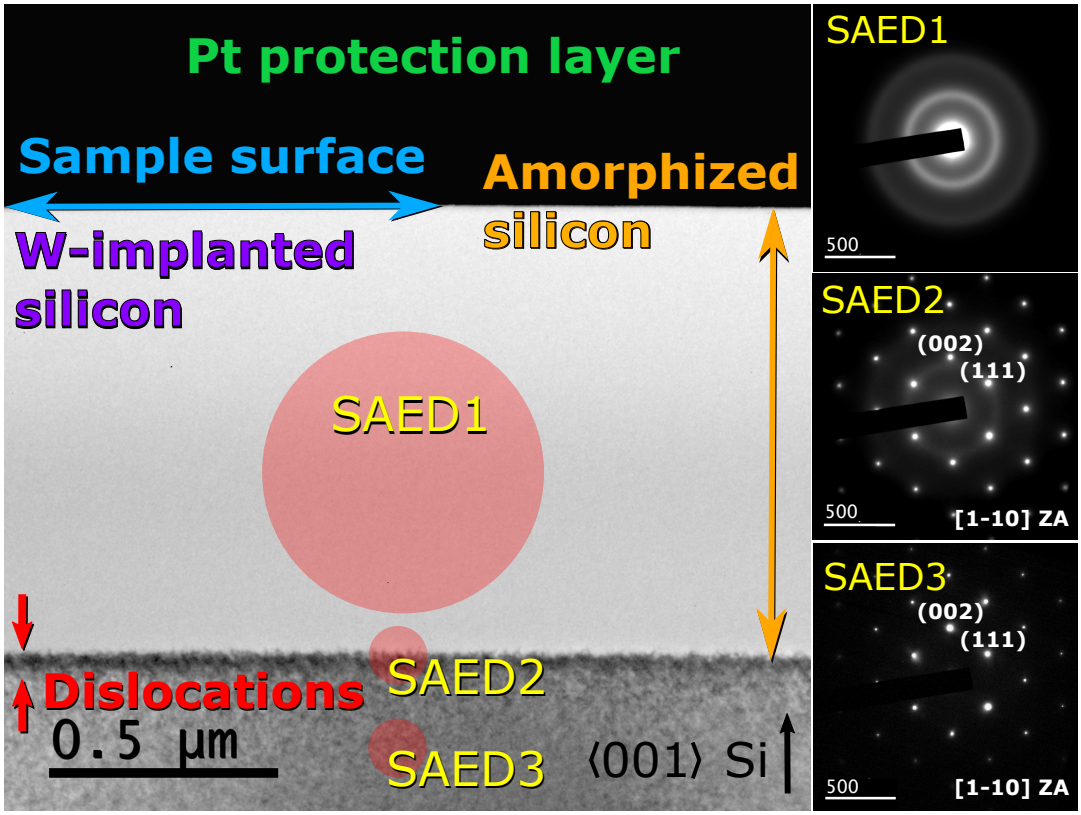

FIGURE 4.12: BF-TEM micrograph of W-D1-0P with three corresponding selected area electron diffraction. The DPs reveal an amorphous area, an a/c interface, and a crystalline region. The red marked circles schematically illustrate the approximate aperture sizes used, during ED in the respective areas.

limit (cf. Section 2.1.1). A BF-TEM micrograph of W-D1-0P can be seen in Figure 4.12, with three corresponding diffraction patterns. SAED1 shows characteristic amorphous rings, which also can be seen in SAED2 to some extent. SAED3 shows the DP of the crystalline Si from the [1-10] ZA, which is the same as the DP in SAED2. The sample thus shows similar features as the as-implanted sample of dosage 0.1. The measured mean amorphized depth is approximately (1.02 ± 0.01) µm, whilst the area of evident dislocations is approximately (0.05 ± 0.01) µm.

Figure 4.13 a) shows an HAADF-STEM micrograph of W-D1-0P acquired on the [1-10] ZA, with an appearing Z-contrast between approximately 0.5 µm and 0.8 µm below the sample surface. The intensity increase was not detected in W-D0.1-0P, implying that the Z contrast becomes difficult to detect (on a ZA) when a W concentration is somewhere between 0.1 and 1 at.%. The mean filtered W distribution acquired using EDS-mapping, is shown in Figure 4.13 b) (yellow graph) on a corresponding HAADF-micrograph. An evident peak concentration is located approximately 0.6 µm underneath the

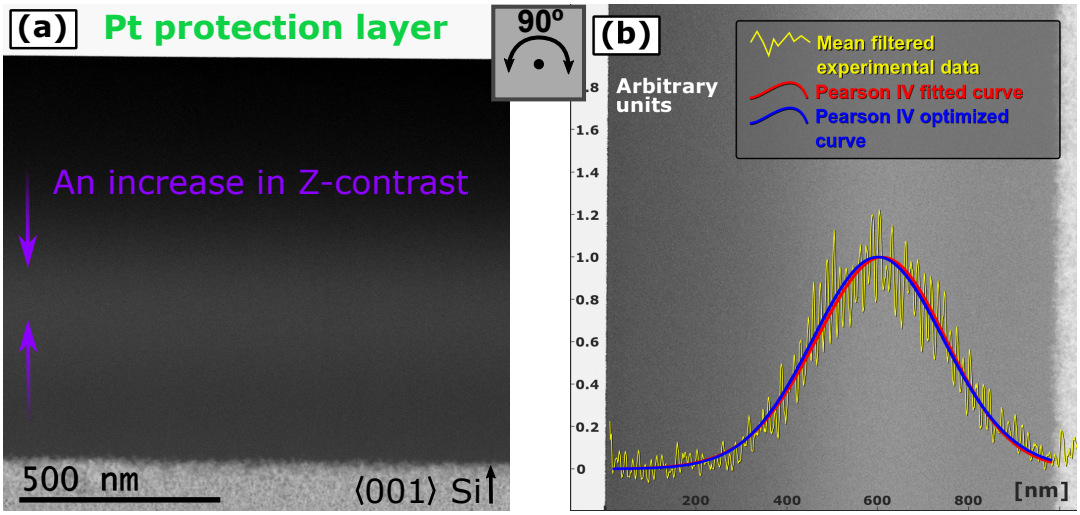

FIGURE 4.13: (a) HAADF-STEM micrograph of W-D1-0P. The purple arrows illustrate intensity gradients from an Z-contrast increase; (b) Mean filtered experimental W distribution profile of W-D1-0P, obtained with EDS mapping (yellow curve). Moments of fitted Pearson IV curve (red): R_p = 0.595 µm; ΔR_p = 0.150 µm; $\gamma = -0.116$; $\beta = 3.166$. Moments of optimized Pearson IV curve (blue): $R_p^{opt.}$ = 0.594 µm; $\Delta R_p^{opt.}$ = 0.152 µm; $\gamma^{opt.} = 0.023$; $\beta^{opt.} = 3.160$. The curves are plotted on a HAADF-STEM micrograph, showing the corresponding area the EDS data is acquired from.

sample surface, implying that the peak is approximately 0.1 µm deeper than the estimated position from TRIM simulations (see Table 3.1). By comparing the position of the W peak concentration in Figure 4.13 b) with the location of the Z-contrast in Figure 4.13 a), it becomes evident that the observed Z-contrast correlates to the increasing W concentration. Lastly, W is also detected in the c-Si region, indicating a presence of W interstitials in the c-Si region.

The W distribution profile from EDS mapping, fits a Pearson IV distribution. The red curve is the experimentally fitted distribution, whilst the blue curve is the optimized distribution. By excluding some of the mean filtered data in the c-Si when curve fitting, the estimated experimental mean square error ($MSE^{exp.}$) of 8.15×10^{-3} became approximately 1.1% smaller. The optimized value ($MSE^{opt.}$) of 7.92×10^{-3}, became approximately 2.8% smaller. The estimated experimental and optimized Pearson moments are given in the Figure caption. Note that none of the curves in Figure 4.13 b) are normalized, but is done in Section 4.2.4.

4.2.2 W-D1-F0.9-1P

A laser fluence of 0.9 J cm^{-2} does not recrystallize the entire amorphized W-Si phase of W-D1-0P, but leads to four different regions as seen in the BF-TEM micrograph in Figure 4.14. Selected area electron diffraction patterns of W-D1-F0.9-1P, acquired from the respective areas (see SAED1-3 (of which SAED2 has d-values corresponding to Si) and SAED5 in Figure 4.14), reveals an L-poly and an F-poly region, a remaining amorphous layer and the underlying c-Si, respectively (see Section 4.1.2). Apparent tungsten-rich precipitates (continuous and discontinuous filaments and single clusters of lengths

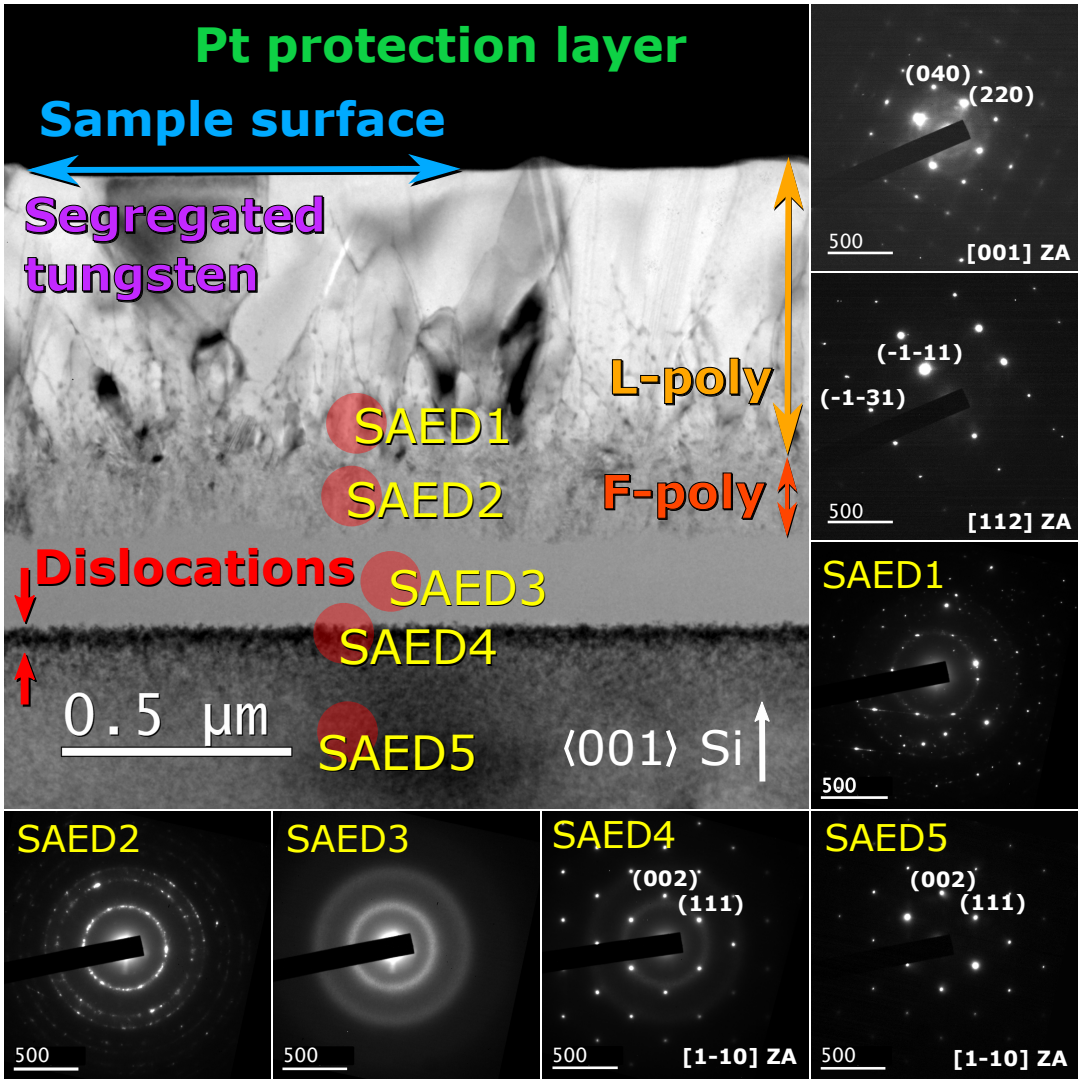

FIGURE 4.14: BF-TEM micrograph of W-D1-F0.9-1P with 7 selected area electron diffraction. SAED1-5 reveal an L-poly region, an F-poly region, an amorphous region, an a/c interface and a crystalline region. The two remaining DPs show a different ZA than the underlying c-Si, and are acquired from another area on the TEM sample. The red marked areas schematically illustrate the approximate aperture sizes used ED, at the respective areas.

$3 - 50$ nm) are observed in the recrystallized region, which is verified by the BF- and HAADF-STEM micrographs in Figure 4.15. An evident interface between the crystallized region and the amorphous layer, is also shown in Figure 4.15.

The presence of threadlike filaments of W_xSi_y phases, are more prominent in the present sample, as opposed to W-D0.1-F0.9-1P. In addition, the present sample contains more cluster-like precipitates, which are not evident discontinuous filaments. It is difficult from both the BF-TEM micrograph in Figure 4.14 and the BF-/HAADF-STEM micrographs in Figure 4.15, to determine whether or not the filaments commence at some interface between the L-poly and the F-poly (see SAED1 and SAED2), or if the formation of these phases are occurring before the hypothesized explosive crystallization takes place. Nonetheless, the observable segregation of threadlike filaments are forming complex structures with respect to each other, where some of them

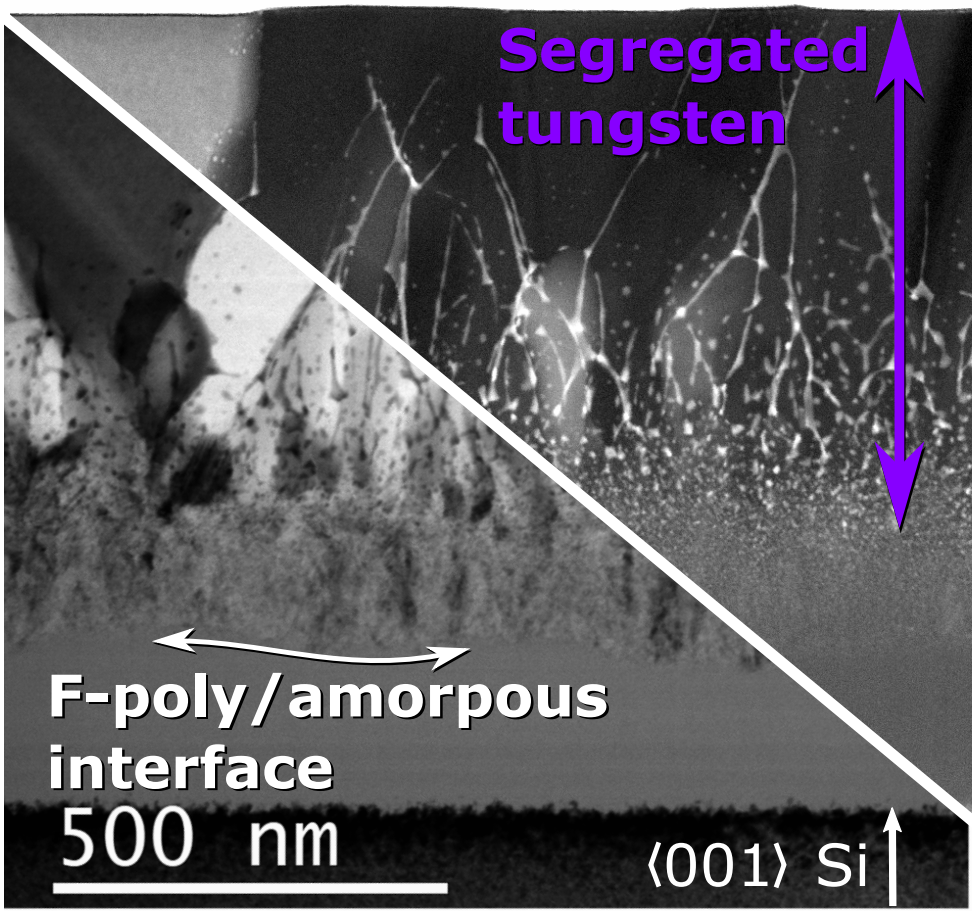

FIGURE 4.15: BF-STEM and HAADF-STEM micrograph of W-D1-F0.9-1P, revealing W-rich precipitates. The BF-STEM micrograph reveal an F-poly/amorphous interface, where a white curved arrow indicates an invariant interface morphology.

follow grain boundaries. Moreover, compared to W-D0.1-F0.9-1P, it is not unlikely that the larger W concentration is affecting the growth conditions of WSi precipitates, regarding the used material processing methods.

An interesting observation on W-D1-F0.9-1P - which can also be seen on W-D0.1-F0.9-1P, is the apparent height variations on the sample surface (there can only be seen small height variations in Figure 4.15, but larger surface morphologies have been observed on the sample; see Figure 4.14). In particular the fact that some of the filaments seem to reach the surface approximately in the middle of a surface elevation. Whether or not this has any correlation with the impurity-rich morphology, can not be determined with the used techniques.

The selected area electron diffraction patterns in Figure 4.14, show similar properties as the micrographs of W-D0.1-F0.9-1P. This implies that the laser fluence has recrystallized a layer of large polycrystals, which is constituting the sample surface (two additional diffraction patterns from two different zone axes are also included in Figure 4.14, but are not acquired from the area shown in Figure 4.14). The L-poly region extends approximately (0.60 ± 0.03) µm deep, from where a transition from the L-poly region to the F-poly region occurs. This transition appears on micrographs using the same technique as the one used to obtain the effects seen in Figure 4.5 (The micrograph is not shown here). The F-poly region is measured to be (0.19 ± 0.01) µm, and may have occurred from explosive crystallization as previously discussed (see Section 2.2.1).

The F-poly layer is positioned between the L-poly region, and the remaining amorphous region which is (0.21 ± 0.02) µm deep. The corresponding SAED3 shows no extra diffraction spots as opposed to W-D0.1-F0.9-1P, which

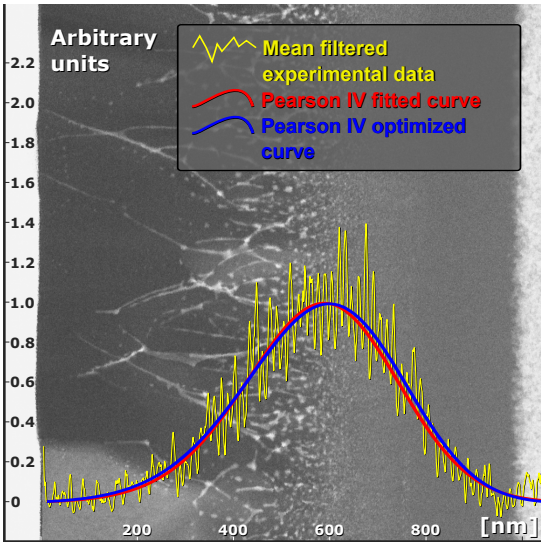

FIGURE 4.16: Mean filtered experimental W distribution profile of W-D1-F0.9-1P, obtained with EDS mapping (yellow curve). Moments of fitted Pearson IV curve (red): $R_p = 0.573\,\mu m$; $\Delta R_p = 0.164\,\mu m$; $\gamma = -0.164$; $\beta = 3.160$. Moments of optimized Pearson IV curve (blue): $R_p^{opt.} = 0.574\,\mu m$; $\Delta R_p^{opt.} = 0.173\,\mu m$; $\gamma^{opt.} = -0.275$; $\beta^{opt.} = 3.161$. The curves are plotted on a HAADF-STEM micrograph, showing the corresponding area of which the data was acquired.

may indicate that the aperture used during ED on W-D0.1-F0.9-1P, covered some of the F-poly region.

The acquired tungsten distribution profile from EDS-mapping (yellow graph), is shown in Figure 4.16 on a corresponding HAADF-micrograph. The peak is located approximately 0.6 µm underneath the sample surface, indicating that W has not diffused remarkably closer to the surface. The profile shape is similar to that of W-D1-0P, which lead to the attempt to fit a Pearson profile to the acquired data. The result is an experimental fitted Pearson IV curve (red), and a corresponding optimized (blue curve) Pearson IV profile. The estimated $\mathrm{MSE}^{exp.} = 1.47 \times 10^{-2}$, whereas $\mathrm{MSE}^{opt.} = 1.38 \times 10^{-2}$. The corresponding moments are given in the figure caption.

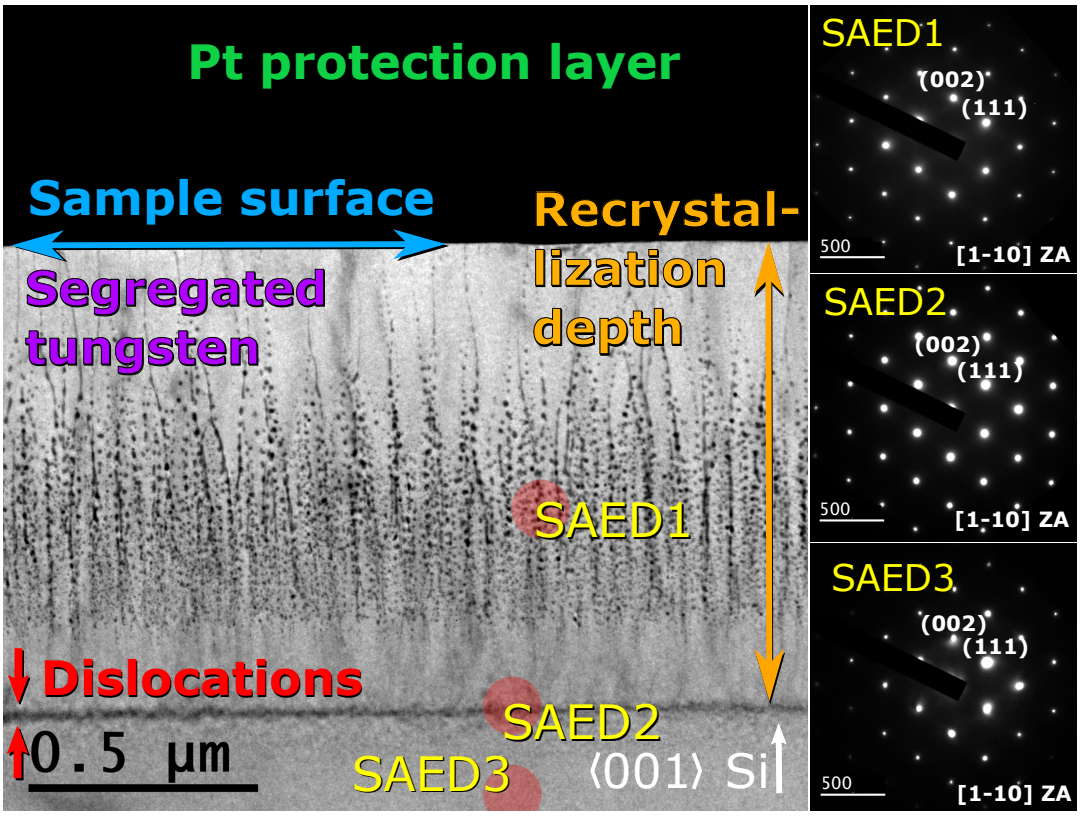

FIGURE 4.17: BF-TEM micrograph of W-D1-F1.8-1P, revealing W segregation into W-rich precipitates. Three corresponding selected area electron diffraction patterns are included, revealing that the crystal growth has happened epitaxially. No additional super reflexes can be seen in the DPs, indicating that W is arranged in the Si lattice. The red marked circles schematically illustrate the approximate aperture sizes used during ED, in the respective areas.

4.2.3 W-D1-F1.8-1P

Increasing the laser fluence to $1.8\,\mathrm{J\,cm^{-2}}$, melts and subsequently recrystallizes the entire amorphized region of the dosage one bulk sample, epitaxially. This can be seen from SAED1 and SAED2, with the BF-TEM micrograph in Figure 4.17. In contrast to the sample with one tenth of the peak concentration, the segregation into discontinuous filaments are more apparent in the present sample, extending from the sample surface to approximately 0.85 ± 0.01 µm below. Dislocations are also present in the current sample.

Despite the fact that the present sample has a W concentration much larger compared to W-D0.1-F1.8-1P, selected area electron diffraction patterns reveal no additional reflections from the tungsten phases. This may indicate that tungsten is perhaps to be found on the silicon lattices, in some arrangement. However, it has also been hypothesized that the observed W-rich precipitates in the previous characterized completely recrystallized sample, may be amorphous to some extent. The same argument can be applied to the present sample, since no additional reflexes are evidently seen. In addition,

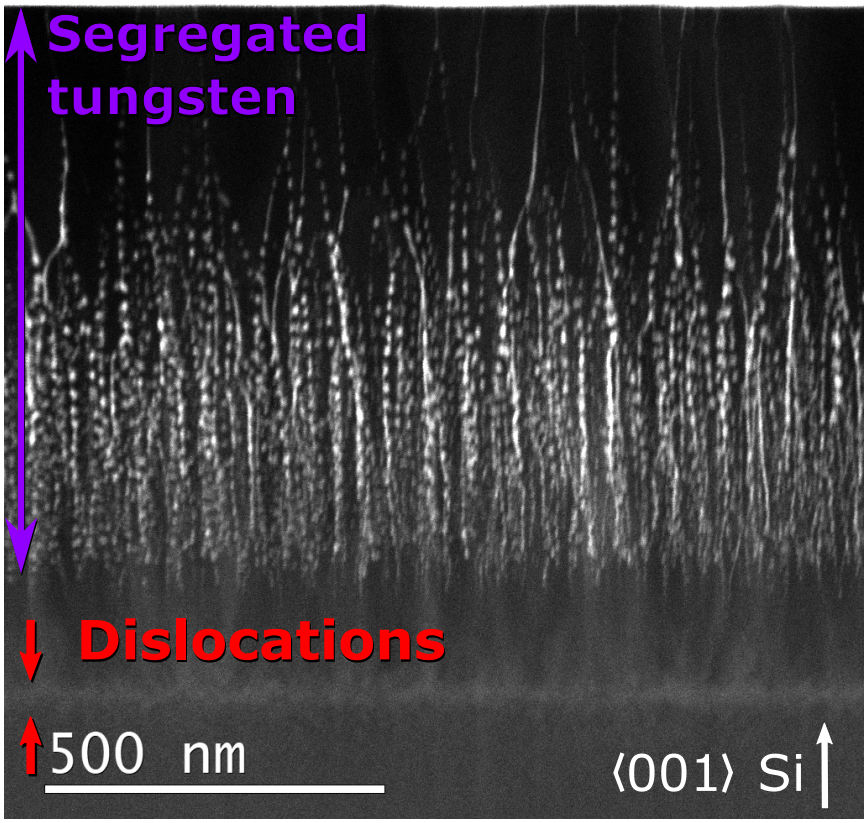

FIGURE 4.18: HAADF-STEM micrograph of W-D1-F1.8-1P, revealing W segregation into W-rich precipitates. Whether the Z contrast in the region of dislocations contains large concentrations of W, or is caused by present defects, is not evident from the micrograph.

this may also perhaps indicate that tungsten crystallizes slower than the solidification velocity, and/or that an interfacial energy is preferable over W crystallization.

Inspecting the acquired HAADF-STEM micrograph of W-D1-F1.8-1P in Figure 4.18, verifies the observed segregated W_xSi_y precipitates of dimension $3 - 50$ nm. The precipitates are visually looking identical to the phases seen in W-D0.1-F1.8-1P, but the present sample reveals mainly discontinuous impurity rich columns. The disconnected morphology is hypothesized to be a consequence of a pinch-off mechanism due to a Rayleigh instability (see Section 2.1.2), which may have been amplified by an impurity bulk diffusion during solidification. The same phenomena may have happened to all the previous characterized recrystallized samples, which contain discontinuous impurity rich filaments. However, yet more continuous filaments can be seen in both W-D0.1-F0.9-1P and W-D1-F0.9-1P. This may be explained by a build up of vacancy-solute pairs around the boundaries in the L-poly region, to reduce Gibbs free energy (see Section 2.2.1).

The acquired experimental and mean filtered W distribution profile from EDS-mapping (yellow graph), is shown in Figure 4.19 on a corresponding HAADF-micrograph. The W peak concentration is located approximately 0.6 µm underneath the samples surface, indicating that W diffusion has not altered the original profile shape at any great extent. The profile therefore resembles that of both W-D1-0P and W-D1-F0.9-1P. A Pearson IV distribution profile was therefore fitted to the profile, as seen in Figure 4.19 (red curve). The corresponding optimized curve is also shown (blue curve), whereas the corresponding estimated moments are given in the figure caption. $\text{MSE}^{exp.} = 1.29 \times 10^{-2}$ whereas the optimized mean square error for the sample is $\text{MSE}^{opt.}$

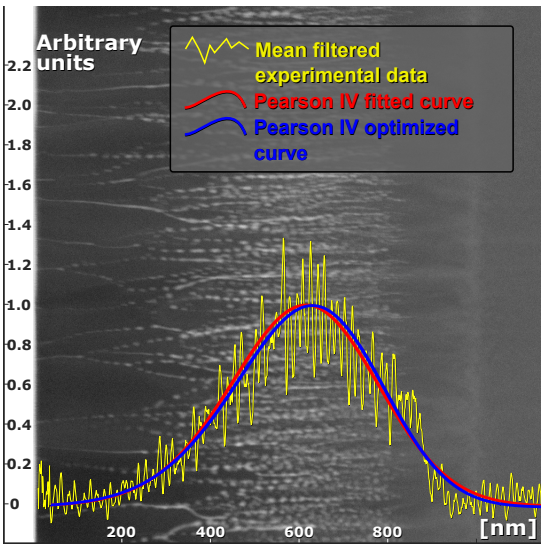

FIGURE 4.19: Mean filtered experimental W distribution profile of W-D1-F0.9-1P, obtained with EDS mapping (yellow curve). Moments of fitted Pearson IV curve (red): $R_p = 0.530\,\mu\text{m}$; $\Delta R_p = 0.160\,\mu\text{m}$; $\gamma = -0.127$; $\beta = 3.190$. Moments of optimized Pearson IV curve (blue): $R_p^{opt.} = 0.531\,\mu\text{m}$; $\Delta R_p^{opt.} = 0.159\,\mu\text{m}$; $\gamma^{opt.} = -0.301$; $\beta^{opt.} = 3.243$. The profiles are plotted on a HAADF-STEM micrograph, showing the corresponding area where the EDS data was acquired.

$= 1.26 \times 10^{-2}$.

4.2.4 Dopant diffusion in dosage 1 samples

Figure 4.20 shows the three optimized distribution profiles of the characterized dosage 1 samples. The profiles have been normalized, and the peak value of W-D1-0P has been set to 1 at.%. The profiles acquired from the recrystallized samples, are calibrated with respect to the peak value of W-D1-0P.

Tungsten has been reported with an unusually slow and still not understood diffusion mechanism (see Section 2.1.1). From Figure 4.20, it can be seen that this does also apply to the present recrystallized samples. With the W distribution profile of W-D1-0P as reference, it can be observed that tungsten diffuses slowly towards the surface during recrystallization, as expected.

The overall tungsten diffusion of W-D1-F0.9-1P, has occurred from approximately 0.7 µm underneath the sample surface: A small deviation from the as-implanted value, is observed approximately in the middle of the F-poly region. This strengthens the argument of energy transfer, from the solidifying L-poly region to the amorphous layer; since W is more soluble in liquid silicon compared to solid Si, W will diffuse into the liquefied Si. This implies that diffusion from the neighbouring F-poly region to the liquid phase, may have occurred during explosive crystallization, before the major liquid/solid interface advances towards the sample surface.

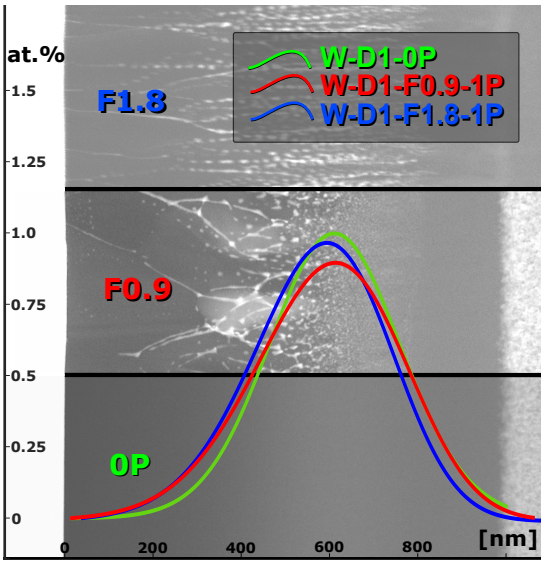

FIGURE 4.20: Normalized optimized tungsten distribution profiles of W-D1-0P (green curve), W-D1-F0.9-1P (red curve), and W-D1-F1.8-1P (blue curve), plotted on corresponding rotated HAADF-micrograps for illustration. The profiles are normalized, and calibrated with respect to the expected peak concentration of the as-implanted sample.

When the undercooled melt commences the phase transition, the W diffusion in the L-poly region seems to be moving parallel with the solidification direction. Compared to the diffusion in the F-poly region, this seems to be happening to a greater extent. This too, supports the hypothesis of an occurred explosive crystallization. However, other experimental methods ought to be done, to verify this observation or not.

It can be seen from Figure 4.20 that W diffusion in W-D1-F1.8-1P has happened in the entire recrystallized volume, with an overall movement towards the surface. This supports the argument that the entire amorphized volume probably has been melted by the laser pulse, causing a more uniform dopant diffusion parallel to the advancing solidifying direction. In addition, an apparent concentration difference between W-D1-F0.9-1P and W-D1-F1.8-1P, can be observed between approximately 0.4 µm and 0.7 µm below the surface. This too supports the possible occurrence of an explosive crystallization in W-D1-F0.9-1P.

Figure 4.20 does only show a W distribution schematics, due to the detection limit of EDS. A more detailed analysis ought therefore to be done with e.g. secondary ion mass spectrometry, to compare with the presented EDS data. SIMS is done to all the presented dosage 1 samples, and will be presented in later work.

4.3 Samples of dosage 2

4.3.1 W-D2-0P

The last as-implanted sample to be characterized in this thesis, is W-D2-0P. The present sample is expected with a W peak concentration of 2 at.%., which is approximately $10 - 13$ times larger than the reported solubility limit (see Section 2.1.1). A BF-TEM micrograph of W-D2-0P, can be seen in Figure 4.21. The as-implanted sample shows similar structural properties as the two previous characterized as-implanted samples, with an amorphous layer (SAED1) located on top of a crystalline layer (SAED3 shows the [1-10] ZA). A damaged interface is seen between these two regions (SAED2), defining the commencing EOR region. The a/c interface contains dislocations, and is measured to be approximately (0.05 ± 0.01) µm deep. The implantation depth is approximately (1.02 ± 0.01) µm.

An acquired HAADF-STEM micrograph of W-D2-0P is shown in Figure 4.22 a), revealing an area of increasing Z-contrast between 0.45 µm and

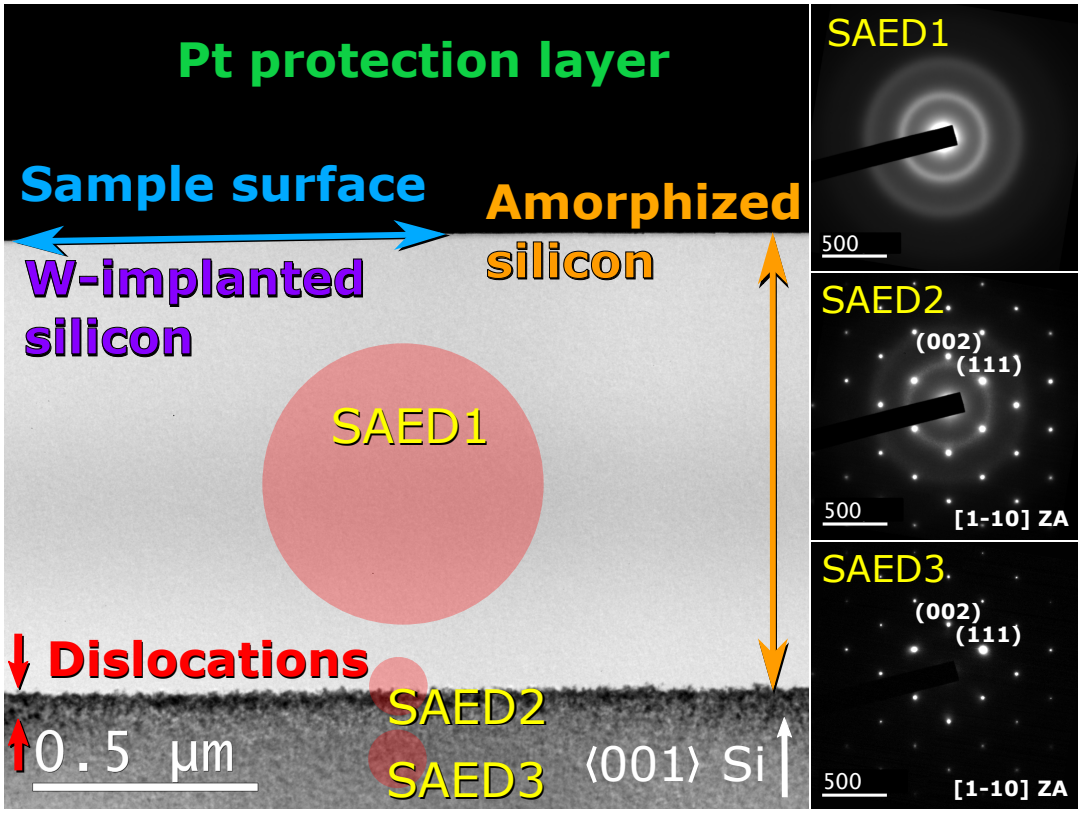

FIGURE 4.21: BF-TEM micrograph of W-D2-0P with three selected area electron diffraction patterns. The DPs reveal an amorphous layer, an a/c interface and a crystalline region. The red marked circles schematically illustrate the approximate aperture sizes, used during ED in the respective areas.

0.80 µm below the sample surface. The mean filtered tungsten distribution profile (yellow graph) in Figure 4.22 b) (plotted on a corresponding HAADF-micrograph), shows that the W peak concentration is located approximately 0.6 µm underneath the sample surface. This implies that the observed Z contrast in Figure 4.22 a), correlates well with EDS data. Tungsten is also detected in the c-Si region, indicating that W interstitials are present in the c-Si. This concerns all the as-implanted samples, which strengthens the hypothesis of W interstitials in this region in all the characterized as-implanted samples.

A Pearson IV distribution function is fitted (red curve) to the acquired EDS data (yellow graph), with a corresponding optimized distribution (blue curve). The graphs can be seen in Figure 4.22 b), where $\mathrm{MSE}^{exp.} = 1.01 \times 10^{-2}$ and $\mathrm{MSE}^{opt.} = 9.19 \times 10^{-3}$. The corresponding estimated moments are given in the Figure caption. Note that the distribution profiles are not normalized in Figure 4.22 b), but will be done in Section 4.3.4.

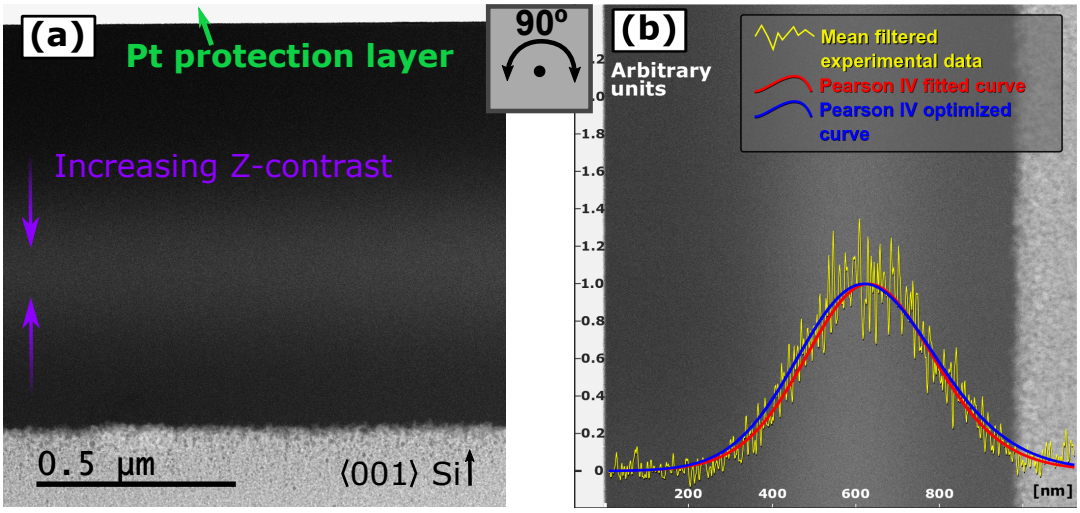

FIGURE 4.22: (a) HAADF-STEM micrograph of W-D2-0P. The purple arrows illustrate intensity gradients from an Z-contrast increase; (b) Mean filtered experimental W distribution profile of W-D2-0P, obtained with EDS mapping (yellow curve). Moments of fitted Pearson IV curve (red): R_p = 0.597 µm; ΔR_p = 0.157 µm; γ = 0.132; β = 3.477. Moments of optimized Pearson IV curve (blue): $R_p^{opt.}$ = 0.595 µm; $\Delta R_p^{opt.}$ = 0.167 µm; $\gamma^{opt.}$ = −0.250; $\beta^{opt.}$ = 3.414. The graphs are plotted on the corresponding HAADF-STEM micrograph, showing the area where the EDS data was acquired.

4.3.2 W-D2-F0.9-1P

Using a laser energy fluence of 0.9 J cm^{-2} on the dosage 2 bulk sample, leads to a partially recrystallization of the amorphized volume. A BF-TEM micrograph is shown in Figure 4.23, and shows similar characteristics as W-D0.1-F0.9-1P and W-D1-F0.9-1P; the crystallization has resulted in four distinct regions: a polycrystalline layer of large grains containing segregate W-Si phases (verified by SAED1), and is constituting the sample surface of invariant topology. The L-poly layer is approximately (0.58 ± 0.02) µm deep. A fine polycrystalline layer is found underneath the L-poly layer (see SAED2, which has d-values corresponding to Si), and is approximately (0.20 ± 0.01) µm deep. This depth has been measured from a micrograph using the same technique as used to obtain the effects seen in Figure 4.5. The third layer is the remaining amorphous material (SAED3) of (0.24 ± 0.02) µm depth, which is lying on top the c-Si (SAED5). SAED3 shows no additional diffraction spots in the amorphous rings, implying that the additional spots seen in Figure 4.4 may have come from the F-poly region.

The measured depth of the polycrystalline layers in all the samples are almost identical, implying that W concentrations in the range (0.1 − 2) at.%

may not affect the amount of melted volume to a great extent. Small differences are nonetheless found, but due to the invariant surface topology of the recrystallized samples, and not completely evident L-poly/F-poly interface, precise depth measurements are difficult from TEM micrographs. Furthermore, the number of samples studied in this thesis, is not large enough to determine if there is a correlation between L-poly depth, F-poly depth and W-concentration in Si. An overview of these measurements will be given in Table 4.1.

It can be seen in the BF-TEM micrograph in Figure 4.23, that continuous

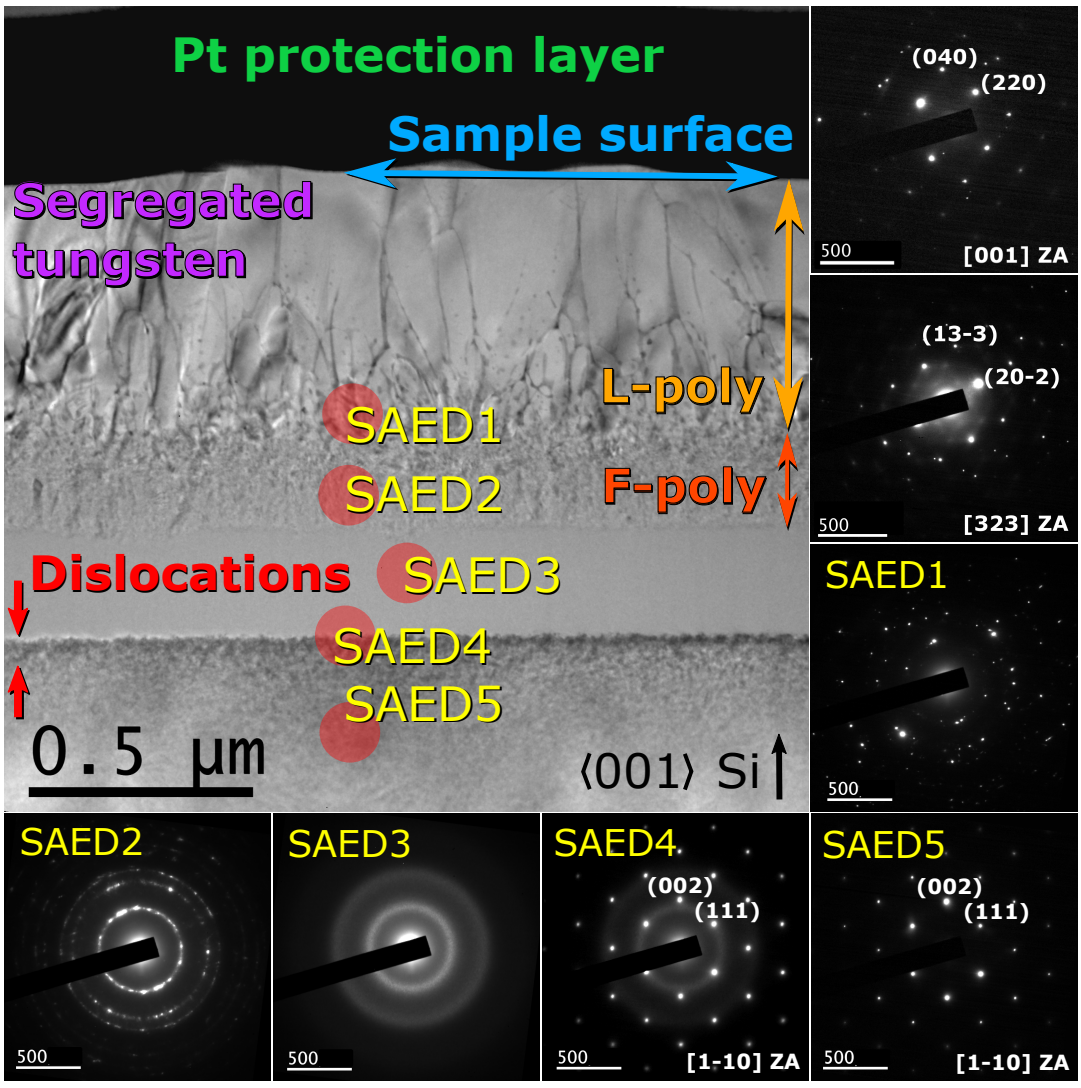

FIGURE 4.23: BF-TEM micrograph of W-D2-F0.9-1P, with five selected area electron diffraction patterns. SAED1-5 reveal an L-poly region, an F-poly region, an amorphous region, an a/c interface and a crystalline region, respectively. The two remaining DPs are showing different ZAs, acquired from another area on the TEM sample. The red circled areas schematically illustrate the approximate aperture sizes used during ED, at the respective areas.

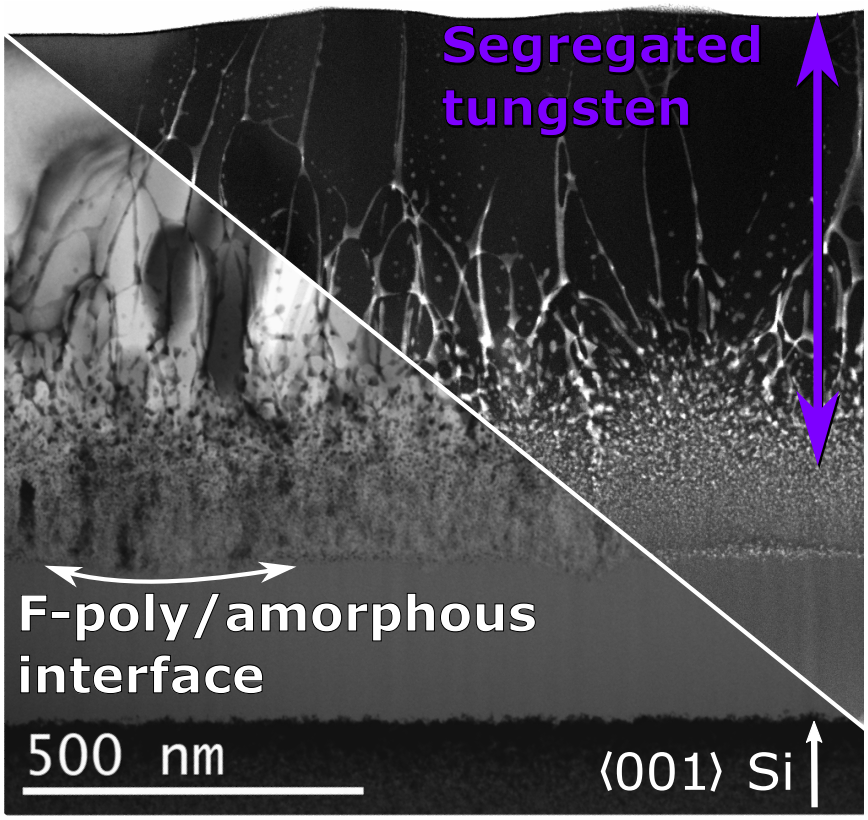

FIGURE 4.24: BF-STEM and HAADF-STEM micrograph of W-D2-F0.9-1P, revealing W segregation into W-rich precipitates.

and discontinuous filaments of WSi phases are present. This is verified by both the HAADF- and BF-STEM micrographs, seen in Figure 4.24. The discontinuous filaments consist of precipitates with dimension $3 - 50$ nm. Filaments are more prominent in the present sample, compared to the two previously characterized samples, recrystallized using a laser fluence of $0.9\,\mathrm{J\,cm^{-2}}$. This may be explained by the larger W concentration in the present sample, regarding the low W solubility limit in solid Si (see Section 2.1.1). Moreover, it seems like more filaments are reaching the sample surface, as opposed to W-D0.1-F0.9-1P and W-D1-F0.9-1P. A possible explanation is the greater W concentration. EDS mapping is not able to verify this hypothesis, implying that other spectroscopy and/or spectrometry techniques need to be conducted. A second possibility may be that impurity rich regions have caused a retarded advancing solidification front (see Section 2.1.2), implying that W segregation has happened for a longer time, and is therefore able to build up columns of W-rich phases until the solidification front has reached the surface (see Section 2.1.2). The latter possibility may also explain the more prominent surface morphology. However, a surface study using e.g. AFM, ought to be done to verify whether or not the topology of the present sample,

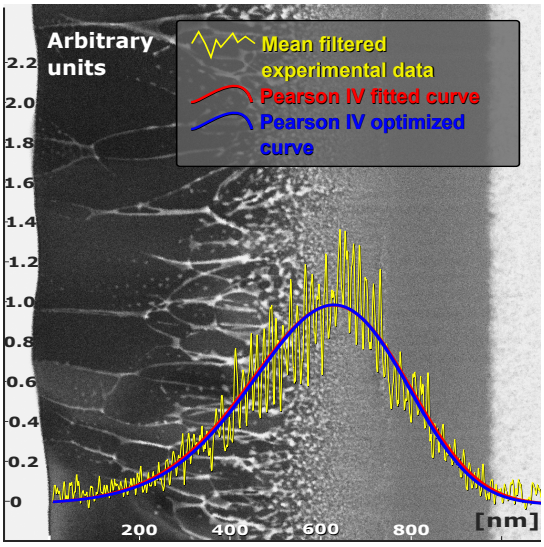

FIGURE 4.25: Mean filtered experimental W distribution profile of W-D2-0P, obtained with EDS mapping (yellow curve). Moments of fitted Pearson IV curve (red): $R_p = 0.562\,\mu m$; $\Delta R_p = 0.173\,\mu m$; $\gamma = -0.372$; $\beta = 3.394$. Moments of optimized Pearson IV curve (blue): $R_p^{opt.} = 0.565\,\mu m$; $\Delta R_p^{opt.} = 0.169\,\mu m$; $\gamma^{opt.} = -0.392$; $\beta^{opt.} = 3.319$. The graphs are plotted on a HAADF-STEM micrograph, showing the corresponding area the EDS data was acquired from.

has a greater roughness compared with the two other samples. A third possible explanation of the greater build-up of filaments close to the surface (compared to W-D0.1-F0.9-1P and W-D1-F0.9-1P), is an increase of point defects between grains: because of the greater W concentration, the introduction of more point defects in grain boundaries may result in a greater reduction in Gibbs free energy (see Section 2.2.1). However, since the conducting crystallization is happening under non-equilibrium conditions, non-equilibrium grain boundary segregation for instance is also a likewise explanation, and participating effect.

The obtained W distribution profile from EDS mapping, is shown in Figure 4.25 (yellow curve) on a corresponding HAADF-STEM micrograph. A Pearson profile was to begin with fitted to the mean filtered EDS profile (red curve), but was only fulfilling the requirement of Equation 2.13. The mean filtering range was therefore changed from 2 to 1, which resulted in the fulfillment of both Equation 2.13 and 2.16. Thus, $MSE^{exp.} = 1.18 \times 10^{-2}$ and $MSE^{opt.} = 1.17 \times 10^{-2}$, whereas the estimated moments are given in the figure caption. The W peak concentration is located approximately 0.6 µm below the sample surface.

4.3.3 W-D2-F1.8-1P

The final sample to be characterized in this thesis, is W-D2-F1.8-1P. A BF-TEM micrograph can be seen in Figure 4.26, from where it can be observed that tungsten has segregated into W-rich precipitates. The segregated phases are mainly discontinuous filament precipitates/clusters of length $3 - 50$ nm, but

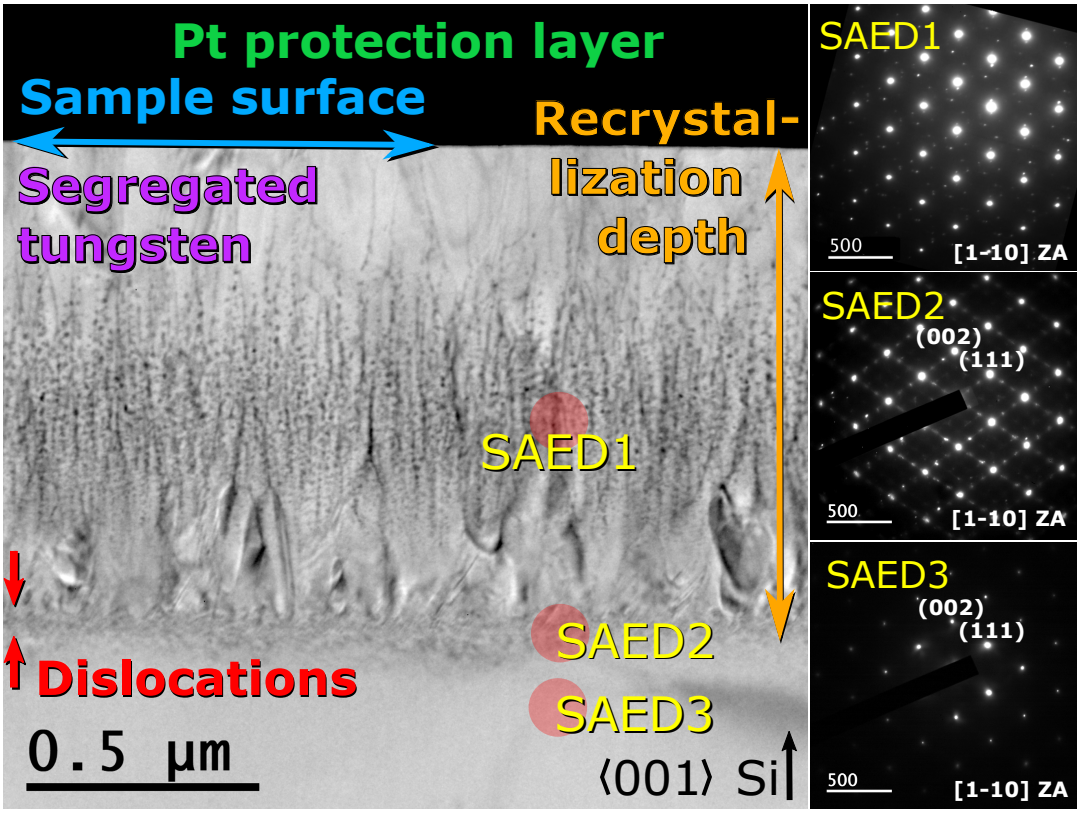

FIGURE 4.26: BF-TEM micrograph of W-D2-F1.8-1P, with three corresponding electron diffraction patterns. The BF micrograph reveal dopant segregation into W-rich precipitates, in addition to other effects and possible defects. SAED1 shows additional reflexes possibly caused by different W arrangements in the silicon lattice planes. SAED2 reveals a more symmetric distribution of super reflexes, where three additional spots can be seen between each Si reflex. This indicates a W arrangement on every third Si {111} lattice plane. The red marked circles schematically illustrate the approximate aperture sizes, used during ED in the respective areas.

continuous filaments are observed too. This can also be seen in the HAADF-STEM micrograph, in Figure 4.27. The segregation of W reaches a depth of approximately 0.93 ± 0.03 µm underneath the sample surface. Electron diffraction patterns show that the large concentration of tungsten, causes multiple scattering event. In SAED1, an apparent asymmetry can be seen in the extra reflections, whilst a more symmetric diffraction pattern is seen in SAED2. However, intense reflections are asymmetric distributed in SAED2 too. SAED1 and SAED2 is characterized as the [1-10] Si ZA (see SAED3), indicating that the crystal growth has occurred epitaxially.

The apparent segregation of tungsten is present in all the recrystallized samples. However, the present sample is the only one that has shown additional reflexes in the corresponding DPs, which are probably caused by the larger concentration of W. Since SAED2 is the only acquired DP with

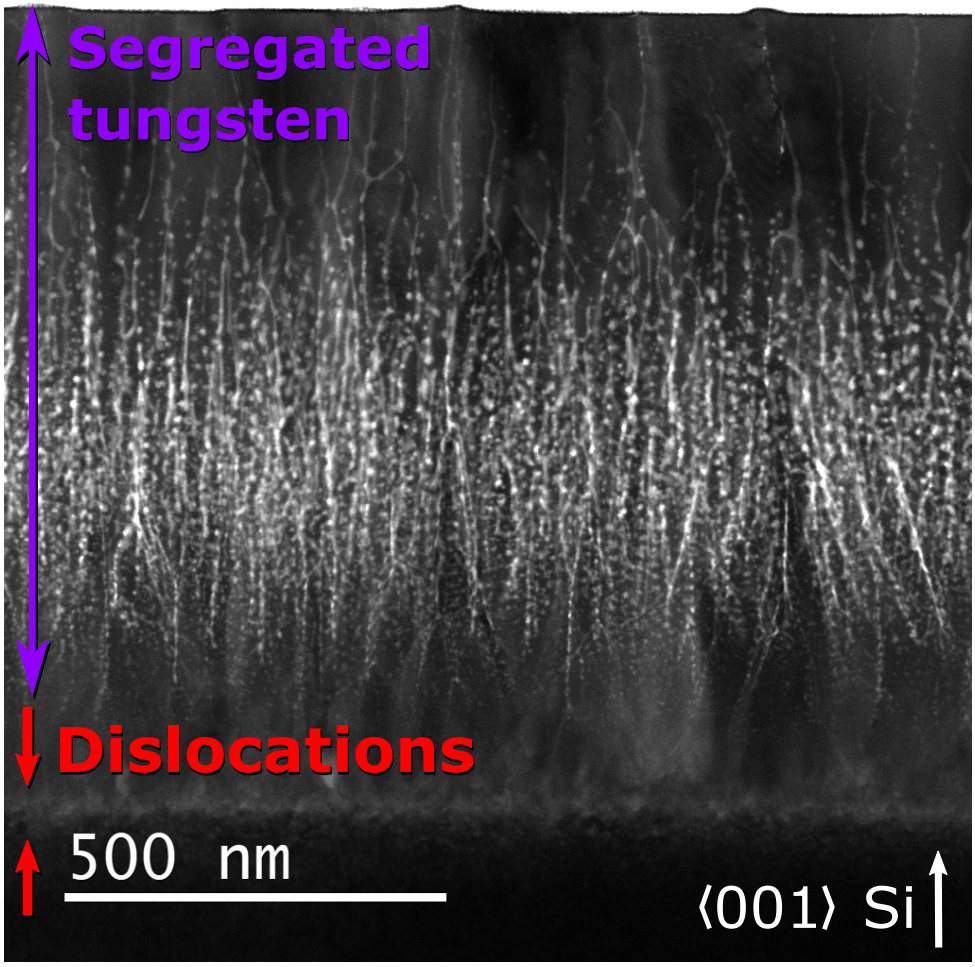

FIGURE 4.27: HAADF-STEM micrograph of W-D2-F1.8-1P, revealing dopant segregation into W-rich precipitates in a complex network. Whether the Z contrast in the pre-a/c interface is caused by W concentrations or defects, is not evident from the micrograph.

some symmetry, SAED2 has been attempted characterized using different approaches. It has been attempted to estimate d-values from the electron DP, and comparing this with d-values of known tungsten silicides and W phases. This has not resulted in any good matches. The DP has also been rotated around the center, while doing a rotational average. An intensity profile has subsequently been plotted with calculated c-W and known W silicide X-ray diffraction peaks (estimated using VESTA; see Appendix A for further details about the tested phases), but without any good matches. Diffraction patterns from tungsten silicide powder, have also been acquired, but with no good fits. The diffraction pattern does therefore not seem to come from any known crystalline W phases, nor tungsten silicide phases. Therefore, another possible explanation is that the present system is not a new phase,

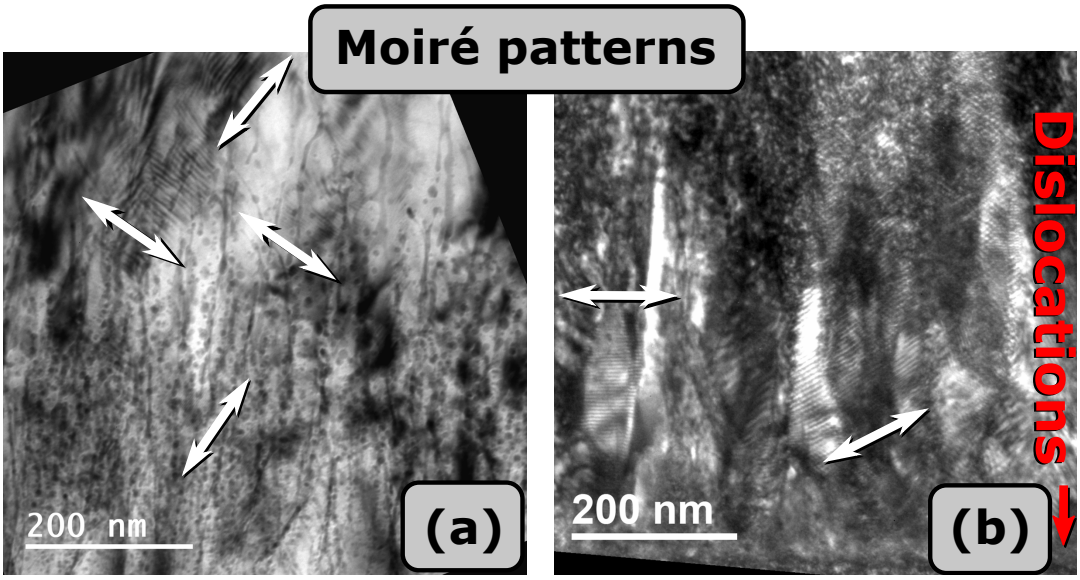

FIGURE 4.28: Moiré patterns revealing the overlap of crystal planes. Different Moiré patterns are orientated differently with respect to each other, indicating that different crystal orientations are present. Figure (a) is taken off zone axis, while (b) is taken on [1-10] ZA. (b) reveals several effects, caused by the sample crystallinity.

but an arrangement of tungsten atoms in the silicon lattice, causing the additional reflexes in the DP. Apparent super reflexes seems to be lying on 1/3 and 2/3 of the {111} reflexes, indicating that W atoms are arranged on every third {111} Si lattice plane. This does not apply to SAED1, where there is much more asymmetry in the DP. However, the W atoms may nonetheless be arranged in a similar fashion in this region.

The electron DP seen in SAED1, was only observed at some regions, in the area of largest W concentration. In other words, the sample's diffraction pattern, alter laterally on the [1-10] Si ZA. This may indicate that W atoms may be arranged in a much more asymmetric and complex way, compared with the hypothesized arrangement seen at the pre-a/c interface.

Figure 4.28 a) and b) show the present sample from off zone axis, and on the [1-10] zone axis respectively. The micrographs are revealing Moiré patterns (and several other effects), which is an overlap of two lattice planes with almost equal lattice spacing. The patterns are oriented differently with respect to each other, which supports the interpretation of a much more asymmetric and complex W arrangement in the area of largest W concentration.

An interesting observation in the present sample (and in the two previous completely recrystallized samples), is the apparent absence of morphological elevations on the sample surfaces. In the recrystallized samples using a fluence of $0.9\,\mathrm{J\,cm^{-2}}$, filamentary precipitates can be seen reaching the

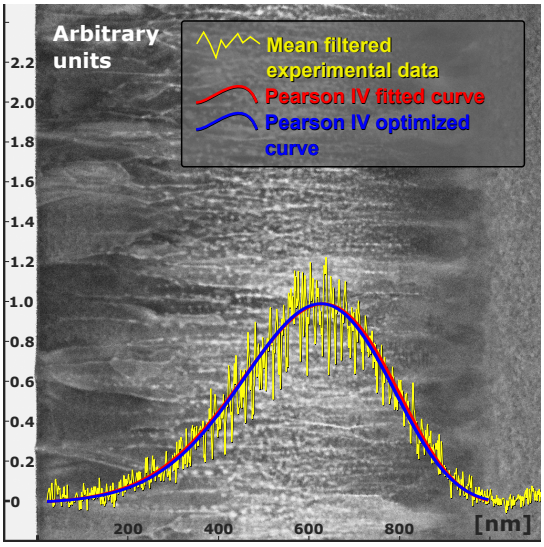

FIGURE 4.29: Experimental W distribution profile of W-D2-0P, obtained with EDS mapping (yellow curve). Moments of fitted Pearson IV curve (red): R_p = 0.547 µm; ΔR_p = 0.159 µm; $\gamma = -0.408$; $\beta = 3.084$. Moments of optimized Pearson IV curve (blue): $R_p^{opt.}$ = 0.549 µm; $\Delta R_p^{opt.}$ = 0.157 µm; $\gamma^{opt.} = -0.387$; $\beta^{opt.} = 3.143$. *beta* does not fulfill Equation 2.7, which might be due to experimental limitations. The graphs are plotted onto a HAADF-STEM micrograph, showing the corresponding area where the EDS data is acquired from.

sample surface. In particular close to where evident surface elevations are present. However, this does not seem to be the case for the completely recrystallized samples, indicating that an approximate homogeneous growth has occurred. Furthermore, W does not seem to cause a great local retardation of the main solidification front, when the solidification occurs epitaxially. However, whether this correlates with growth direction and/or tungsten concentrations, is not clear from the presented results.

The obtained tungsten concentration profile is shown in Figure 4.29 (yellow curve) on a corresponding HAADF-STEM micrograph, with a peak concentration located approximately 0.6 µm below the sample surface. The profile did according to Equation 2.13 correspond to a Pearson IV profile, but Equation 2.16 was not fulfilled. The changing of different parameters was attempted to fulfill Equation 2.16. However, due to the limited range of the data and possibly the present depression close to the a/c interface, β could only be estimated with a deviation of 0.14 from the minimum requirement to use a Pearson IV distribution. β was also set equal to the limiting value of Equation 2.16, but resulted in infinite values in the distribution profile. It was also attempted to fit the distribution to a Pearson I solution (a generalized beta distribution), in case Equation 2.13 was wrongly estimated due to e.g. noise (see Figure 2.15). However, this profile did also result in infinite values. A Pearson IV profile was therefore fitted to the experimental data as seen in Figure 4.29, under the assumption that β would have fulfilled Equation 2.16 if not for the experimental limitations. Figure 4.29 shows the EDS profile (not mean filtered), the fitted (red curve) and the optimized (blue curve) Pearson IV distribution functions. $\text{MSE}^{exp.} = 6.92 \times 10^{-3}$, $\text{MSE}^{opt.} = 6.85 \times 10^{-3}$, and the moments are given in the figure caption.

W interstitials are detected in the c-Si of W-D2-F1.8-1P. This supports the above explanation of SAED2 as well. Nevertheless, the possibility of present metastable W and WSi phases, ought not to be rejected.

4.3.4 Dopant diffusion in dosage 2 samples

The normalized W distribution profiles from the dosage 2 samples, are shown in Figure 4.30. The recrystallized profiles are calibrated with respect to the expected peak concentration of W-D2-0P. The as-implanted W peak concentration is located approximately 0.6 µm underneath the sample surface, which is 0.1 µm further than expected position from TRIM simulations (see Table 3.1).

The optimized W EDS distribution profiles of dosage 2, show similar properties as the profiles of dosage 1 (see Figure 4.20). It can be observed that tungsten has a slow diffusion mechanism in silicon, moving only slightly towards the sample surface during resolidification. An interesting difference however, is the deviation between W-D2-0P and W-D2-F0.9-1P between approximately 0.8 µm and the crystalline silicon. The deviation was not prominent in the dosage one samples, which may indicate that there is an unexpected W concentration difference between the two amorphous regions. However, this deviation may also be caused by noise, due to the different sample preparations: the as-implanted sample of dosage 2 is attached to a TEM Cu-grid as shown in Figure 3.3 F) - G), whilst W-D2-F0.9-1P is attached on one of the finger's sides. Nonetheless, SIMS data is being acquired, and may perhaps verify whether this difference is caused by EDS limitations and noise, or if it is caused by an actual concentration difference.

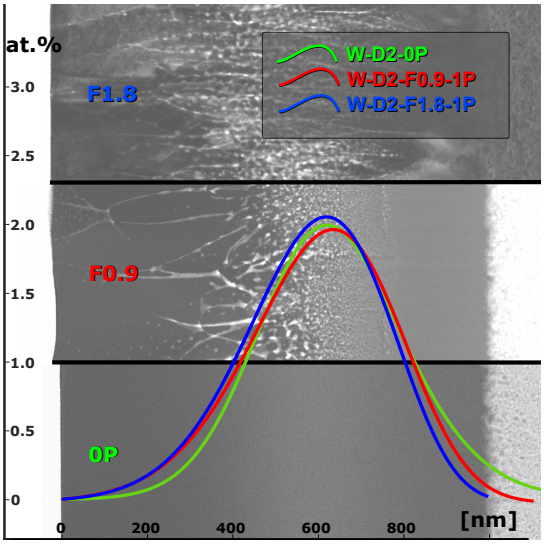

FIGURE 4.30: Normalized optimized tungsten distribution profiles of W-D2-0P (green curve), W-D2-F0.9-1P (red curve) and W-D2-F1.8-1P (blue curve), plotted onto HAADF-STEM micrographs from the respective samples. The profiles are normalized, and calibrated with respect to the expected peak concentration of the as-implanted sample.

When comparing W-D2-F0.9-1P with W-D2-0P at the recrystallized region, it can be observed in Figure 4.30 that a small W diffusion has occurred at approximately 0.7 µm underneath the sample surface. This is approximately in the middle of the F-poly region. This was also observed in the optimized profiles of dosage 1, indicating that W diffusion is perhaps occurring from the F-poly region to the melt during the hypothesized explosive crystallization. It can further be observed that W diffusion has occurred slowly in the L-poly region, from approximately 0.5 µm underneath the sample surface. The diffusion has occurred parallel with the solidification direction, and can be explained by the slow diffusion mechanism of W. A likewise participating effect may also be a possible retardation of the solidification front, which has caused W to diffuse closer to the sample surface (see Section 2.1.2).

From the distribution profile of W-D2-F1.8-1P, it can be seen that an overall diffusion towards the sample surface has occurred during the crystallization - similar to that of W-D2-F0.9-1P in the L-poly region. This supports the argument that the entire amorphous volume has melted. An interesting observation compared to the corresponding profile of dosage 1, is that the W peak is larger than the as-implanted peak. This was not the case for the dosage 1 samples. This may indicate that an accumulation of tungsten around 0.6 µm has occurred during solidification, causing the W concentration to become larger than 2 at.%. W diffusion may therefore have reached an upper diffusion threshold in Si, when recrystallizing using PLM. This may also indicate that W has retarded the solidification front, to such an extent that W has crystallized in some arrangement, and is consequently causing the additional reflexes seen in Figure 4.26. If this is the case, the hypothesis saying that tungsten might be amorphous in (at least) W-D0.1-F1.8-1P, is perhaps strengthened regarding crystallization time. However, the sample of W-D2-F1.8-1P is prepared the same way as W-D2-0P, whilst all the samples of dosage 1 are fastened on the sides of a FIB Cu-grid. This may also perhaps explain the apparent difference between the two dosages. Nevertheless, secondary ion mass spectrometry is being done to the samples, and may perhaps verify this observation or not.

4.4 Recrystallized W-implanted Si

An object of the processed materials, is to incorporate concentrations of W both above and underneath the reported solubility limit in Si. It is further desirable to manage this, without apparent dopant segregation. A second

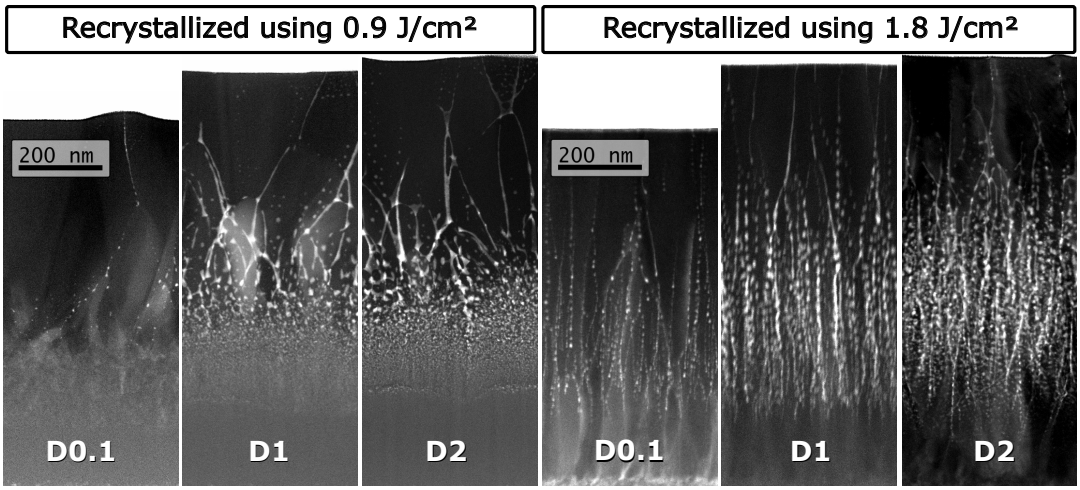

FIGURE 4.31: HAADF-micrographs of all the characterized recrystallized samples of dosage 0.1, 1 and 2, respectively.

object, is to consequently introduce an intermediate band between the silicon valence and conduction band. To accomplish the latter, tungsten needs to be equally distributed within the matrices, as introduced in Chapter 1. In other words, dopant segregation ought not to occur.

Large concentrations of W has been ion implanted in Si matrices, on the expanse of material quality. PLM has therefore been conducted to regain the materials' crystallinity. Since the characterized recrystallized samples show the most interesting properties, the as-implanted samples will not be discussed any further. The characterized recrystallized samples, show segregation of tungsten into WSi precipitates, shaped as continuous and discontinuous filaments as seen in the sample overview in Figure 4.31. This is not desired, regarding solar cell application.

The W rich precipitates in the polycrystalline samples, could not be determined using corresponding diffraction patterns. This implies that high-resolution HAADF-STEM, is perhaps a better alternative to the used techniques. However, morphological similarities can be seen between the observed precipitates, and the WSi phases in the completely recrystallized samples. This implies that the hypothesis from the analysis of W-D0.1-F1.8-1P, W-D1-F1.8-1P and W-D2-F1.8-1P, may perhaps be applied to the polycrystalline samples too.

Differences between the observed precipitates in the polycrystalline samples, are mainly their dimensional sizes. In W-D0.1-F0.9-1P, small cluster-looking precipitates of dimensions $\sim 3 - 30$ nm are mainly observed. These dimensions are given in Table 4.1. The precipitates are arranged in such a way that they remind of discontinuous filaments, implying that most of

TABLE 4.1: Overview over sample characteristics and properties. Used abbreviations are amorphous (a), monocrystalline (c), fine polycrystals (F-poly), large polycrystals (L-poly), continuous filaments (cf) and discontinuous filaments (df). Numbers and/or abbreviations in parenthesis are not as frequently observed characteristics/measurements, but observed/measured to some extent/sometimes. 'Large', 'Small' and 'No' surface topology are defined as surface elevations >20 nm, <20 nm and $\sim$ 0 nm from the lowest point on the sample surface. Note that the W peak concentration applies for the whole polycrystalline sample, and not merely the region on the same line. The term 'Slow' used to describe the diffusion of a particular sample/region, is defined as a graph deviation less than 0.1 µm from the corresponding as-implanted value.

Sample nomenclature	Phase(s)	Depth [µm]	Segregation morphology	Precipitate dimensions [nm]	Surface topology	Diffusion	W peak concentration [µm]	Additional super reflexes
W-D0.1-0P	a	0.90 ± 0.02			No		-[a]	
W-D1-0P	a	1.02 ± 0.01			No		~ 0.6	
W-D2-0P	a	1.02 ± 0.01			No		~ 0.6	
W-D0.1-F0.9-1P	L-poly	0.56 ± 0.01	cf, df	$\sim 3 - 30$	Large	Slow	-[a]	
	F-poly	0.17 ± 0.01				Slow		
	a	0.15 ± 0.01						
W-D1-F0.9-1P	L-poly	0.60 ± 0.03	cf, df	$3 - 50$	Large	Slow	~ 0.6	
	F-poly	0.19 ± 0.01				Slow		
	a	0.21 ± 0.02						
W-D2-F1.8-1P	L-poly	0.58 ± 0.02	cf, df	$3 - 50$	Large	Slow	~ 0.6	
	F-poly	0.20 ± 0.01				Slow		
	a	0.24 ± 0.02						
W-D0.1-F1.8-1P	c	0.68 ± 0.04[b]	df (cf)	$\sim 3 - 10$ (~ 40)	Small	Slow	-[a]	No
W-D1-F1.8-1P	c	0.85 ± 0.01[b]	df (cf)	$\sim 3 - 50$	Small	Slow	~ 0.6	No
W-D2-F1.8-1P	c	0.93 ± 0.03[b]	df (cf)	$\sim 3 - 50$	Small	Slow	~ 0.6	Yes

[a] W peak location could not be determined using energy dispersive spectroscopy
[b] Depth of observed segregation.

the precipitates are not arbitrary distributed within the recrystallized region. The two remaining polycrystalline samples, have a similar morphology to W-D0.1-F0.9-1P. However, these samples contain more continuous filaments in grain boundaries and within the grains, and reveal clusters of length $\sim 3-50$ nm, as seen in Table 4.1. The long clusters are probably disconnected, due to the hypothesized pinch-off mechanism caused by a Rayleigh instability (see Section 2.1.2). This instability, may have been amplified by impurity bulk diffusion, during the solidification (see Section 2.1.2). Moreover, the presence of continuous filaments in grain boundaries, may be explained by a build up of vacancy-solute pairs in the L-poly region. This may be explained by a reduction of Gibbs free energy, which is a characteristic for grain boundaries (see Section 2.2.1). An overview of these results, can be seen in Table 4.1.

It it difficult to separate WSi precipitates from crystal grains, in the F-poly region in the polycrystalline samples. Therefore, no measurements are done to determine the depth of W segregation. In addition, due to the limited number of samples studied in this thesis, no further comments about the small depth differences between the samples' L- and F-poly region, will be made. This can be seen in Table 4.1.

The completely recrystallized W samples grown epitaxially, have a similar morphology as the recrystallized samples using $0.9\,\mathrm{J\,cm^{-2}}$. However, mainly cluster-like precipitates are observed in the samples recrystallized using $1.8\,\mathrm{J\,cm^{-2}}$. W-D0.1-F1.8-1P is observed with precipitates of dimensions $\sim 1-10$ nm, but some clusters as large as ~ 40 nm can be seen too. Filaments are also present (length > 50 nm), but are not observed as frequently as the filaments in the polycrystalline samples. This does also apply for the two remaining completely recrystallized samples, which contains precipitates of size $\sim 3-50$ nm as seen in Table 4.1. The precipitates does not seem to be arbitrary distributed, but resembles discontinuous filaments as seen in the polycrystalline samples.

Neither W-D0.1-F1.8-1P or W-D1-F1.8-1P showed extra super reflexes on the corresponding diffraction patterns, taken from approximately $0.5-0.6$ µm underneath the sample surface. This may indicate that tungsten is positioned in the silicon lattice, in some arrangement. This hypothesis is strengthened from the observed diffraction pattern of W-D2-F1.8-1P (see Table 4.1), where additional reflexes are perhaps indicating that W atoms are arranged on every third {111} Si lattice plane, in the pre-a/c interface. However, the hypothesis does not apply to the region of largest W concentrations, in the

completely recrystallized dosage 2 sample. This is because W atoms are perhaps oriented differently with respect to the Si orientation, or are located in different Si lattice planes in a more complex way. This observation is also supported by the observed Moiré patterns, mainly found in W-D2-F1.8-1P. Whether this hypothesis applies to the two samples of lower W concentrations, is not evident. However, due to the structural similarities between all the completely recrystallized samples, these W arrangement are not improbable.

Different approaches to characterize the present W-rich precipitates, has been attempted during this project. This concerns estimation of d-values from electron diffraction spots, and comparing them with known d-values of crystalline W and W silicides. This approach has not lead to any evident matches. Tungsten silicide powder has also been studied using TEM, with the object of finding electron diffraction patterns similar to the observed DP of W-D2-F1.8-1P. This did not result in any good matches either. Another approach has been to rotate the electron diffraction pattern with extra symmetric reflexes, while doing a rotational average. An intensity profile from the rotated micrograph, was then compared with calculated X-ray diffraction peaks, estimated using VESTA. However, no good fits were found using this method either. Therefore, the structure and phase of the observed precipitates in all the samples, remain unknown; the very same conclusion has been made by [46] (see Section 2.1.1).

It has been hypothesized that W may be amorphous in the W-rich precipitates, to some extent. This does at least concern the completely recrystallized samples of dosage 0.1 and 1, since no additional reflections are observed in the corresponding diffraction patterns. Moreover, this hypothesis can be supported by the fact that no apparent zone axes were found using high-resolution TEM, while tilting the sample. Furthermore, since the precipitates are almost circular-shaped in the completely recrystallized samples of dosage 0.1 and 1, it may also be hypothesized that a surface energy is favourable over a W crystallization energy, during the rapid solidification.

EDS-data shows that recrystallizing a W concentration of 2 at.% in Si, results in an accumulation of W. The accumulation seems to exceed the as-implanted peak concentration. This may have caused a retarded solidification, which consequently may have given W more time to recrystallize (see SAED1-2 of W-D2-F1.8-1P in Figure 4.26). Since an accumulation was not observed in the completely recrystallized dosage 1 sample (and probably not the dosage 0.1 sample too), the explanation of possible amorphous W phases

in the observed precipitates, is strengthened.

Dopant distribution profiles as seen in Section 4.2.4 and 4.3.4, indicate that tungsten inhibit a slow diffusion mechanism. As opposed to the previous project - where silver was ion-implanted in silicon and recrystallized using PLM, the distribution profiles of Ag was observed to move closer to the sample surface (see Section 4.5 for a further comparison of the two materials) [33]. This indicates that tungsten has a slower diffusion velocity, than silver. Therefore, W may perhaps under optimized conditions, show more promising results than Ag - regarding intermediate band materials. However - despite this property, tungsten has diffused laterally, forming W_xSi_y precipitates. This indicates that the W distribution is not homogeneous within the melt, either before or after the phase transition. A second possibility is that the lateral diffusion of W, is happening swifter than the advancing solidification front (see Section 2.2.1).

Despite the efforts to incorporate tungsten in silicon matrices, the slow diffusion mechanism of tungsten may be a promising characteristic. This is if experimental improvements and optimizations, are attempted. An improvement regarding the recrystallization, may be to use a faster laser pulse, which can cause the recrystallization front velocity to surpass the diffusion velocity of W in Si [13, 28, 111]. Another suggestion, may be to recrystallize the W-implanted Si in the solid state, using flash lamp annealing (FLA). A sample is then heated to a temperature close to the melting point for a few milliseconds, which may induce recrystallization in the solid phase. Gao et al. have successfully introduced nitrogen, at a concentration ~ 8 times larger than the equilibrium solid solubility limit in GaAs at 650°C [112]. This implies that FLA might be a better alternative to PLM, to incorporate W in Si. This suggestion is further supported by the slow diffusion of W in Si, especially regarding the results from EDS mapping from F-poly regions.

4.5 Ag- and W-implanted silicon

It was mentioned in Chapter 1, that recrystallized W-implanted silicon is the second project at Norwegian university of science and technology. The objects are to study hyperdoped Si with W and Ag, motivated by the goal of making an intermediate band solar cell material. In the previous project, silicon was ion-implanted with i.a. 1 at.% silver (Ag), and subsequently recrystallized using PLM. However, after TEM characterization, it was concluded that silver had segregated into filamentary structures, and large and

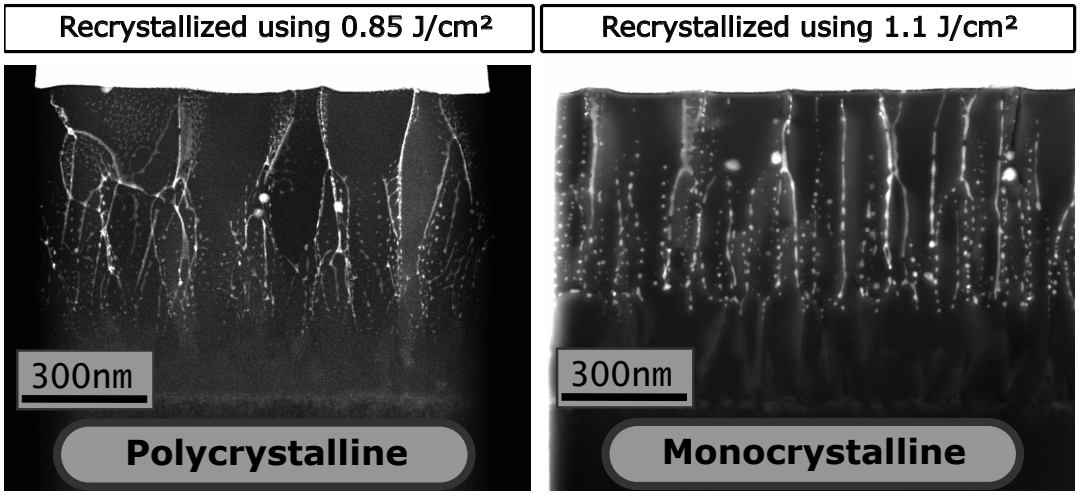

FIGURE 4.32: HAADF-STEM micrographs of recrystallized Ag ion-implanted silicon (amorphized depth of $\sim 0.77\,\mu m$), using a laser fluence of $0.85\,J\,cm^{-2}$ and $1.1\,J\,cm^{-2}$. The Ag peak concentration of the samples' corresponding as-implanted speciment, is 1 at.%. This is the largest concentration of Ag, studied in the previous project. (The HAADF-STEM micrographs are acquired by H. Lysne (see [33] and [34]).)

almost circular silver clusters [33–35]. This can be seen in Figure 4.32, which is showing two recrystallized Ag-doped dosage 1 samples, characterized as polycrystalline and monocrystalline (i.e. the polycrystalline sample has not recrystallized completely, whilst the other sample has grown via liquid-phase epitaxy (see Section 2.2.1)). EDS-mapping of the Ag-implanted samples, show that recrystallizing the samples using one laser pulse, causes the dopant to diffuse towards the sample surface. SIMS shows the very same observation, and is to be presented in a later letter. However, the SIMS data revealed a difference between the two concentration profiles. Therefore, the results from EDS-mapping of the Ag-implanted samples, will not be presented here. However, there is agreement between the two techniques, that Ag diffuses towards the sample surface.

Structural similarities and differences, can be observed between the two different doped materials. It is apparent from Figure 4.32, that both the transition metals segregates and forms phases within the recrystallized Si matrices. Structural differences on the other hand, are more apparent. There are for instance more evident complete filamentary Ag structures in both the Ag samples, which are not as frequently observed in the monocrystalline W-samples. On the contrary, discontinuous filaments are more frequently observed in the completely recrystallized W samples.

The polycrystalline materials of both the W- and Ag-implanted Si samples, are observed with a prominent surface topology. The completely recrystallized samples, does not show a morphology as apparent. However, surface elevations are more frequently observed on the monocrystalline Ag sample, but are almost absent on W-D1-F1.8-1P. Whether this is connected with the smaller implantation depth and laser parameters, can not be said from the present results. However, a correlation between this and the transition metals' diffusive speeds in Si, is not improbable.

An interesting difference between the two different doped recrystallized samples, are the precipitates. Lysne has reported that no traces of Ag silicides, could be observed in the samples. Instead, silver has segregated and formed it's own face centered cubic phase, with orientation relation Ag[011](1-10)‖Si[011](1-10). Neither can be said for the W-implanted Si samples, since W-rich precipitates has been difficult to characterize. Precipitates from the dosage 0.1 and 1 samples, may for instance be amorphous to some extent, but may also be arranged within the Si lattice. Either way, a further study of the observed W precipitates, needs to be done.

"We can then see that if we want to use the electric effects on products in a reaction of two dissolutions with each other, to study this reaction under the influence of light, we must be conscious of the action sunlight can have on the metallic plates used, the effect of which can easily be separated from the total effect, when using the machine filled with two liquids consecutively. I will come back to the distinction between these two effects in a later Memoire"

Alexandre-Edmond Becquerel (1839) [5].

5 Conclusion

In the presented work, tungsten (W) ion-implanted silicon (Si) samples with expected W peak concentrations of 0.1, 1 and 2 at.% (referred to as dosages), have been characterized using transmission electron microscopy (TEM), and energy dispersive spectroscopy (EDS/-X). Corresponding recrystallized samples using pulsed laser melting (PLM) with energy fluences $0.9\,\mathrm{J\,cm^{-2}}$ and $1.8\,\mathrm{J\,cm^{-2}}$, have also been characterized using the same techniques. A Pearson IV distribution profile, has been fitted to all the characterized samples from the dosage 1 and 2 bulk samples.

TEM characterization has shown that all the as-implanted samples, have become amorphous after W ion implantation. The amorphous regions are $\sim 0.9 - 1$ µm deep. High-angle annular dark-field (HAADF) scanning TEM (STEM) micrographs of the dosage 1 and 2 samples, reveal an area of evident Z-contrast in the amorphous region. These areas are located in the area of the detected W peak concentrations, using EDS mapping. Neither HAADF-STEM nor EDS-mapping of W-D0.1-0P, revealed any evident W peak concentrations. This may indicate that 0.1 at.%, is too low for reliable W concentration detection using EDS.

TEM, STEM and electron diffraction (ED) reveal that recrystallizing W-implanted Si samples using $0.9\,\mathrm{J\,cm^{-2}}$ with KrF excimer, does not recrystallize the entire amorphous region. The melted volume recrystallizes into a

polycrystalline phase, whilst heat and energy transfer from the recrystallization are believed to induce explosive crystallization. The result is two polycrystalline layers: one layer consisting of large polycrystal (L-poly) grains constituting the sample surface, and one layer underneath the L-poly layer of fine polycrystal (F-poly) grains. The F-poly grains, are of smaller dimensions than the larger grains. Tungsten is observed segregated in all the recrystallized samples (verified using EDS mapping). The corresponding observed morphologies, are continuous filamentary structures expanding towards the surface, and discontinuous filaments of W_xSi_y precipitates. This indicates that W lateral diffusion velocity, may exceed the recrystallization velocity. Lastly, several filaments follow grain boundaries. This may indicate point defect introductions during solidification, to reduce Gibbs free energy.

TEM, STEM and electron diffraction (ED), reveal that recrystallizing W-implanted Si samples using $1.8\,\mathrm{J\,cm^{-2}}$ with KrF excimer, recrystallizes the entire amorphous region. The underlying crystalline silicon acts as a seed, and is inducing epitaxial crystal growth. W is observed segregated in all the completely recrystallized samples, but mainly into discontinuous W-rich filamentary precipitates (verified using EDS mapping). These formations may have been caused by a pinch-off mechanism, due to a Rayleigh instability. The observed W-rich phases has not been determined, which has also been an issue in other studies. However, the precipitates may not be crystalline W or W silicide phases.

EDS mapping indicate that tungsten inhibit a slow diffusion mechanism, when introduced in silicon matrices. This is expected. An overall movement of the tungsten profiles, are seen in all the recrystallized samples of dosage 1 and 2. The W profiles are relocated in the same direction as the advanced recrystallization front.

Recrystallizing tungsten and silver (Ag) ion-implanted silicon using PLM, results in the segregation of both transition metals. Ag is reported to segregate to complete and discontinuous filaments, of crystalline Ag. The phase's orientation, is equal to the surrounding Si. W segregates into entire and discontinuous filaments too, but mainly into discontinuous filaments when the amorphized volume crystallizes epitaxially. Both the implanted metals diffuses parallel with the direction of the solidification front, but Ag diffuses faster than W.

5.1 Further work

As opposed to the first attempt of making an intermediate band material, Ag was observed with a larger diffusion velocity than W in Si. The transition metal tungsten shows therefore a more prominent diffusion mechanisms. An excimer that can cause larger temperature gradients in doped silicon, may perhaps manage to freeze W in a silicon matrix without dopant segregation. Another technique to consider, is flash lamp annealing (FLA), which has shown promising results regarding impurity incorporation.

The W-rich precipitates has not been determined in the present study, despite different attempts. A further study ought therefore be done, using High resolution (HR) TEM, and/or HR HAADF-STEM for instance.

A

Crystalline tungsten and tungsten silicide phases

A.1 Face and body centered cubic tungsten

The crystal structure presented here, are the crystal structures of which VESTA-estimated X-ray diffraction patterns have been compared with a rotational average intensity profile from the W-implanted silicon sample of largest W concentration.

A.1.1 BCC tungsten

Equilibrium body centered cubic α-W, has a topological close-packed A2 structure (space group $Im\bar{3}m$) [113]. The lattice constant is 4.15 Å [114]. A schematic figure of the crystal structure is shown to the left in Figure A.1.

A.1.2 FCC tungsten

Metastable face centered cubic β-W, has a topological close-packed A15 structure (space group $Pm\bar{3}n$) [113]. The lattice constant is 5.04 Å [115]. A schematic figure of the crystal structure is shown to the right in Figure A.1.

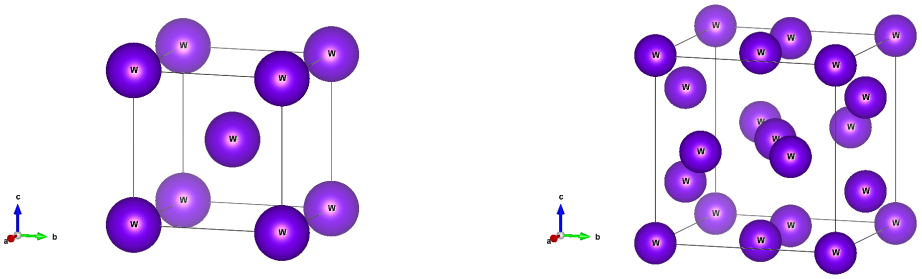

FIGURE A.1: Schematics of the W FCC (left) and the BCC (right) structure. (Constructed using VESTA.).

A.2 Tungsten silicides

A.2.1 Tetragonal WSi_2

Equilibrium tetragonal modification of tungsten silicide, characterized with the $MoSi_2$ structure (space group I4/mmm) [116]. The lattice constants are 3.2083(1) Å and 7.8216(4) Å, whereas the atomic positions used are (0 0 0) and (0 0 0.322(1)), respectively. A schematic figure of the crystal structure is shown in Figure A.2.

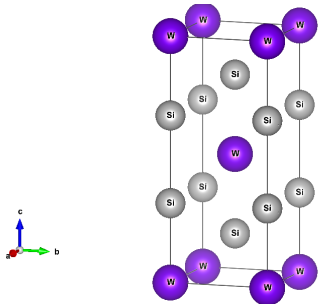

FIGURE A.2: Schematics of tetragonal WSi_2. (Constructed using VESTA.)

A.2.2 Hexagonal WSi_2

Metastable hexagonal modification of tungsten silicide, characterized with $CrSi_2$ type of structure (space group $P6_222$) [116]. The lattice constants are 4.614 Å and 6.414 Å, whereas the atomic positions used are (0.5 0 0.5) and (0.164 0.328 0.5), respectively [116]. A schematic figure of the crystal structure is shown in Figure A.3.

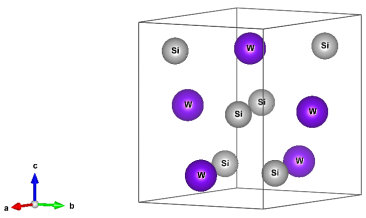

FIGURE A.3: Schematics of hexagonal WSi_2. (Constructed using VESTA.)

A.2.3 Tetragonal W_5Si_3

Equilibrium tetragonal modification of W_5Si_3, characterized with the $MoSi_2$ structure (space group I4/mmm) [116]. The lattice constants are 9.5917(3) Å and 4.9690(2) Å, whereas the atomic positions used are (0 0.5 0.25) and (0075(1) 0.222(1) 0) for the W atoms, and (0 0 0.25) and (0.168(6) 0.668(6) 0) for the Si atoms [116]. A schematic figure of the crystal structure is shown in Figure A.4.

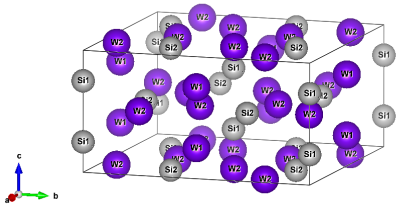

FIGURE A.4: Schematics of tetragonal W_5Si_3. (Constructed using VESTA.)

B

Pearson distribution function: Matlab script

A draft of the written Matlab script to estimate and optimize the Pearson distribution function from energy dispersive spectroscopy mapping. The script has not been optimized.

Note that only the Pearson IV has been used in this thesis, implying that Pearson I is not extensively tested.

With reservations to typing errors and other possible slips.

```
function pearsonProfile()

close all;
format compact;

imageDepth = 'length of image'; % nm;
K = 1;

% Acquiring EDS data from saved .tif-files
t = Tiff('filename.tif','r'); % Reading
imageData = double(read(t)); % Acquiring
imDataNum = 2; % imageData is a [pixel]x[pixel]x[imDataNum] matrix. The value of
    imDataNum to acquire the EDS data has to manually be determined
% figNum = 1; % Remove the following to plot the EDS picture to check imDataNum
% figure(figNum)
% imshow(imageData(:,:,imDataNum)); % A check if the data points are
    % in the selected imDataNum image
```

```
17 close(t);
18 imageDimensions = size(imageData);
19
20 % Define the interface between the Pt- and the implantaed Si; W is detected in the
       Pt-layer, probably due to limited detection sensitivity in the high-energy range
21 excludedStartLength = '# pixels on Pt-layer'; % Exclude detection from the Pt-layer
22 excludedEndLength = '# pixels on c-Si'; % Usually set to 0, but was sometimes > 0
       due to experimental limits
23 meanFilterRange = 2;
24 filterType = 1; %
25
26 increment = .001; % Number of increments/decrements when optimizing the Pearson
       function
27
28 % I have yet not been able to write the code for filterType = 3
29 if meanFilterRange > 5
30     fprintf('The meanFilterRange values is too large for this script...');
31     return;
32 elseif filterType ~= 1 && filterType ~= 3
33     fprintf('Filter type is not valid');
34     return;
35 end
36
37 foo = 0;
38 switch meanFilterRange % Taking care of boundary conditions
39     case 1
40         foo = 1;
41     case 2
42         foo = 2;
43     case 3
44         foo = 3;
45     case 4
46         foo = 4;
47     case 5
48         foo = 5;
49 end
50
51 depth = zeros(1,imageDimensions(2) - excludedStartLength); % Depth from the sample
       surface
52 list_W = zeros(1,imageDimensions(2) - excludedStartLength); % List containing the
       concentration values
53 pearsonDepth = zeros(1,imageDimensions(2) - excludedStartLength - excludedEndLength)
       ;
54     % Depth corresponding to the Pearson list
55 pearsonlist = zeros(1,imageDimensions(2) - excludedStartLength - excludedEndLength);
56 pearsonOptimized = zeros(1,imageDimensions(2) - excludedStartLength -
       excludedEndLength);
57
58 tempDepth = linspace(0,imageDepth,imageDimensions(2)); % Of personal preference
59
60 % Data values excluded from the Pearsion IV function
61 lost_startValues = zeros(1,excludedStartLength);
62 lost_startLength = zeros(1,excludedStartLength);
63 lost_endValues = zeros(1,excludedEndLength);
64 lost_endLength = zeros(1,excludedEndLength);
65 count_start = 1;
66 count_list = 1;
67 count_end = 1;
```

```


%%%%%%%%%%%%%%%%%%%%%%%%%%%%%%%%%%%%%%%%%%%%%%%%%%%%%%%%%%%%%%%%%%%%%%%%%%%%%%%%%%%%%%
%%%%%%%%%%%%%%%%%%%%%%%% MEAN FILTERING %%%%%%%%%%%%%%%%%%%%%%%%%%%%%%%%%%%%%%%%
%%%%%%%%%%%%%%%%%%%%%%%%%%%%%%%%%%%%%%%%%%%%%%%%%%%%%%%%%%%%%%%%%%%%%%%%%%%%%%%%%%%%%%


% Reading list values and saving them in separate lists, in addition to
% Note that 20 row pixels are white from the image text
for i = ((imageDimensions(1) - imageDimensions(2))/2) + 1 : ...
        imageDimensions(1) - (imageDimensions(1) - imageDimensions(2))/2
    if i <= excludedStartLength + ((imageDimensions(1) - ...
            imageDimensions(2))/2) % Pt layer
        lost_startLength(1,count_start) = tempDepth(i - ...
            ((imageDimensions(1) - imageDimensions(2))/2));
        lost_startValues(1,count_start) = sum(imageData(i,:,imDataNum))/...
            imageDimensions(2);
        count_start = count_start + 1;
    elseif i > excludedStartLength % Implanted area + "substrate"
        % Mean filtering of data values
        depth(1,count_list) = tempDepth(i - ((imageDimensions(1) - ...
            imageDimensions(2))/2));
        if i > (imageDimensions(1) - (imageDimensions(1) - ...
                imageDimensions(2))/2) - meanFilterRange
            % The foo'th last value
            for j = - meanFilterRange : 1 : meanFilterRange - foo
                if filterType == 1
                    list_W(1,count_list) = list_W(1,count_list) + ...
                        sum(imageData(i + j,:,imDataNum));
                elseif filterType == 3 % Unfinished
                    continue;
                end
            end
            switch meanFilterRange
                case 1 % End value
                    list_W(1,count_list) = (list_W(1,count_list) + ...
                        sum(imageData(i,:,imDataNum)))/...
                        (imageDimensions(2)*(2*meanFilterRange + 1));
                    count_list = count_list + 1;
                case 2
                    if foo == 2 % last value
                        list_W(1,count_list) = (list_W(1,count_list) + ...
                            sum(imageData(i,:,imDataNum)))/(imageDimensions(2)*4);
                        count_list = count_list + 1;
                    else % second last value
                        list_W(1,count_list) = (list_W(1,count_list) + ...
                            sum(imageData(i + meanFilterRange - 1,:,imDataNum)))...
                            /(imageDimensions(2)*(2*meanFilterRange + 1));
                        count_list = count_list + 1;
                        foo = foo + 1;
                    end
                case 3
                    if foo == 3 % last value
                        list_W(1,count_list) = (list_W(1,count_list) + ...
                            sum(imageData(i,:,imDataNum)))/(imageDimensions(2)*5);
                        count_list = count_list + 1;
                    elseif foo == 2 % second last value
                        list_W(1,count_list) = (list_W(1,count_value) + ...
```

```
126                         sum(imageData(i + meanFilteringRange - 2,:,imDataNum)))
                                /...
127                         (imageDimensions(2)*6);
128                     count_list = count_list + 1;
129                     foo = foo + 1;
130                 else
131                     list_W(1,count_list) = (list_W(1,count_value) + ...
132                         sum(imageData(i + meanFilteringRange - 1,:,imDataNum)))
                                /...
133                         (imageDimensions(2)*6);
134                     count_list = count_list + 1;
135                     foo = foo + 1;
136                 end
137             case 4
138                 if foo == 4 % last value
139                     list_W(1,count_list) = (list_W(1,count_list) + ...
140                         sum(imageData(i,:,imDataNum)))/(imageDimensions(2)*5);
141                     count_list = count_list + 1;
142                 elseif foo == 3 % second last value
143                     list_W(1,count_list) = (list_W(1,count_value) + ...
144                         sum(imageData(i + meanFilteringRange - 3,:,imDataNum)))
                                /...
145                         (imageDimensions(2)*6);
146                     count_list = count_list + 1;
147                     foo = foo + 1;
148                 elseif foo == 2
149                     list_W(1,count_list) = (list_W(1,count_value) + ...
150                         sum(imageData(i + meanFilteringRange - 2,:,imDataNum)))
                                /...
151                         (imageDimensions(2)*6);
152                     count_list = count_list + 1;
153                     foo = foo + 1;
154                 else
155                     list_W(1,count_list) = (list_W(1,count_value) + ...
156                         sum(imageData(i + meanFilteringRange - 1,:,imDataNum)))
                                /...
157                         (imageDimensions(2)*6);
158                     count_list = count_list + 1;
159                     foo = foo + 1;
160                 end
161             case 5
162                 if foo == 5 % last value
163                     list_W(1,count_list) = (list_W(1,count_list) + ...
164                         sum(imageData(i,:,imDataNum)))/(imageDimensions(2)*5);
165                     count_list = count_list + 1;
166                 elseif foo == 4 % second last value
167                     list_W(1,count_list) = (list_W(1,count_value) + ...
168                         sum(imageData(i + meanFilteringRange - 4,:,imDataNum)))
                                /...
169                         (imageDimensions(2)*6);
170                     count_list = count_list + 1;
171                     foo = foo + 1;
172                 elseif foo == 3
173                     list_W(1,count_list) = (list_W(1,count_value) + ...
174                         sum(imageData(i + meanFilteringRange - 3,:,imDataNum)))
                                /...
175                         (imageDimensions(2)*6);
176                     count_list = count_list + 1;
```

```
                        foo = foo + 1;
                    elseif foo == 2
                        list_W(1,count_list) = (list_W(1,count_value) + ...
                            sum(imageData(i + meanFilteringRange - 2,:,imDataNum)))/...
                            (imageDimensions(2)*6);
                        count_list = count_list + 1;
                        foo = foo + 1;
                    else
                        list_W(1,count_list) = (list_W(1,count_value) + ...
                            sum(imageData(i + meanFilteringRange - 1,:,imDataNum)))/...
                            (imageDimensions(2)*6);
                        count_list = count_list + 1;
                        foo = foo + 1;
                    end
            end
        else
            for j = -meanFilterRange:1:meanFilterRange
                list_W(1,count_list) = list_W(1,count_list) + ...
                    sum(imageData(i + j,:,imDataNum));
            end
            list_W(1,count_list) = list_W(1,count_list)/(imageDimensions(2)*...
                (2*meanFilterRange + 1));
            count_list = count_list + 1;
        end
    end
    if count_list > imageDimensions(1) - (imageDimensions(1) - ...
            imageDimensions(2))/2 - excludedEndLength  % Substrate
        lost_endLength(1,count_end) = tempDepth(i - ((imageDimensions(1) - ...
            imageDimensions(2))/2));
        lost_endValues(1,count_end) = list_W(1,count_list - 1)/imageDimensions(2);
        count_end = count_end + 1; % not mean filtered
    end
end



%%%%%%%%%%%%%%%%%%%%%%%%%%%%%%%%%%%%%%%%%%%%%%%%%%%%%%%%%%%%%%%%%%%%%%%%%%%%%%%%%%%%
%%%%%%%%%%%%%%%%%%%%%%%% ESTIMATING MOMENTS %%%%%%%%%%%%%%%%%%%%%%%%%%%%%%%%%%%%
%%%%%%%%%%%%%%%%%%%%%%%%%%%%%%%%%%%%%%%%%%%%%%%%%%%%%%%%%%%%%%%%%%%%%%%%%%%%%%%%%%%%


% Using middle Riemann sum
% Note maximum error: <= M_2(b-a)^3/24n^2, M_2 = |max(f''(x))|
list_W = list_W - list_W(1);
R_p = 0;
sum_N = 0;
delX = tempDepth(2);
for i = 1:imageDimensions(2)-excludedStartLength-excludedEndLength - 1
    R_p = R_p + delX*(depth(i) - depth(1))*...
        (list_W(i + 1) + list_W(i))/2;
    sum_N = sum_N + delX*(list_W(i + 1) + list_W(i))/2;
end
K = 1 / R_p; % Peak value is temporary set to 1
R_p = R_p/sum_N;

% Estimating experimental moment values
```

```
% mu_i = (int((x-R_p)^i*N(x)))/(int(N(x))) <=> moment mu_k, k = {2,3,4}
mu = zeros(3); % mu_{2,3,4}
for i = 1:imageDimensions(2)-excludedStartLength-excludedEndLength - 1
    mu(1) = mu(1) + delX*((((depth(i) + depth(i+1)- 2*depth(1))/2)-R_p)^2)*...
        (list_W(1,i + 1) + list_W(1,i))/2;

    mu(2) = mu(2) + delX*((((depth(i) + depth(i+1) - 2*depth(1))/2)-R_p)^3)*...
        (list_W(1,i + 1) + list_W(1,i))/2;

    mu(3) = mu(3) + delX*((((depth(i) + depth(i+1) - 2*depth(1))/2)-R_p)^4)*...
        (list_W(1,i + 1) + list_W(1,i))/2;
end
mu_2 = mu(1)/sum_N;
mu_3 = mu(2)/sum_N;
mu_4 = mu(3)/sum_N;

delR_p = sqrt(mu_2); % variance
gamma = mu_3/(delR_p^3); % skewness (sqrt(beta_1))
beta = mu_4/(delR_p^4); % kurtosis (beta_2)

crit = gamma^2*(beta + 3)^2/(4*((4*beta)-(3*gamma^2))*((2*beta)-(3*gamma)-6));

pearsonProfile = 0;
if crit < 0
    fprintf('crit = %.2d, therefore Pearson I\n', crit);
    pearsonProfile = 1;
elseif crit > 0 && crit < 1
    fprintf('crit = %.2d, therefore Pearson IV\n', crit);
    pearsonProfile = 4;
elseif crit == 1
    fprintf('crit = %.2d, therefore PEARSON V\n', crit);
    pearsonProfile = 5;
elseif crit > 1
    fprintf('crit = %.2d, therefore Pearson VI\n', crit);
    pearsonProfile = 6;
else
    fprintf('crit = %.2d, therefore the criteria does not apply...\n', crit);
    pearsonProfile = 0;
end

    A = ((10*beta)-(12*gamma^2)-18);
    b_0 = -delR_p^2*((4*beta)-(3*gamma^2))/A;
    b_1 = -gamma*delR_p*(beta+3)/A;
    b_2 = -((2*beta)-(3*gamma^2)-6)/A; %
    a = b_1;

%%%%%%%%%%%%%%%%%%%%%%%%%%%%%%%%%%%%%%%%%%%%%%%%%%%%%%%%%%%%%%%%%%%%%%%%%%%%%%%%
%%%%%%%%%%%%%%%%%%%% DETERMINING PEARSON DISTRIBUTION %%%%%%%%%%%%%%%%%%%%%%%%%
%%%%%%%%%%%%%%%%%%%%%%%%%%%%%%%%%%%%%%%%%%%%%%%%%%%%%%%%%%%%%%%%%%%%%%%%%%%%%%%%

if pearsonProfile == 4
    fprintf('\nbeta = %.2f < %.2f\n',beta,((3*((13*gamma^2)+16))+(6*(gamma^2+4)
        ^(3/2)))/(32-gamma^2));

%     if beta < ((3*((13*gamma^2)+16))+(6*((gamma^2+4)^(3/2))))/(32-gamma^2) % This
    command doesn't always result well...
%         fprintf('\nbeta = %.2f < %.2f\n',beta,((3*((13*gamma^2)+16))+(6*(gamma
    ^2+4)^(3/2)))/(32-gamma^2));
```

```
288 %           beta = ((3*((13*gamma^2)+16))+(6*(gamma^2+4)^(3/2)))/(32-gamma^2);
289 %       end
290       for i = 1:imageDimensions(2) - excludedStartLength - excludedEndLength
291           pearsonDepth(1,i) = (depth(1,i) - R_p - lost_startLength(excludedStartLength
                  ));
292           temp1 = (b_0+(b_1*pearsonDepth(1,i))+(b_2*pearsonDepth(1,i)^2));
293       if temp1 < 0 % Absolute value
294           temp1 = -1*temp1;
295       end
296           pearsonlist(1,i) = K*temp1^(1/(2*b_2))*...
297               exp(-((b_1/(2*b_2))+a)*(2/(sqrt((4*b_2*b_0)-(b_1^2)))*...
298               atan(((2*b_2*pearsonDepth(1,i))+b_1)/sqrt((4*b_2*b_0)-(b_1^2)))));
299       end
300       fprintf('\nThe following variables are as follows: \n\nR_p("mean") = %.3d \nmu_2
              = %.3d, \nmu_3 = %.3d, \nmu_4 = %.3d, \ndelR_p(std.dev.) = %.3d, \n',R_p,
              mu_2,mu_3,mu_4,delR_p);
301       fprintf('gamma(skew.) = %.3d, \nbeta(kurt.) = %.3d, \nb_0 = %.3d, \nb_1 = %.3d,
              \nb_2 = %.3d\n',gamma,beta,b_0,b_1,b_2);
302   elseif pearsonProfile == 1
303       fprintf('The discriminant is non-negative, which implies that the \nPearson
              distribution is the "logarithmic case."\n');
304
305       a_1 = (-b_1 - sqrt(b_1^2-(4*b_2*b_0)))/(2*b_2);
306       a_2 = (-b_1 + sqrt(b_1^2-(4*b_2*b_0)))/(2*b_2);
307       nu = 1/(b_2*(a_1-a_2));
308       fprintf('a_1 = %.2d, a_2 = %.2d and nu = %.2d\n',a_1,a_2,nu);
309
310
311       if (a_1 < 0 && 0 < a_2) || (a_1 > 0 && a_2 < 0)% Pearson I
312           fprintf('The data set corresponds to a Pearson type I distribution.\n');
313       if abs(denom) > sqrt(realmin)
314           m1 = (c1 + a1) ./ (c2 .* (a2 - a1));
315           m2 = -(c1 + a2) ./ (c2 .* (a2 - a1));
316       else
317            % c1 and c2 -> Inf, but c1/c2 has finite limit
318           m1 = c1 ./ (c2 .* (a2 - a1));
319           m2 = -c1 ./ (c2 .* (a2 - a1));
320       end
321
322           if abs(A) > sqrt(realmin)
323               m_1 = (a+a_1)/(b_2*(a_2-a_1));
324               m_2 = -(a+a_2)/(b_2*(a_2-a_1));
325           else
326               m_1 = a/(b_2*(a_2-a_1));
327               m_2 = -a/(b_2*(a_2-a_1));
328           end
329           if (real(a_1) > real(a_2)), tmp = a_1; a_1 = a_2; a_2 = tmp; end
330               for i = 1:imageDimensions(2) - excludedStartLength - excludedEndLength
331                   pearsonDepth(1,i) = ((depth(1,i) - a_1 - depth(1)))/(a_2-a_1);
332                   pearsonlist = betapdf(pearsonDepth, m_1+1, m_2+1)/delR_p/(a_2-a_1);
333               end
334       else % General solution; not completed nor tried
335           fprintf('The data set correspond to the general solution of a Pearson
                  distribution.\n');
336           for i = 1:imageDimensions(2) - excludedStartLength - excludedEndLength
337               pearsonlist(1,i) = (pearsonDepth(1,i)-a_1)^(-nu*(a_1-a))*(pearsonDepth
                      (1,i)-a_2)^(nu*(a_2-a));
338               pearsonDepth(1,i) = depth(1,i);
```

```matlab
            end
        end
end

%%%%%%%%%%%%%%%%%%%%%%%%%%%%%%%%%%%%%%%%%%%%%%%%%%%%%%%%%%%%%%%%%%%%%%%%%%%%%%%%%
%%%%%%%%%%%%%%%%%%%%%%%%%%%%%%%%% OPTIMIZATION %%%%%%%%%%%%%%%%%%%%%%%%%%%%%%%%%%
%%%%%%%%%%%%%%%%%%%%%%%%%%%%%%%%%%%%%%%%%%%%%%%%%%%%%%%%%%%%%%%%%%%%%%%%%%%%%%%%%

% Lowering W_list
pearsonMax = 0.0;
for i = 1:imageDimensions(2) - excludedStartLength - excludedEndLength
    if pearsonlist(1,i) > pearsonMax
        pearsonMax = pearsonlist(1,i);
        pearsonMaxLocation = i;
    end
end
pearsonDepth = pearsonDepth + R_p + depth(1,1);


scale = 0.0;
num = 0;
range = 10;
for i = -range:1:range
    scale = scale + list_W(i+pearsonMaxLocation);
    num = num + 1;
end
subtract = pearsonlist(1);
pearsonlist = pearsonlist - subtract;
str = size(lost_startValues);
lost_startValues = lost_startValues - lost_startValues(str(2));

lost_startValues = num.*(lost_startValues)./scale;
list_W = num.*(list_W)./scale;
pearsonlist = pearsonlist./pearsonMax;

MSE_exp = 0.0; MSE_optimized = 0.0;
for i = 1 : imageDimensions(2) - excludedStartLength - excludedEndLength
    MSE_exp = MSE_exp + (pearsonlist(1,i) - list_W(1,i))^2;
end
MSE_exp = MSE_exp/(imageDimensions(2) - excludedStartLength - excludedEndLength);

optimized = false; del = 0.0; gam = 0.0; bet = 0.0;
delOpt = 0.0; gamOpt = 0.0; betOpt = 0.0;
steppingUpDel = false; steppingDownDel = false;
steppingUpGam = true; steppingDownGam = true;
steppingUpBet = true; steppingDownBet = true;
parameter = 1;
while optimized == false
    if parameter == 1
        del = del + increment;
        up = MSE_estimator(K, depth, list_W, R_p, delR_p + del, gamma, beta, pearsonProfile, excludedStartLength, excludedEndLength, lost_startLength, imageDimensions);
        down = MSE_estimator(K, depth, list_W, R_p, delR_p - del, gamma, beta, pearsonProfile, excludedStartLength, excludedEndLength, lost_startLength, imageDimensions);
    elseif parameter == 2
        gam = gam + increment;
```

```
393         steppingUpDel = true; steppingDownDel = true;
394         steppingUpGam = false; steppingDownGam = false;
395         up = MSE_estimator(K, depth, list_W, R_p, delOpt, gamma + gam, beta,
                pearsonProfile, excludedStartLength, excludedEndLength, lost_startLength
                , imageDimensions);
396         down = MSE_estimator(K, depth, list_W, R_p, delOpt, gamma - gam, beta,
                pearsonProfile, excludedStartLength, excludedEndLength, lost_startLength
                , imageDimensions);
397     elseif parameter == 3
398         bet = bet + increment;
399         steppingUpGam = true; steppingDownGam = true;
400         steppingUpBet = false; steppingDownBet = false;
401         up = MSE_estimator(K, depth, list_W, R_p, delOpt, gamOpt, beta + bet,
                pearsonProfile, excludedStartLength, excludedEndLength, lost_startLength
                , imageDimensions);
402         down = MSE_estimator(K, depth, list_W, R_p, delOpt, gamOpt, beta - bet,
                pearsonProfile, excludedStartLength, excludedEndLength, lost_startLength
                , imageDimensions);
403     else
404         steppingUpBet = true; steppingDownBet = true;
405         MSE_optimized  = MSE_estimator(K, depth, list_W, R_p, delOpt, gamOpt, betOpt
                , pearsonProfile, excludedStartLength, excludedEndLength,
                lost_startLength, imageDimensions);
406         fprintf('The optimized mean square value is %.2d, in comparison with the
                experimental value: %.2d\n', MSE_optimized,MSE_exp);
407         optimized = true;
408     end
409
410     if up < down
411         while steppingUpDel == false
412             up1 = MSE_estimator(K, depth, list_W, R_p, delR_p + del, gamma, beta,
                    pearsonProfile, excludedStartLength, excludedEndLength,
                    lost_startLength, imageDimensions);
413             up2 = MSE_estimator(K, depth, list_W, R_p, delR_p + del + increment,
                    gamma, beta, pearsonProfile, excludedStartLength, excludedEndLength,
                     lost_startLength, imageDimensions);
414             if up2 < up1
415                 del = del + increment;
416             elseif up1 < up2
417                 delOpt = delR_p + del;
418                 steppingUpDel = true;
419                 parameter = parameter + 1;
420             else % up1 = up2
421                 delOpt = delR_p + del;
422                 steppingUpDel = true;
423                 parameter = parameter + 1;
424             end
425         end
426         while steppingUpGam == false
427             up1 = MSE_estimator(K, depth, list_W, R_p, delOpt, gamma + gam, beta,
                    pearsonProfile, excludedStartLength, excludedEndLength,
                    lost_startLength, imageDimensions);
428             up2 = MSE_estimator(K, depth, list_W, R_p, delOpt, gamma + gam +
                    increment, beta, pearsonProfile, excludedStartLength,
                    excludedEndLength, lost_startLength, imageDimensions);
429             if up2 < up1
430                 gam = gam + increment;
431             elseif up1 < up2
```

```
432                 gamOpt = gamma + gam;
433                 steppingUpGam = true;
434                 parameter = parameter + 1;
435             else % up1 = up2
436                 gamOpt = gamma + gam;
437                 steppingUpGam = true;
438                 parameter = parameter + 1;
439             end
440         end
441         while steppingUpBet == false
442             up1 = MSE_estimator(K, depth, list_W, R_p, delOpt, gamOpt, beta + bet,
                    pearsonProfile, excludedStartLength, excludedEndLength,
                    lost_startLength, imageDimensions);
443             up2 = MSE_estimator(K, depth, list_W, R_p, delOpt, gamOpt, beta + bet +
                    increment, pearsonProfile, excludedStartLength, excludedEndLength,
                    lost_startLength, imageDimensions);
444             if up2 < up1
445                 bet = bet + increment;
446             elseif up1 < up2
447                 betOpt = beta + bet;
448                 steppingUpBet = true;
449                 parameter = parameter + 1;
450             else % up1 = up2
451                 betOpt = beta + bet;
452                 steppingUpBet = true;
453                 parameter = parameter + 1;
454             end
455         end
456
457     elseif down < up
458         while steppingDownDel == false
459             down1 = MSE_estimator(K, depth, list_W, R_p, delR_p - del, gamma, beta,
                    pearsonProfile, excludedStartLength, excludedEndLength,
                    lost_startLength, imageDimensions);
460             down2 = MSE_estimator(K, depth, list_W, R_p, delR_p - del - increment,
                    gamma, beta, pearsonProfile, excludedStartLength, excludedEndLength,
                     lost_startLength, imageDimensions);
461             if down2 < down1
462                 del = del + increment;
463             elseif down1 < down2
464                 delOpt = delR_p - del;
465                 steppingDownDel = true;
466                 parameter = parameter + 1;
467             else % down1 = down2
468                 delOpt = delR_p - del;
469                 steppingDownDel = true;
470                 parameter = parameter + 1;
471             end
472         end
473         while steppingDownGam == false
474             down1 = MSE_estimator(K, depth, list_W, R_p, delOpt, gamma - gam, beta,
                    pearsonProfile, excludedStartLength, excludedEndLength,
                    lost_startLength, imageDimensions);
475             down2 = MSE_estimator(K, depth, list_W, R_p, delOpt, gamma - gam -
                    increment, beta, pearsonProfile, excludedStartLength,
                    excludedEndLength, lost_startLength, imageDimensions);
476             if down2 < down1
477                 gam = gam + increment;
```

```
478             elseif down1 < down2
479                 gamOpt = gamma - gam;
480                 steppingDownGam = true;
481                 parameter = parameter + 1;
482             else % down1 = down2
483                 gamOpt = gamma - gam;
484                 steppingDownGam = true;
485                 parameter = parameter + 1;
486             end
487         end
488         while steppingDownBet == false
489             down1 = MSE_estimator(K, depth, list_W, R_p, delOpt, gamOpt, beta - bet,
                      pearsonProfile, excludedStartLength, excludedEndLength,
                    lost_startLength, imageDimensions);
490             down2 = MSE_estimator(K, depth, list_W, R_p, delOpt, gamOpt, beta - bet
                    - increment, pearsonProfile, excludedStartLength, excludedEndLength,
                     lost_startLength, imageDimensions);
491             if down2 < down1
492                 bet = bet + increment;
493                 % Need to check beta against the lower limit here
494             elseif down1 < down2
495                 betOpt = beta - bet;
496                 steppingDownBet = true;
497                 parameter = parameter + 1;
498             else % down1 = down2
499                 betOpt = beta - bet;
500                 steppingDownBet = true;
501                 parameter = parameter + 1;
502             end
503         end
504     else % The values are identical from the beginning
505         parameter = parameter + 1;
506     end
507 end
508
509 critOpt = gamOpt^2*(betOpt + 3)^2/(4*((4*betOpt)-(3*gamOpt^2))*((2*betOpt)-(3*gamOpt
        )-6));
510 pearsonProfileOpt = 0;
511 if critOpt < 0
512     fprintf('critOpt = %.2d, therefore Pearson I\n', critOpt);
513     pearsonProfileOpt = 1;
514 elseif critOpt > 0 && critOpt < 1
515     fprintf('critOpt = %.2d, therefore Pearson IV\n', critOpt);
516     pearsonProfileOpt = 4;
517 elseif critOpt == 1
518     fprintf('critOpt = %.2d, therefore PEARSON V\n', critOpt);
519     pearsonProfileOpt = 5;
520 elseif critOpt > 1
521     fprintf('critOpt = %.2d, therefore Pearson VI\n', critOpt);
522     pearsonProfileOpt = 6;
523 else
524     fprintf('critOpt = %.2d, therefore the criteria does not apply...\n', critOpt);
525     pearsonProfileOpt = 0;
526 end
527
528 AOpt = ((10*betOpt)-(12*gamOpt^2)-18);
529 b0Opt = -delOpt^2*((4*betOpt)-(3*gamOpt^2))/AOpt;
530 b1Opt = -gamOpt*delOpt*(betOpt+3)/AOpt;
```

```
531 b2Opt = -((2*betOpt)-(3*gamOpt^2)-6)/AOpt; %
532 aOpt = b1Opt;
533
534 if pearsonProfileOpt == 4
535 %     if beta < ((3*((13*gamma^2)+16))+(6*((gamma^2+4)^(3/2))))/(32-gamma^2)
536 %         fprintf('\nbeta = %.2f < %.2f\n',beta,((3*((13*gamma^2)+16))+(6*(gamma
      ^2+4)^(3/2)))/(32-gamma^2));
537 %         beta = ((3*((13*gamma^2)+16))+(6*(gamma^2+4)^(3/2)))/(32-gamma^2); % This
      doesn't always result well...
538 %     end
539     for i = 1:imageDimensions(2) - excludedStartLength-excludedEndLength
540         pearsonDepth(1,i) = (depth(1,i) - R_p - lost_startLength(excludedStartLength
              ));
541         temp1 = (b0Opt+(b1Opt*pearsonDepth(1,i))+(b2Opt*pearsonDepth(1,i)^2));
542     if temp1 < 0 % Absolute value
543         temp1 = -1*temp1;
544     end
545         pearsonOptimized(1,i) = K*temp1^(1/(2*b2Opt))*...
546             exp(-((b1Opt/(2*b2Opt))+aOpt)*(2/(sqrt((4*b2Opt*b0Opt)-(b1Opt^2)))*...
547             atan(((2*b2Opt*pearsonDepth(1,i))+b1Opt)/sqrt((4*b2Opt*b0Opt)-(b1Opt^2))
                  )));
548     end
549     fprintf('\nThe following variables are as follows: \n\nR_p("mean") = %.3d \nmu_2
          = %.3d, \nmu_3 = %.3d, \nmu_4 = %.3d, \ndelR_p(opt.)(std.dev.) = %.3d, \n',
          R_p,mu_2,mu_3,mu_4,delOpt);
550     fprintf('gamma(opt)(skew.) = %.3d, \nbeta(opt)(kurt.) = %.3d, \nb_0(opt) = %.3d,
          \nb_1(opt) = %.3d, \nb_2(opt) = %.3d\n',gamOpt,betOpt,b0Opt,b1Opt,b2Opt);
551 elseif pearsonProfileOpt == 1
552     fprintf('The discriminant is non-negative, which implies that the \nPearson
          distribution is the "logarithmic case."\n');
553
554     a1Opt = (-b1Opt - sqrt(b1Opt^2-(4*b2Opt*b0Opt)))/(2*b2Opt);
555     a2Opt = (-b1Opt + sqrt(b1Opt^2-(4*b2Opt*b0Opt)))/(2*b2Opt);
556     nuOpt = 1/(b2Opt*(a1Opt-a2Opt));
557     fprintf('a_1(opt) = %.2d, a_2(opt) = %.2d and nu(opt) = %.2d\n',a1Opt,a2Opt,
          nuOpt);
558
559
560     if (a1Opt < 0 && 0 < a2Opt) || (a1Opt > 0 && a2Opt < 0)% Pearson I
561         fprintf('The data set corresponds to a Pearson type I distribution.\n');
562         if abs(AOpt) > sqrt(realmin)
563             m1Opt = (aOpt-a1Opt)/(b2Opt*(a1Opt-a2Opt));
564             m2Opt = (aOpt-a2Opt)/(b2Opt*(a2Opt-a1Opt));
565         else
566             m1Opt = aOpt/(b2Opt*(a1Opt-a2Opt));
567             m2Opt = aOpt/(b2Opt*(a2Opt-a1Opt));
568         end
569         if (a1Opt < 0 && 0 < a2Opt)
570             for i = 1:imageDimensions(2) - excludedStartLength - excludedEndLength
571                 pearsonDepth(1,i) = ((depth(1,i) - a1Opt - lost_startLength(
                      excludedStartLength)))/(a2Opt-a1Opt);
572                 pearsonOptimized(1,i) = ((1+pearsonDepth(1,i)/a1Opt)^m1Opt)*(1-
                      pearsonDepth(1,i)/a2Opt)^m2Opt;
573             end
574         else
575             for i = 1:imageDimensions(2) - excludedStartLength - excludedEndLength
576                 pearsonDepth(1,i) = ((depth(1,i) - a2Opt - lost_startLength(
                      excludedStartLength)))/(a1Opt-a2Opt);
```

```
                pearsonOptimized(1,i) = ((1+pearsonDepth(1,i)/a1Opt)^m1Opt)*(1-pearsonDepth(1,i)/a2Opt)^m2Opt;
            end
        end
        %pearsonIVlist = betapdf(pearsonDepth, m_1+1, m_2+1);
    else % General solution
        fprintf('The data set correspond to the general solution of a Pearson distribution.\n');
        for i = 1:imageDimensions(2) - excludedStartLength - excludedEndLength
            pearsonOptimized(1,i) = (pearsonDepth(1,i)-a1Opt)^(-nuOpt*(a1Opt-aOpt))*(pearsonDepth(1,i)-a2Opt)^(nuOpt*(a2Opt-aOpt));
            pearsonDepth(1,i) = depth(1,i);
        end
    end
end
pearsonOptMax = 0.0; pearsonOptMaxLocation = 0;
for i = 1:imageDimensions(2) - excludedStartLength - excludedEndLength
    if pearsonOptimized(1,i) > pearsonOptMax
        pearsonOptMax = pearsonOptimized(1,i);
        pearsonOptMaxLocation = i;
    end
end
pearsonDepth = pearsonDepth + R_p + lost_startLength(excludedStartLength);
pearsonOptimized = pearsonOptimized./pearsonOptMax;
pearsonOptimized = pearsonOptimized - pearsonOptimized(1,1);
fprintf('The list has been scaled %.5d and moved %.5d\n',pearsonOptMax,pearsonOptimized(1,1));

%%%%%%%%%%%%%%%%%%%%%%%%%%%%%%%%%%%%%%%%%%%%%%%%%%%%%%%%%%%%%%%%%%%%%%%%%%%%%%%%
%%%%%%%%%%%%%%%%%%%%%%%%%%%%%%%% PLOTTING %%%%%%%%%%%%%%%%%%%%%%%%%%%%%%%%%%%%%%%%
%%%%%%%%%%%%%%%%%%%%%%%%%%%%%%%%%%%%%%%%%%%%%%%%%%%%%%%%%%%%%%%%%%%%%%%%%%%%%%%%

print = ''; printOpt = '';
if pearsonProfile == 1
    print = 'I';
elseif pearsonProfile == 4
    print = 'IV';
end
if pearsonProfileOpt == 1
    printOpt = 'I';
elseif pearsonProfileOpt == 4
    printOpt = 'IV';
end

figNum = figNum + 1;
figure(figNum);
hold on;
plot(lost_startLength, lost_startValues);%/max(lost_startValues)));
plot(depth, list_W);
plot(pearsonDepth, pearsonlist, 'LineWidth', 2);
plot(pearsonDepth, pearsonOptimized, 'LineWidth',2);
title('Pearson fitted functions');
xlabel('Depth [nm]');
ylabel('Arbitrary units')
legend({'Excluded mean filtered EDS data','mean filtered EDS data',['Pearson ' print ' fitted from EDS data'], ['Optimized Pearson ' printOpt ' curve']},'Location','northeast');
hold off;
```

```
629
630 figNum = figNum + 1;
631 figure(figNum);
632 hold on;
633 plot(depth, list_W);
634 plot(pearsonDepth, pearsonlist, 'LineWidth', 2);
635 plot(pearsonDepth, pearsonOptimized, 'LineWidth',2);
636 title('Pearson fitted functions');
637 xlabel('Depth [nm]');
638 ylabel('Arbitrary units')
639 legend({'Mean filtered EDS data',['Pearson ' print ' fitted from EDS data'], ['
    Optimized Pearson ' printOpt ' curve']},'Location','northeast');
640 hold off;
641 end
642
643
644
645 function MSE_out = MSE_estimator(K, depth, list_W, R_p, delR_p, gamma, beta,
    distributionProfile, excludedStartLength, excludedEndLength, lost_startLength,
    imageDimensions)
646 MSE_temp = 0.0;
647 tempPearsonlist = zeros(1,imageDimensions(2) - excludedStartLength -
    excludedEndLength);
648 pearsonDepth = zeros(1,imageDimensions(2) - excludedStartLength - excludedEndLength)
    ;
649
650 A = ((10*beta)-(12*gamma^2)-18);
651 b_0 = -delR_p^2*((4*beta)-(3*gamma^2))/A;
652 b_1 = -gamma*delR_p*(beta+3)/A;
653 b_2 = -((2*beta)-(3*gamma^2)-6)/A;
654 a = b_1;
655
656 if distributionProfile == 4
657 %     if beta < ((3*((13*gamma^2)+16))+(6*((gamma^2+4)^(3/2))))/(32-gamma^2)
658 %     fprintf('\nbeta = %.2f < %.2f\n',beta,((3*((13*gamma^2)+16))+(6*(gamma^2+4)
    ^(3/2))))/(32-gamma^2));
659 %         beta = ((3*((13*gamma^2)+16))+(6*(gamma^2+4)^(3/2))))/(32-gamma^2);
660 %     end
661     for i = 1:imageDimensions(2) - excludedStartLength-excludedEndLength
662         pearsonDepth(1,i) = (depth(1,i) - R_p - lost_startLength(excludedStartLength
                ));
663         temp1 = (b_0+(b_1*pearsonDepth(1,i))+(b_2*pearsonDepth(1,i)^2));
664     if temp1 < 0 % Absolute value
665         temp1 = -1*temp1;
666     end
667         tempPearsonlist(1,i) = K*temp1^(1/(2*b_2))*...
668             exp(-((b_1/(2*b_2))+a)*(2/(sqrt((4*b_2*b_0)-(b_1^2))))*...
669             atan(((2*b_2*pearsonDepth(1,i))+b_1)/sqrt((4*b_2*b_0)-(b_1^2)))));
670     end
671 elseif distributionProfile == 1
672     a_1 = (-b_1 - sqrt(b_1^2-(4*b_2*b_0)))/(2*b_2);
673     a_2 = (-b_1 + sqrt(b_1^2-(4*b_2*b_0)))/(2*b_2);
674     nu = 1/(b_2*(a_1-a_2));
675
676
677     if (a_1 < 0 && 0 < a_2) || (a_1 > 0 && a_2 < 0)% Pearson I
678 %         fprintf('The data set corresponds to a Pearson type I distribution.\n');
679         if abs(A) > sqrt(realmin)
```

```
680             m_1 = (a-a_1)/(b_2*(a_1-a_2));
681             m_2 = (a-a_2)/(b_2*(a_2-a_1));
682         else
683             m_1 = a/(b_2*(a_1-a_2));
684             m_2 = a/(b_2*(a_2-a_1));
685         end
686         if (a_1 < 0 && 0 < a_2)
687             for i = 1:imageDimensions(2) - excludedStartLength - excludedEndLength
688                 pearsonDepth(1,i) = ((depth(1,i) - a_1 - lost_startLength(
                        excludedStartLength)))/(a_2-a_1);
689                 tempPearsonlist(1,i) = ((1+pearsonDepth(1,i)/a_1)^m_1)*(1-
                        pearsonDepth(1,i)/a_2)^m_2;
690             end
691         else
692             for i = 1:imageDimensions(2) - excludedStartLength - excludedEndLength
693                 pearsonDepth(1,i) = ((depth(1,i) - a_2 - lost_startLength(
                        excludedStartLength)))/(a_1-a_2);
694                 tempPearsonlist(1,i) = ((1+pearsonDepth(1,i)/a_1)^m_1)*(1-
                        pearsonDepth(1,i)/a_2)^m_2;
695             end
696         end
697         %pearsonIVlist = betapdf(pearsonDepth, m_1+1, m_2+1);
698     else % General solution
699         for i = 1:imageDimensions(2) - excludedStartLength - excludedEndLength
700             tempPearsonlist(1,i) = (pearsonDepth(1,i)-a_1)^(-nu*(a_1-a))*(
                    pearsonDepth(1,i)-a_2)^(nu*(a_2-a));
701             pearsonDepth(1,i) = depth(1,i);
702         end
703     end
704 end
705 pearsonDepth = pearsonDepth + R_p + lost_startLength(excludedStartLength);
706
707
708 pearsonMax = 0.0;
709 for i = 1:imageDimensions(2) - excludedStartLength - excludedEndLength
710     if tempPearsonlist(1,i) > pearsonMax
711         pearsonMax = tempPearsonlist(1,i);
712     end
713 end
714 subtract = tempPearsonlist(1);
715 tempPearsonlist = tempPearsonlist - subtract;
716 tempPearsonlist = tempPearsonlist./pearsonMax;
717
718 MSE_temp = 0.0;
719 for i = 1 : imageDimensions(2) - excludedStartLength - excludedEndLength
720     MSE_temp = MSE_temp + (tempPearsonlist(1,i) - list_W(1,i))^2;
721 end
722
723     MSE_out = MSE_temp/(imageDimensions(2) - excludedStartLength - excludedEndLength
            );
724 end
```

Bibliography

[1] A. B. Arons and M. B. Peppard, "Einstein's proposal of the photon concept - a translation of the Annelen der physik paper of 1905", American journal of physics **33**, 367–374 (1965).

[2] W. Smith, "Effect of light on selenium during the passage of an electric current", Nature **7**, 303 (1873).

[3] T. Twidell J. & Weir, *Renewable energy resources*, 3rd ed. (Routledge, 2015), pp. 151 –201.

[4] J. Nelson, *The physics of solar cells* (Imperial College Press, 2003), pp. 1–78, 177–252, 298–325.

[5] E. Becquerel, *Mémoire sur les effets électriques produits sous l'influence des rayons solaires.* 1839.

[6] C. E. Fritts, "On the fritts selenium cells and batteries.", Journal of the Franklin Institute **119**, 221 –232 (1885).

[7] G. Conibeer, "Third-generation photovoltaics", materialstoday **10**, 42–50 (2007).

[8] M. A. Green, *Third generation photovoltaics, Advanced solar energy conversion*, edited by T. Kamiya, B. Monemar, H. Venghaus, and Y. Yamamoto (Springer-Verlag, 2003), pp. 59–109.

[9] A. M. Bagher, M. M. A. Vahid, and M. Mohsen, "Types of solar cells and application", American Journal of Optics and Photonics **3**, 94–113 (2015).

[10] A. V. Da Rosa, *Fundamentals of renewable energy processes*, 2nd ed. (Elsevier Inc., 2009), pp. 625–720.

[11] *Technology roadmap - Solar photovoltaic energy*, tech. rep. (IEA Publications, 2014), p. 12.

[12] G. Conibeer and A. Willoughby, eds., *Solar cell materials: Developing technologies*, 1st ed. (John Wiley & Sons, Ltd, 2014), pp. 1–4, 283 –314.

[13]W. Yang, J. Mathews, and J. S. Williams, "Hyperdoping of Si by ion implantation and pulsed laser melting", Materials Science in Semiconductor Processing **62**, 103–114 (2016).

[14]A. Luque and A. Martí, "Increasing the efficiency of ideal solar cells by photon induced transitions at intermediate levels", Physical Review Letters **78**, 5014–5017 (1997).

[15]A.Luque1, A. Martí, and C. Stanley, "Understanding intermediate-band solar cells", Nature Photonics **3**, 146–152 (2012).

[16]T. Nozawa and Y. Arakawa, "Detailed balance limit of the efficiency of multilevel intermediate band solar cells", APPLIED PHYSICS LETTERS **98**, 171108 (2011).

[17]C. B. Simmons, A. J. Akey, J. P. Mailoa, D. Recht, M. J. Aziz, and T. Buonassisi, "Enhancing the infrared photoresponse of silicon by controlling the fermi level location within an impurity band", Advanced functional materials **24**, 2852–2858 (2014).

[18]Y. Okada et al., "Intermediate band solar cells: Recent progress and future directions.", Applied physics Reviews, 2–49 (2015).

[19]A. Luque and A. Martí, "The intermediate band solar cell: Progress toward the realization of an attractive concept", Advanced Materials **22**, 160–174 (2010).

[20]W. Shockley and H. J. Queisser, "Detailed balance limit of efficiency of p-n junction solar cells", Journal of applied physics **32**, 510 –519 (1961).

[21]L. Cuadra, A. Martí, and A. Luque, "Influence of the overlap between the absorption coefficients on the efficiency of the intermediate band solar cell", IEEE Transactions on Electron Devices **51**, 1002–1007 (2004).

[22]G. Azzouzi and W. Tazibtb, "Improving silicon solar cell efficiency by using the impurity photovoltaic effect", Energy Procedia **41**, 40–49 (2013).

[23]A. Martí and A. Luque, "Intermediate band solar cells", Trans Tech Publications **74**, 143–150 (2010).

[24]A. Luque, A. Martí, E. Antolín, and C. Tablero, "Intermediate bands versus levels in non-radiative recombination", Physica B: Condensed Matter **382**, 320–327 (2006).

[25]N. F. Mott, "Metal-insulator transition", Reviews of modern physics **40**, 677–683 (1968).

[26]K. Momma and F. Izumi, "Vesta: A three-dimensional visualization system for electronic and structural analysis", Journal of Applied Crystallography **41**, 653–658 (2008).

[27]M. Grundmann, *The physics of semiconductors - an introduction including devices and nanophysics*, 1st ed. (Springer, 2006), pp. 111–147.

[28]D. Recht et al., "Supersaturating silicon with transition metals by ion implantation and pulsed laser melting", Journal of applied physics **114**, 124903 (2013).

[29]M. J. Aziz, "Model for solute redistribution during rapid solidification", Journal of Applied Physics **53** (1982) 10.1063/1.329867.

[30]C. Quan, M. Zhi-Hua, X. Chun-Lai, Z. Yu-Hua, and W. Qi-Ming, "Detailed balance limit efficiency of silicon intermediate band solar cells", Chineese physics B **20**, 097103 (2011).

[31]J. T. Sullivan, C. B. Simmons, T Buonassisi, and J. J. Krich, "Targeted search for effective intermediate band solar cell materials", IEEE JOURNAL OF PHOTOVOLTAICS **5**, 212–218 (2015).

[32]H. S. Hauge, "Fabrication and characterization of an intermediate band material based on ion implantation and pulsed laser melting of Ag in FZ-Si.", MA thesis (Department of Physics, 2015).

[33]H. Lysne, "Transmission electron microscopy of cellular breakdown in silver-implanted silicon for intermediate band solar cells", Project work at Norwegian University of Science and Technology, 2016.

[34]H. Lysne, "3D TEM characterization of silver implanted silicon for intermediate band solar cells.", MA thesis (Department of Physics, 2017).

[35]J. A. Sørhaug, "Transmission electron microscopy and atomic force microscopy on recrystallized Ag-implanted Si - A study of potential intermediate band solar cell material", Project work at Norwegian University of Science and Technology, 2018.

[36]J. M. Warrender, J. Mathews, D. Recht, M. Smith, S. Gradečak, and M. J. Aziz, "Morphological stability during solidification of silicon incorporating metallic impurities", JOURNAL OF APPLIED PHYSICS **115**, 1–8 (2014).

[37]A. J. Akey, D. Recht, J. Williams, M. J. Aziz, and T. Buonassisi, "Single-phase filamentary cellular breakdown via laser-induced solute segregation", Advanced Functional Materials **25** (2015) 10.1002/adfm.201501450.

[38]W. Yang et al., "Au-rich filamentary behavior and associated subband gap optical absorption in hyperdoped Si", PHYSICAL REVIEW MATERIALS **1** (2017) 10.1103/PhysRevMaterials.1.074602.

[39]S. I. T. Ando and C. Munakata, "Deep-level transient spectroscopy on p-type silicon crystals containing tungsten impurities", Journal of Applied Physics **70**, 5401–5403 (1991).

[40]H. K. Y. Fujisaki T. Ando and Y. Takano, "Characterization of tungsten-related deep levels in bulk silicon crystal", Journal of Applied Physics **63**, 2304–2306.

[41]J. Davis et al., "Impurities in silicon solar cells", IEEE Transactions on Electron Devices **27**, 677 –687 (1980).

[42]W. Shockley and J. W. T. Read, "Statistics of the recombinations of holes and electrons", Phys. Rev. **87** (1952) 10.1103/PhysRev.87.835.

[43]N. B. A. Portavoce A. De Luca and M. Texier, "Redistribution of metallic impurities in Si during annealing and oxidation: W and Fe", Defect and Diffusion Forum **383**, 17–22 (2018).

[44]G. González-Dìaz et al., "Intermediate band for solar cells. Transition metals supersaturated silicon approach.", Current Developments in Energy and Sustainability, 1–9 (2013).

[45]"Theory and technology", in *Handbook of ferroalloys*, edited by M. Gasik, 1st ed. (Butterworth-Heinemann, 2013) Chap. 11, pp. 377–385.

[46]A. D. Luca et al., "Tungsten diffusion in silicon", Journal of Applied Physics **115**, 013501 (2014).

[47]A. De Luca, A. Portavoce, M. Texier, N. Burle, and B. Pichaud, "Dynamic segregation of metallic impurities at SiO_2/Si interfaces", Journal of physics: conference series **471**, 012029 (2013).

[48]D. Recht, "Energetic beam processing of silicon to engineer optoelectronically active defects", PhD thesis (Harvard University, 2012).

[49]G. Coletti, "Impurities in silicon and their impact on solar cell performance", PhD thesis (Utrecht University Repository, 2011).

[50]S. Lombardoa et al., "Laser annealing in Si and Ge: Anomalous physical aspects and modeling approaches", Materials Science in Semiconductor Processing **62**, 80–91 (2017).

[51]W. A. Tiller, K. Jackson, J. W. Rutter, and B. Chalmers, "The redistribution of solute atoms during the solidification of metals", Acta Metallurgica **1**, 428–437 (1953).

[52]W. W. Mullins and R. F. Sekerka, "Stability of a planar interface during solidification of dilute binary alloy", Journal of Applied Physics **35**, 444–451 (1964).

[53]A. G. Cullis et al., "Growth interface breakdown during laser recrystallization from the melt", Applied Physics Letters **38**, 642–644 (1981).

[54]J. Narayan, "Interface instability and cell formation in ion-implanted and laser-annealed silicon", Journal of Applied Physics **52**, 1289–1293 (1981).

[55]J.Narayan, "Development of morphological instability and formation of cells in silicon alloys during pulsed laser irradiation", Journal of Crystal Growth **59**, 583–598 (1982).

[56]L. K. Aagesen et al., "Pinch-off of rods by bulk diffusion", Acta Materialia **59**, 4922–4932 (2011).

[57]M. Nastasi and J. W. Mayer, *Ion implantation and synthesis of materials* (Springer-Verlag Berlin Heidelberg, 2006), pp. 23–36, 127–142.

[58]M. I. Current, "Ion implantation of advanced silicon devices: Past, present and future", Materials science in semiconductor processing **62**, 13–22 (2016).

[59]J. S. Williams, "Materials modification with ion beams", Reports on progress in physics **49**, 491–588 (1986).

[60]L. Pelaz, L. A. Marqués, M. Aboy, P. López, and I. Santos, "Improved physical models for advanced silicon device processing", Materials science in semiconductor processing **62**, 62–79 (2017).

[61]G. Hobler and G. Otto, "Status and open problems in modeling of as-implanted damage in silicon", Materials science in semiconductor processing **6**, 1–14 (2003).

[62]A. Claverie, L. F. Giles, M. Omri, B. de Mauduit, G. B. Assayag, and D. Mathiot, "Nucleation, growth and dissolution of extended defects in implanted Si: Impact on dopant diffusion", Nuclear Instruments and Methods in Physics Research Section B **147**, 1–12 (1999).

[63]S. Koffel et al., "End of range defects in Ge", JOURNAL OF APPLIED PHYSICS **12**, 126110 –126110–3 (2009).

[64]D. J. Eaglesham, P. A. Stolk, H. J. Gossmann, and J. M. Poole, "Implantation and transient B diffusion in Si: The source of the interstitials", Applied Physics Letters **65**, 2305–2307 (1994).

[65]J. Li and K. S. Jones, "{311} defects in silicon: The source of the loops", applied physics letters **73**, 3748–3750 (1998).

[66]C. Lu et al., "Direct observation of defect range and evolution in ion-irradiated single crystalline Ni and Ni binary alloys", Scientific Reports **6**, 1–10 (2016).

[67]M. J. Aziz and T. Kaplan, "Continuous growth model for interface motion during alloy solidification", Acta Metallurgica **36**, 2335–2347 (1988).

[68]E. García-Hemme et al., "Room-temperature operation of a titanium supersaturated silicon-based infrared photodetector", Applied Physics Letters **104**, 211105 (2014).

[69]F. Liu et al., "On the insulator-to-metal transition in titanium-implanted silicon", Scientific Reports **8**, 1–8 (2018).

[70]J. H. Kim and J. Y. Lee, "High-resolution transmission electron microscopy study of solid phase crystallized silicon thin films on SiO_2: Crystal growth and defects formation", Journal of Applied Physics **77**, 95–102 (1995).

[71]R. Drosd and J. Washburn, "Some observations on the amorphous to crystalline transformation in silicon", Journal of Applied Physics **53**, 397–403 (1982).

[72]D. B. Williams and C. B. Carter, *Transmission electronic microscopy - a textbook for materials science*, 2nd ed. (Springer Science + Business Media, LLC, 2009), pp. 3–71, 115–126, 141–171, 197–208, 581–603, 639–662.

[73]F. C. Voogt, R. Ishihara, and F. D. Tichelaar, "Melting and crystallization behavior of low-pressure chemical vapor-deposition amorphous Si films during excimer-laser annealing", Journal of applied physics **95**, 2873–2879 (2004).

[74]W. C. Sinke, A. Polman, S. Roorda, and P. A. Stolk, "Explosive crystallization of amorphous silicon: Triggering and propagation", Applied surface science **43** (1989) 10.1016/0169-4332(89)90201-8.

[75]J. S. Im and H. J. Kim, "On the super lateral growth phenomenon observed in excimer laser-induced crystallization of thin film silicon", Applied physics letter **64**, 2303–2305 (1994).

[76]M. O. Thompson, G. J. Galvin, and J. W. Mayer, "Melting temperature and explosive crystallization of amorphous silicon during pulsed laser irradiation", Physical review letter **52**, 2360–2363 (1984).

[77]J. Narayan, C. W. White, M. J. Aziz, B. Stritzker, and A. Walthuis, "Pulsed excimer (KrF) laser melting of amorphous and crystalline silicon layers", Journal of applied physics **57**, 564–567 (1985).

[78]J. S. Im, H. J. Kim, and M. O. Thompson, "Phase transformation mechanisms involved in excimer laser crystallization of amorphous silicon films", Applied physics letter **63**, 1969–1971 (1993).

[79]P. Lejcek, *Grain boundary segregation in metals* (Springer, Berlin, Heidelberg, 2006) Chap. 3.

[80]J. Y. Tsao and P. S. Peercy, "Crystallization instability at the amorphous-silicon/liquid-silicon interface", Physical review letter **58**, 2782–2785 (1987).

[81]D. H. Lowndes, J. G. E. Jellison, S. J. Pennycook, S. P. Withrow, and D. N. Mashburn, "Direct measurements of the velocity and thickness of "explosively" propagating buried molten layers in amorphous silicon", Applied physics letter **48**, 1389–1391 (1986).

[82]W. C. Sinke, A. Polman, S. Roorda, and P. A. Stolk, "Explosive crystallization of amorphous silicon: Triggering and propagation", Applied Surface Science **43**, 128–135 (1989).

[83]In, *Focused ion beam systems: Basics and applications*, edited by N. Yao, 1st ed. (Cambridge University Press, 2007) Chap. 1, pp. 1–10.

[84]L. Repetto, G. Firpo, and U. Valbusa, "Applications of focused ion beam in material science", Materials and technology **42**, 143–149 (2008).

[85]T. Ruska, *Curriculum vitae*, http://ernst.ruska.de/daten_e/mainframe_e.html, Accessed: 2018-10-06, 1999.

[86]M. Knoll and E. Ruska, "Das elektronenmikroskop", Zeitschrift für Physik **78**, 318–339 (1932).

[87]C. Kittel, *Introduction to solid state physics*, edited by S. Johnson, 8th ed. (John Wiley & Sons, Inc., 2005), pp. 23–88, 131–220.

[88]W. L. Bragg, "The diffraction of X-rays by crystals", International journal of research in physical chemistry and chemical physics **228**, 957–968 (1913).

[89]S. J. Pennycook and P. D. Nellist, eds., *Scanning transmission electron microscopy: Imaging and analysis* (Springer Science + Business Media, LLC, 2011), pp. 1–116, 247–352, 393–428.

[90]E. Rutherford, "LXXIX. The scattering of α and β particles by matter and the structure of the atom", Philosophical Magazine, 6th ser. **21**, 669 –688 (1911).

[91]C. P. P. H. Goldstein and J. L. Safko, *Classical mechanics*, 3rd ed. (Pearson Education Limited, 2014) Chap. 3.

[92]G. Cliff and G. W. Lorimer, "The quantitative analysis of thin specimens", Journal of microscopy **103**, 203–207 (1975).

[93]*Accuracy, precision and detection limits*, https://myscope.training/legacy/analysis/eds/accuracy/, Accessed: 2019-05-15, 2014.

[94]A. F. Tasch, H. Shin, C. Park, J. Alvis, and S. Novak, "An improved approach to accurately model shallow B and BF_2 implants in silicon", Journal of the electrochemical society **136**, 810–814 (1989).

[95]K. Suzuki, "Analysis of ion implantation profiles for accurate process/device simulation: Ion implantation profile database based on tail function", Fujitsu scientific & technical journal **46**, 307–317 (2010).

[96]*Investigation on ion implantation models impact on I-V curve and thin film solar cell efficiency* (2007).

[97]K. Pearson, "Contributions to the mathematical theory of evolution. II. Skew variation in homogeneous material", Philosophical Transactions of the Royal Society of London. **186**, 343–414 (1895).

[98]H. Ryssel, G. Prinke, K. Haberger, and K. Hoffmann, "Range parameters of boron implanted into silicon", Applied physics **24**, 39–43 (1981).

[99]T. Lindstrøm, *Kalkulus*, 3rd ed. (Universitetsforlaget, AS, 2006) Chap. 8.

[100]D. G. Ashworth, R. Oven, and B. Mundin, "Representation of ion implantation profiles by Pearson frequency distribution curves", Journal of Physics D: Applied Physics **23**, 870–876 (1990).

[101]M. M. Hossain and M. H Chowdhury, "Heat transfer simulations for pulsed laser annealing of silicon thin film", in Ieee 56th international midwest symposium on circuits and systems (2013).

[102]H. Lysne, "Tungsten doped silicon for intermediate band solar cells", Unpublished manuscript.

[103]*JEM-2100F: Field emission electron microscope*, JEOL Ltd. (2003) Chap. 2–4.

[104]*EM-31640 specimen tilting beryllium holder, Instructions*, JEOL Ltd. (2014).

[105]*DigiScan, User's Guide*, Gatan, Inc. (2004).

[106] *DigitalMicrograph software 3*, Gatan, Inc. (2018).

[107] *ImageJ, Image processing and analysis in Java*, National Institutes of Health (2004).

[108] T. Ferreir and W. Rasband, *ImageJ user guide* (2012).

[109] N. Rowlands and S. Burgess, "Energy dispersive analysis in the TEM", materialstoday **12**, 46–48 (2010).

[110] *Photovoltaics report.* Tech. rep. (Oxford instruments analytical Ltd, 2008).

[111] N. A. Berjeza, S. P. Velikevitch, V. I. Mazhukin, I. Smurov, and G. Flamant, "Influence of temperature gradient to solidification velocity ratio on the structure transformation in pulsed- and CW-laser surface treatment", Applied Surface Science **86**, 303–309 (1995).

[112] K. Gao, S. Prucnal, W. Skorupa, M. Helm, and S. Zhou, "Formation and photoluminescence of $GaAs_{1-x}N_x$ dilute nitride achieved by N-implantation and flash lamp annealing", Applied Physics Letters **105**, 012107 (2014).

[113] K. Barmak, J. Liu, L. Harlan, P. Xiao, J. Duncan, and G. Henkelman, "Transformation of topologically close-packed β-W to body-centered cubic α-W: Comparison of experiments and computations", THE JOURNAL OF CHEMICAL PHYSICS **147**, 152709 (2017).

[114] K. L. Chopra, M. R. Randlett, and R. H. Duff, "Face-centered-cubic tungsten films obtained by", THE JOURNAL OF CHEMICAL PHYSICS **9** (1966) 10.1063/1.1754629.

[115] Q. Hao, W. Chen, and G.Xiao, "Beta (β) tungsten thin films: Structure, electron transport, and giant spin Hall effect", Applied Physics Letters **106**, 182403 (2015).

[116] J. Lukovic et al., "Tungsten disilicide (wsi_2): Synthesis, characterization, and prediction of new crystal structures", Journal of inorganic and general chemistry **643**, 2088–2094 (2017).

Jørgen Sørhaug

TEM characterization of tungsten-implanted silicon

NTNU
Norwegian University of
Science and Technology